Aus der Klinik für Gastroenterologie, gastrointestinale Onkologie und Endokrinologie
(Prof. Dr. med. V. Ellenrieder)
der Medizinischen Fakultät der Universität Göttingen

The role of the ROBO3-signaling pathway in pancreatic cancer plasticity

INAUGURAL-DISSERTATION

zur Erlangung des Doktorgrades
der Medizinischen Fakultät der
Georg-August-Universität zu Göttingen

vorgelegt von

Niklas Krebs

Aus

Bielefeld

Göttingen 2022

Dekan:	Prof. Dr. W. Brück

Betreuungsausschuss

Betreuer	Prof. Dr. V. Ellenrieder

Prüfungskommission

Referent/in	Prof. Dr. V. Ellenrieder
Ko-Referent/in:	Prof. Dr. M. Zeisberg
Drittreferent/in:	Prof. Dr. T. Meyer

Datum der mündlichen Prüfung: 08.09.2022

Hiermit erkläre ich, Niklas Krebs, die Dissertation mit dem Titel " The role of the ROBO3-signaling pathway in pancreatic cancer plasticity" eigenständig angefertigt und keine anderen als die von mir angegebenen Quellen und Hilfsmittel verwendet zu haben.

Göttingen, den …… ……

(Unterschrift)

Table of contents

List of figures

List of tables

List of abbreviations

ADEX	Aberrantly differentiated endocrine exocrine
ADM	Acinar-to-ductal metaplasia
AGR2	Anterior Gradient 2, Protein Disulphide Isomerase Family Member
ALDH1B	Alcohol dehydrogenase 1B (Class I), Beta Polypeptide
AXL	AXL receptor tyrosine kinase
BGB324	Bemcentinib
BL	Basal-like
BRCA1	Breast cancer 1
BRCA2	Breast cancer 2
BSA	Bovine serum albumin
CA 19-9	Carbohydrate antigen 19-9
CAF	Cancer associated fibroblast
CAPN8	Calpain 8
Cas9	CRISPR associated protein 9
CDC42	Cell division cycle 42
CDKN2A	Cyclin-dependent kinase Inhibitor 2A
cDNA	Complementary DNA
CLA	Classical
CLAS	Classical
cMET	Tyrosine-Protein Kinase Met
CRISPR	Clustered regularly interspaced short palindromic repeats
crRNA	Crispr RNA
DAPI	4',6-Diamidino-2-phenylindole
dCas9	Cas9 Endonuclease Dead
DMEM	Dulbecco's Modified Eagle Medium
DMSO	Dimethylsulfoxide
DNA	Deoxyribonucleic acid
ECM	Extracellular Matrix
ECOG	Eastern Cooperative Oncology Group
EGFR	Epidermal Growth Factor Receptor
EMT	Epithelial to mesenchymal transition
ERBB2	Erb-B2 Receptor Tyrosine Kinase 2
F.o.V.	Field of view
FAM83A	Family With Sequence Similarity 83 Member A
FCS	Fetal calf serum
FOLFIRINOX	Chemotherapy regimen: folinic acid, fluorouracil, irinotecan, oxaliplatin
$Foxn1^{nu/nu}$	Homozygous nude-mutant forkhead box protein N1
GATA6	GATA Binding Protein 6
GCDX	Cell line derived from PDX established in Göttingen

GEKID	Gesellschaft Der Epidemiologischen Krebsregister In Deutschland E.V.
Gem	Gemcitabine
GEMM	Genetically engineered mouse model
GSEA	Gene set enrichment analysis
HE	Hematoxylin-Eosin
HER2neu	human epidermal growth factor receptor 2
HNF1α	HNF1 Homeobox A
HRP	horseradish peroxidase
i.p.	Intraperitoneal
IC_{50}	Inhibitory concentration 50%
IF	Immunofluorescence
IL-6	Interleukin 6
JAK	Janus kinase
KLF5	Krueppel-like factor 5
KRAS	Kirsten rat sarcoma viral oncogene homolog
KRT5	Keratin 5
KRT81	Keratin 81
KSF	Keratinocyte serum-free
LCM	Laser capture microdissection
LRR	Leucine-rich repeat
MAPK	Mitogen-activated protein kinase
MAPKBP1	Mitogen-Activated Protein Kinase Binding Protein 1
MES	Mesenchymal
mRNA	Messenger RNA
NELL2	Neural Epidermal Growth Factor-Like 2
NGS	Normal goat serum
PALB2	Partner and Localizer of BRCA2
PanIN	Pancreatic intraepithelial neoplasia
PARPi	Poly(ADP-Ribose) Polymerase inhibition
PB	Phosphate buffer
PBS	Phosphate-buffered saline
PBST	Phosphate-buffered saline with Tween 20
PDA	Pancreatic ductal adenocarcinoma
PDX	Patient-derived xenograft
PLEKHG1	Pleckstrin Homology And RhoGEF Domain Containing G1
QM	Quasi-mesenchymal
RNA	Ribonucleic acid
RNA-seq	RNA-sequencing
ROBO	Roundabout receptor
ROBO3	Roundabout receptor 3
RPMI	Roswell Park Memorial Institute

RTK	Receptor tyrosine kinase
RT-qPCR	Real-time quantitative polymerase chain reaction
s.c.	Subcutaneous
SD	Standard deviation
SDS-PAGE	Sodium dodecyl sulfate polyacrylamide gel electrophoresis
sgRNA	Single guide RNA
SLC39A13	Solute Carrier Family 39 Member 13
SLIT	SLIT Guidance Ligand
SMAD4	Small mothers against decapentaplegic homolog 4
SNAIL	Zinc finger protein SNAI1
Sox2	SRY (Sex Determining Region Y)-Box 2
STAT	Signal transducer and activator of transcription
TBS	TRIS-buffered saline
TBST	TRIS-buffered saline with Tween 20
TEMED	Tetramethylethylenediamine
TGF-β	Transforming growth factor β
TME	Tumor mircoenvironment
TNC	Tenascin C
TNFα	Tumor necrosis factor α
TP53	Tumor protein 53
tracerRNA	Trans-activity RNA
Twist	Twist Family BHLH Transcription Factor
VIM	Vimentin
Wnt	Wingless-related integration site
ZEB1	Zinc finger E-box-binding homeobox

1 Introduction

1.1 Pancreatic ductal adenocaricoma

1.1.1 Epidemiology and risk factors

In Germany, about 18.000 people suffer annually from pancreatic cancer, which corresponds to an incidence of ten to fourteen per 100,000 inhabitants (Koch-Institut und GEKID 2019). The median age at diagnosis is 71 years, while it affects men more frequently than women and occurs more often in industrialized countries (Ryan et al. 2014). It is anticipated that pancreatic cancer becomes the second leading cause of cancer-related death by the end of 2030 (Rahib et al. 2014; Siegel et al. 2019). Pancreatic cancer is a highly complex and multifactorial disease caused by certain genetic alterations (e. g., *BRCA-1/2* mutation), epigenetic changes and transcriptional alterations. Besides these essential molecular abnormalities, environmental risk factors such as smoking, obesity, high alcohol consumption or pre-existing conditions such as chronic pancreatitis and diabetes mellitus, play a major role in the development of pancreatic cancer (Becker et al. 2014).

1.1.2 Pancreatic cancer development

The most frequent malignant process in the pancreas is the Pancreatic Ductal Adenocarcinoma (PDA), with more than 95 % of the cases (Koorstra et al. 2008). Nowadays, it is assumed that the development of PDA is based on a gradual multi-stage process and is characterized by the stepwise acquisition of driver mutations in defined precursor lesions (Figure 1). The most frequent precursor lesions of pancreatic carcinoma are Pancreatic Intraepithelial Neoplasia (PanINs), whereas Intraductal Pancreatic Mucinous Neoplasia (IPMNs) occur less prevalent (Koorstra et al. 2008; Hruban et al. 2008). PanINs are divided into three stages depending on the degree of epithelial atypia, ranging from minimal (PanIN-1) to profound atypia (PanIN-3). The PanINs develop from the pancreatic acinar cells via Acinar-to-Ductal Metaplasia (ADM) and subsequently might progress towards an invasively growing cancer via the carcinoma in situ (PanIN-3) stage (Koorstra et al. 2008).

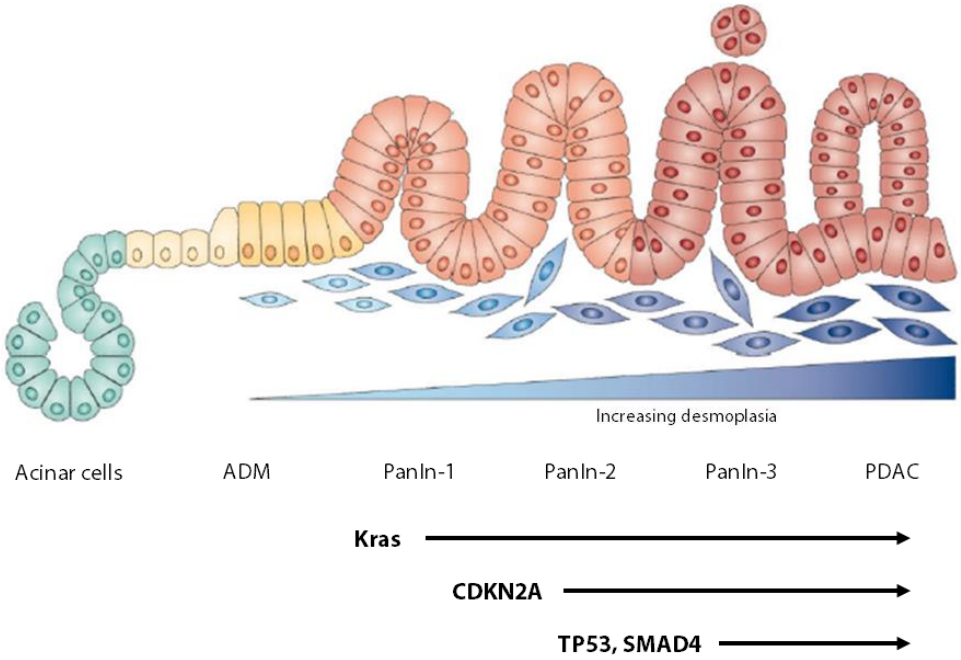

Figure 1. Progression Model of Pancreatic Cancer. Schematic illustration of the development of pancreatic cancer from early precursor lesions. After initial Acinar-to-Ductal Metaplasia (ADM), a sequential accumulation of driver mutations promotes the formation of Pancreatic Ductal Adenocarcinoma (PDA) from early Pancreatic Intraepithelial Neoplasia (PanIN) (Morris et al. 2010). This figure was modified after Morris et al. 2010 with the permission and RightsLink Printable License of Springer Nature.

1.1.3 Genetic alterations in pancreatic cancer

The understanding of the molecular biology of pancreatic carcinoma is currently still a major subject of research. The four most common oncogenic events are mutations of *KRAS (Kirsten rat sarcoma virus), TP53(Tumor protein 53), SMAD4 (Small mothers against decapentaplegic homolog 4)* and *CDKN2A (Cyclin dependent kinase inhibitor 2A)*. *KRAS* mutations, which occur in more than 90 % of pancreatic ductal adenocarcinomas (Hruban et al. 1993; The Cancer Genome Atlas Research Network et al. 2017), result in a constitutive activation of the protein, which in turn leads to an increased proliferation and cell survival. However, *KRAS* mutations are not sufficient for the development of a full-blown invasive carcinoma. Mutations of the tumor suppressor genes *TP53, SMAD4* or *CDKN2A* are leading to their inactivation (Redston et al. 1994; Massagué et al. 2000). The loss of *CDKN2A* leads to an insufficient phosphorylation of Rb-1, which in turn can cause rapid cell cycle transition at G1/S phase (Sellers et al. 1995). The p53 protein is central to modulating cellular responses to cytotoxic stress by promoting both cell cycle arrest and programmed cell death (Gnoni et al. 2013). An inactivation of the *p53* tumor suppressor gene in pancreatic cancer occurs in 50 %-75 % (Redston et al. 1994) and results in inappropriate cell growth, increased cell survival

and genomic instability (Muller and Vousden 2013). Mutations of *SMAD4* are detected in about 55 % of cases (Koorstra et al. 2008). The transcription factor SMAD4 is an important regulator of the transforming growth factor beta (TGF-β) signaling pathway, thus mutations causing a disruption of connected intracellular signaling cascades leading to reduced growth (Massagué et al. 2000). In addition to those major genetic alterations, genome analyses of pancreatic cancer reveal a complex mutation landscape, reflected by a great number of genes mutations that occur with only low prevalence. Despite the remarkable genetic heterogeneity, oncogenic point mutations of individual genes can aggregate to alter molecular core pathways, including those involved in DNA damage repair, cell cycle regulation, TGF-β signaling, chromatin regulation, and axon guidance as indicated in Figure 6 (Bailey et al. 2016).

1.1.4 Current therapy

Currently, surgical resection is the only potential curative treatment for pancreatic cancer, although recurrence rates are high and long-term survival rates are inevitable (Hidalgo et al. 2017). Evidently, 80-85 % of locally advanced tumors are not resectable at the time of the diagnosis (Vincent et al. 2011). If distant metastases are already present, surgery is usually no longer possible and only a palliative approach of chemo- and possibly radiotherapy remains (Neesse et al. 2015). The aim of surgical resection is to attain R0 resection, as it is associated with a significantly increased survival in comparison to R1 resections (Demir et al. 2018). Adjuvant treatment is indicated for patients who are undergoing a R0/R1 resection with a pT1-4/N0-1/M0, ECOG PS (Eastern Cooperative Oncology Group Performance Status) 0-1 and appropriate nutritional status (Oettle et al. 2013). The late diagnosis paired with aggressive tumor biology and early metastatic tendency of pancreatic carcinoma complicate adequate therapy and significantly worsen the prognosis (Ryan et al. 2014). Due to the frequent unresectability of tumors, neoadjuvant and palliative chemotherapeutics is of great importance in current research. Gemcitabine has been approved as a first-line reference drug for patients with good performance status since 1997 (Burris et al. 1997). Gemcitabine's advantage over 5-FU has been demonstrated in several individual studies. A comparative Phase III study (n = 126) with single-agent gemcitabine and 5-FU revealed a benefit response in 23.8% of patients receiving gemcitabine compared to 4.8% of patients treated with 5-FU (Burris et al. 1997). Patients treated with gemcitabine had median survival times of 5.6 and 4.4 months and one-year survival rates were 18% for gemcitabine patients and 2% for 5-FU patients (Burris et al. 1997). Similarly, other Phase II/III clinical trials showed a positive or partially positive response to gemcitabine between 5.4% and 12% (Di Costanzo et al. 2005; Rothenberg et al. 1996). PDA management of patients with locally advanced disease is one

of the most controversial therapeutic domains. A significant life-prolonging effect has been demonstrated in recent years for FOLFIRINOX (oxaliplatin, irinotecan, fluorouracil, leucovorin) and gemcitabine nab-paclitaxel, therefore, the current standard for patients, who are fully eligible for chemotherapy, is either gemcitabine nab-paclitaxel or FOLFIRINOX (Conroy et al. 2011; Hoff et al. 2013). Nevertheless, the prognosis with a mean survival time of 11.1 months with FOLFIRINOX therapy or 8.5 months with Gemcitabine-nab-paclitaxel therapy remains very poor (Conroy et al. 2011; Hoff et al. 2013).

1.1.4.1 Stratification of PDA - Novel therapeutic approaches in PDA treatment

A major clinical challenge in the approach to develop profitable new therapeutic regimes in PDA is the complex intra-and inter-tumor heterogeneity. Within this molecular heterogeneity, however, there are subgroups of PDA patients who harbor key genetic mutations in certain signaling pathways and could therefore potentially benefit from targeted therapy. Recently, it has been shown that a subgroup of PDA patients (12-15 %) with key genetic mutations, particularly in the DNA damage repair pathway (*BRCA1* (*Breast cancer 1), BRCA2 (Breast cancer 2)* and *PALB2 (Partner and Localizer of BRCA2)*), significantly benefit from platinum-based therapy in the first line, and in addition have prolonged survival in maintenance treatment with PARP inhibitors (Waddell et al. 2015; Golan et al. 2019).

However, the heterogeneity of PDA is not exclusively displayed by its different mutation profiles but also due to differences on the transcriptional level. The rise of whole-exome sequencing and transcriptome profiling significantly improved the understanding of molecular subtypes, which can be used as a guideline for preclinical and clinical therapeutic development and treatment in many types of cancer (Collisson et al. 2019). Recently, the first prospective clinical study (COMPASS; NCT02750657) was conducted on the applicability of molecular subtype-based prognosis and treatment approaches for PDA (Aung et al. 2018). At present, pancreatic cancer subtypes are not yet decisive for treatment decisions, but the ability to predict optimal treatment strategies based on subtypes before treatment could improve overall patient outcomes and minimize treatment-related morbidity (Collisson et al. 2019).

This illustrates the potential of molecular stratification in PDA and in addition, suggests that stratification-based therapeutic decisions might be a promising strategic approach in near future.

1.2 Molecular subtyping of pancreatic cancer

Despite significant therapeutic efforts in the last 10-15 years, the prognosis has not changed significantly. Nevertheless, there is growing evidence suggesting that therapeutic efficacy correlates with the underlying molecular fingerprint of the tumor (Bailey et al. 2016).

Notably, the first powerful PDA study on molecular subtyping was published by Collisson in 2011 (Collisson et al. 2011). Based on mRNA (Messenger RNA) transcriptional profiling analysis of untreated, primarily resected PDA, they identified three subtypes that were defined as classical, quasi-mesenchymal (QM-PDA) and exocrine. Key features of the classical subtype included high expression levels of adhesion-associated genes and markers of epithelial differentiation. The QM-PDA subtype showed a high expression of mesenchymal associated genes, whereas the exocrine subtype presented a relatively high expression of digestive enzymes from tumor cells. Furthermore, they reported the potential of subtype stratification for prognoses and treatment responsiveness. In particular, individuals with classical subtype tumors performed better than individuals with QM-PDA subtype tumors after resection (Figure 2; Collisson et al. 2011).

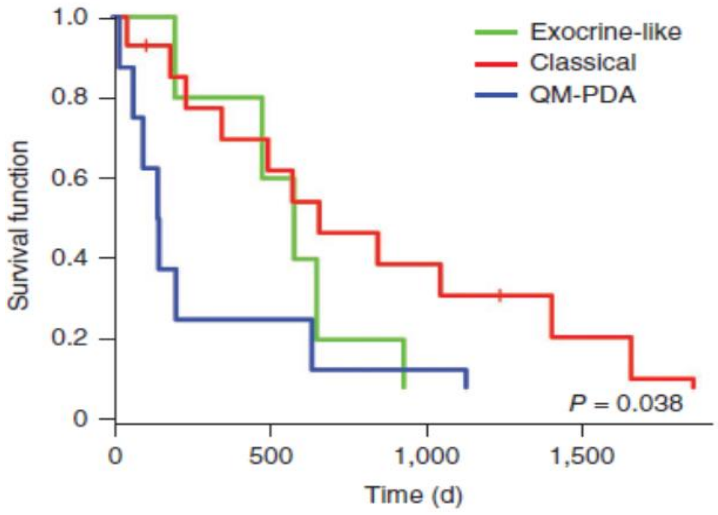

Figure 2. PDA-Subtypes show different prognostic outcome. Kaplan-Meier survival curve, of the 3 classified subtypes of Collisson et al., show different survival rates. Subtypes were defined by transcriptional profiles. Adopted from Collisson et al. 2011 with the permission and RightsLink Printable License of Springer Nature.

PDA is often characterized by extensive accumulation of stromal components, which makes it difficult to capture precise tumor-specific molecular stratification. In 2015, Moffitt et al. have overcome this barrier and provided new insights into the molecular composition of PDA by excluding transcripts that may originate from normal pancreas and distinguishing

between the epithelial-tumor compartment and the stromal compartment. By applying blind source separation to a diverse collection of PDA gene expression microarray data they identified a classical and basal-like subtype from epithelial compartment. In addition, they defined "normal" and "activated" stroma subtypes based on the separate clustering of tumor stroma and normal gene expression, which are autonomously prognostic (Moffitt et al. 2015).

In 2016, Bailey et al. have established a form of molecular subtyping based on an integrated genomic analysis of 456 PDA tumors and classified four molecular subtypes according to differences in the expression of transcription factors and their downstream targets: squamous, pancreatic progenitor, immunogenic and Aberrant Differentiated Endocrine eXocrine (ADEX) (Bailey et al. 2016). All subtypes show different gene expression profiles, but only the squamous subtype is a self-contained predictor for an overall reduced survival. Importantly, the defined subtypes significantly overlap with the subtypes from Collisson et al. In detail, the squamous subtype corresponds well to the QM and basal-like subtype and the pancreatic precursor subtype mirrors expression of gene signatures that have been described for the classical (or ADEX) phenotype (Figure 3). Notably, squamous, QM and basal-like subtypes significantly overlap among these large collaborative molecular classifications of PDA and are associated with a poor prognosis and resistance to conventional chemotherapy. A re-analysis of the original data from Collisson, Moffitt and Bailey for tumor purity from the Cancer Genome Atlas Research Network (TCGA) showed that Collisson's exocrine-like and QM subtypes and Bailey's ADEX and immunogenic subtypes had low purity (The Cancer Genome Atlas Research Network et al. 2017). Nevertheless, a consistent classification of patients into basal-like/squamous and classic/precursor group was possible when applying these classifications to their own data set of high-purity tumors, and thus these data suggest a distinction of the clinically most relevant subtypes among only two tumor-specific subtypes (The Cancer Genome Atlas Research Network et al. 2017). Recently, this classification was confirmed by the application of a machine learning approach using Laser Capture Microdissection (LCM) and subsequent RNA-sequencing, which allows a consistent separation of specific tumor compartments (Maurer et al. 2019). Their findings also validate the previous tumor classification in the aforementioned groups (Maurer et al. 2019).

The new perspective of molecular classification could potentially have major implications for a better understanding of tumor biology and the development of therapeutic strategies. The latter is particularly relevant as recent studies suggest that the molecular signature of a tumor is defined in an extreme way not only by genetic alterations but also by epigenetic alterations and by extra- and intracellular signaling pathways. Importantly, these dynamic processes are

not only caused by tumor-tumor cell interaction but also through the impact of the tumor environment. Correspondingly, this requires a precise understanding of the interaction between the tumor and its environment.

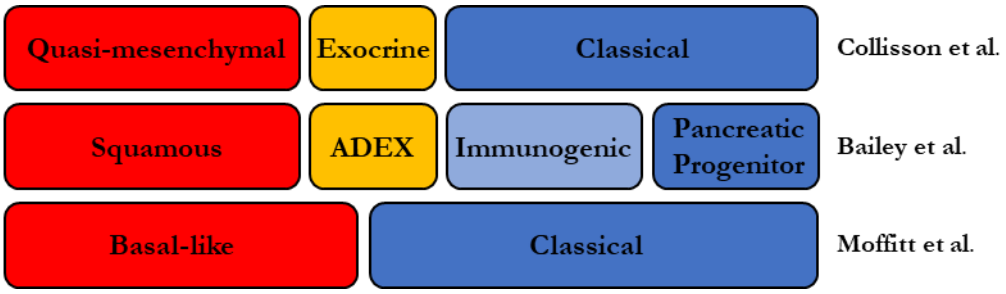

Figure 3. Subtyping in PDA. To define subtypes in PDA, a number of genomic and transcriptomic analyses were performed. Summary of the overlap among the three major transcriptomic studies by Collisson, Moffitt, and Bailey (Le Large et al. 2017). Modified after Le Large et al. 2017.

1.3 Cellular plasticity and epithelial to mesenchymal transition in PDA progression

Cellular plasticity describes the ability of cells to adopt different identities along a phenotypic spectrum, a process that also occurs during cancer progression, leading to molecular and phenotypic changes of tumor cells (Yuan et al. 2019). The development of cancer is based on the loss of normal cell identity and function. During cancer progression and treatment, cancer cells undergo further phenotypic changes as they are exposed to various metabolic conditions, signaling molecules, stromal elements and therapeutics (Yuan et al. 2019). These altered cellular properties include, among others, transcriptional fluctuations that facilitate metastasis, immune defense or chemoresistance (da Silva-Diz et al. 2018). The best-known example of such changes is the Epithelial-Mesenchymal Transition (EMT), first described by Elizabeth Hay as essential for the development of many tissues and organs in embryos (Hay 1995). The reactivation of EMT is driven by EMT-activating transcription factors (EMT-TFs), mainly from the families SNAIL (snail family zinc finger) , TWIST (Twist related protein) and ZEB (Zinc finger E-Box binding homeobox), causing an increased mobility of cancer cells and thereby favoring the invasion and dissemination of cancer (Nieto et al. 2016). A hallmark of EMT is the loss of epithelial genes (e.g. *E-Cadherin (ECAD)*) and the simultaneous induction of mesenchymal genes such as the intermediate-filament protein *vimentin* (Lamouille et al. 2014). Clinically, the tumor grade reflects the manifestation of an EMT phenotype, as poorly differentiated high-grade tumors are characterized by obliteration of normal tissue structure and architecture with histopathological and molecular hallmarks of

EMT (Yuan et al. 2019). While moderately to well differentiated low-grade tumors reflect the maintenance of an epithelial phenotype by cancer cells (Yuan et al. 2019). Numerous studies in PDA have shown that the invasiveness of pancreatic cancer correlates with EMT and is associated with a basal-like subtype (Rhim et al. 2012; Aiello et al. 2018; Zheng et al. 2015). Recent studies show that this process can also be initiated by the interaction of epithelial tumor cells with inflammatory stroma and revealed that basal classified tumors are highly inflamed (Puleo et al. 2018).

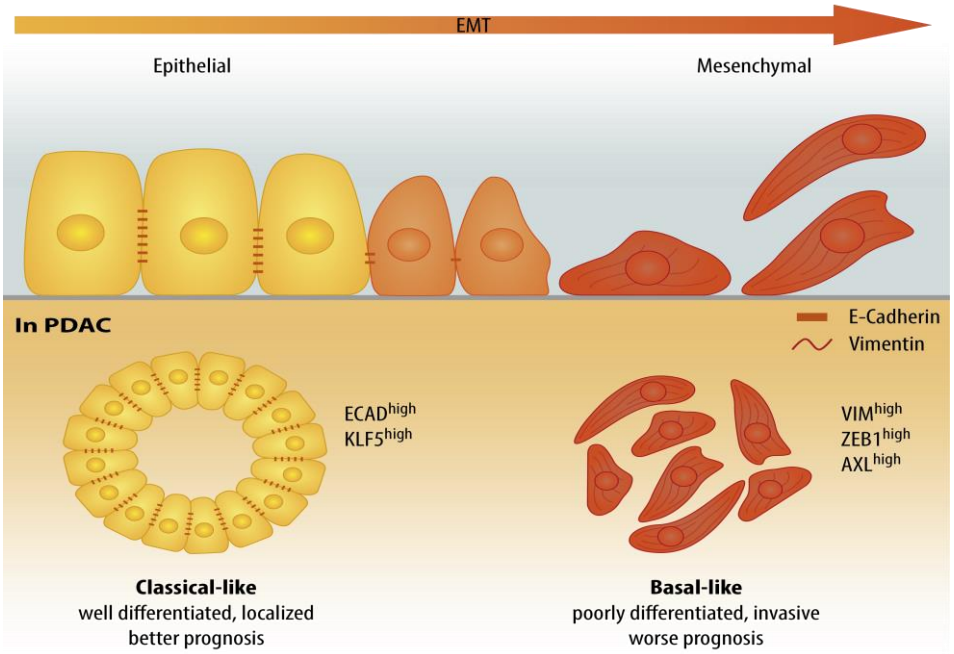

Figure 4. Epithelial to mesenchymal transition and correlation to subtypes in PDA. Schematic illustration from EMT process with the transformation from an epithelial phenotype manifested by the expression of epithelial markers such as KLF5 (Kruppel like factor 5) or ECAD (E-Cadherin) to a mesenchymal phenotype characterized by the expression of ZEB1 or AXL and the loss of epithelial gene signatures.

1.4 Inflammatory tumor microenvironment

An important factor in the carcinogenesis of PDA is the inflammatory tumor microenvironment, as the bulk tumor contains many different components such as blood vesicles, immune cells, fibroblasts, signal molecules and the ExtraCellular Matrix (ECM). In PDA, the stromal fraction can range from 70 to 80 % of the total tumor (Procacci et al. 2018). In general, pancreatic tumors often display increased secretion of pro-inflammatory cytokines and recruitment of tumor associated macrophages (Puleo et al. 2018). A recent study in 308 PDA patient tumors shows a strong correlation between abundance of an inflammatory environment and formation of basal-like tumors, whereas classical tumors are often characterized

by infiltration CD4/8 T-cells (Puleo et al. 2018). Therefore, targeting the crosstalks between epithelial tumor cells and the inflammatory stroma is becoming more important for novel therapeutic approaches. In particular, the inflammatory cytokine InterLeukin-6 (IL-6) plays a role in this context, which is secreted by monocytes and cancer-associated fibroblasts in PDA. Recently, it has been shown that a high expression of IL-6 in the inflammatory stroma is directly associated with a basal-like phenotype (Puleo et al. 2018). In general, IL-6 is associated with tumor progression in several tumor models (Öhlund et al. 2017; Nagathihalli et al. 2016), by enhancing the ability of tumor cells to metastasize through increased angiogenesis and vascular permeability as well as the modulation of the immune environment in tumors (Grivennikov et al. 2010). IL-6 dependent effects are predominantly due to changes in gene expression regulated by the transcriptional regulatory activity of Signal Transducer and Activator of Transcription 3 (STAT3).

1.5 The role of axon guidance receptor family and its role in pancreatic cancer

Axon guidance molecules, SLIT glycoproteins (SLIT) and ROundaBOut Receptors (ROBO), influence the regulation of several physiological processes, such as cell proliferation and cell motility in a variety of cell and tissue types, and were originally introduced as extracellular signatures in the nervous system that act as axon guidance signals, promote axon branching and control neuronal migration during development (Ballard and Hinck 2012). The interaction of SLIT and ROBO is highly involved in the developmental processes of various organs as breast, lung, liver, kidney, eye and reproductive system (Hinck 2004; Greenberg et al. 2004).

1.5.1 The Axon guidance receptor family

The SLIT family consists of the glycoproteins SLIT1, SLIT2 and SLIT3, originally detected in *Drosophila* (Jürgens et al. 1984). The structure is highly conserved among vertebrates. Important for their interaction with ROBO proteins is one of the four leucine-rich repeat (LRR) domains (D1-D4) at the N-terminal end, the D2 region (Morlot et al. 2007). SLIT binds to ROBO receptors and induce signaling pathways that are still poorly understood.

ROBO proteins form a transmembrane receptor and belong to the IgCAM superfamily with a conserved cytoplasmic domain (Fujiwara et al. 2006; Domyan et al. 2013). The number of *ROBO* genes varies between invertebrates and vertebrates, with four *ROBOs (ROBO1, ROBO2, ROBO3* and *ROBO4*) identified in humans (Ballard and Hinck 2012). The different

ROBO receptors differ in their amount of Ig domains fibronectin type 3 (FN3) repeats. Thereby, the Ig1 and Ig2 of their ectodomain is important for the interaction with the D2 domain of SLIT proteins (Morlot et al. 2007). The intracellular domain comprises several 'cytoplasmic conserved' motifs (CC0-CC3) that are variably expressed in different ROBO receptors (Blockus and Chédotal 2016). This different expression of the conserved cytoplasmic domains modulate the interaction of SLIT protein with downstream signaling pathways (Ballard and Hinck 2012; Blockus and Chédotal 2016). The signal transduction of the ROBO receptor family is mediated by the scaffolding and downstream molecules (Blockus and Chédotal 2016). The expression of the different ROBO isoforms differs between tissue types, as ROBO2 and ROBO3 are highly expressed in the nervous system but not in the vascular system (Yadav and Narayan 2014). Meanwhile ROBO1 expression has been shown in both systems and ROBO4 is a specific receptor in endothelial cells (Koohini et al. 2019). Due to a few amino acid changes in its Ig1 domain of the ectodomain, ROBO3 lost the ability to bind SLITs (Zelina et al. 2014). However, ROBO3 primarily interact with the chemoattractant signaling pathway Netrin 1/DCC (Zelina et al. 2014), as well as with the Neural EpidermaL growth factor-Like 2 (NELL2) (Jaworski et al. 2015).

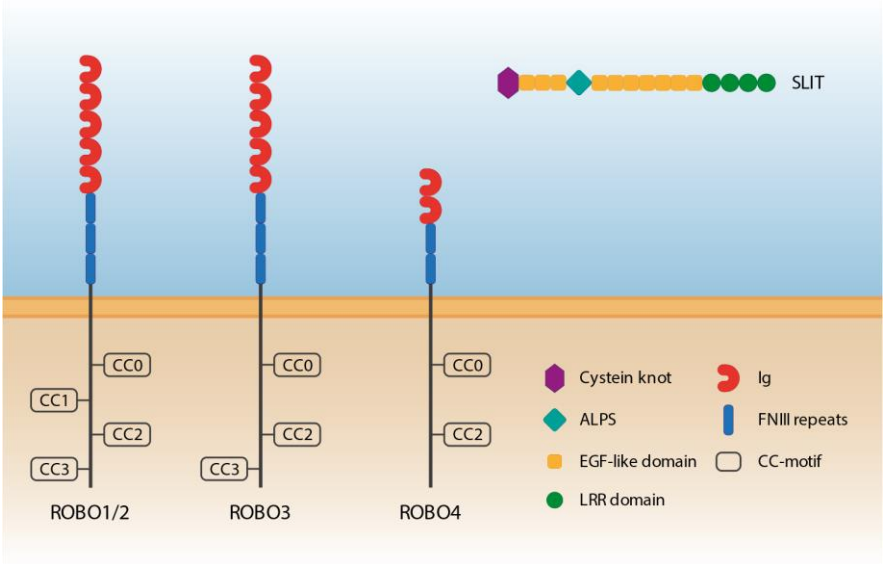

Figure 5. Structure of the different ROBO receptors and the ligand SLIT. Schematic illustration of the structural properties of the different ROBO and SLIT proteins. The legend is indicated in the figure. SLITs are the main ligands of ROBO receptors, composed of four leucine-rich repeat (LRR) domains, seven to nine epidermal growth factor (EGF) like repeats, an Agrin-Perlecan-Laminin-SLIT (ALPS) and a C-terminal cysteine knot (Blockus and Chédotal 2016). ROBO receptors are single-pass transmembrane proteins containing five immunoglobulin-like domains (Ig1-5) and three fibronectin repeats (FNIII 1-3) as an ectodomain. The intracellular domain comprises several conserved regions termed CC ('cytoplasmic conserved') motifs (Blockus and Chédotal 2016).

1.5.2 The Axon guidance receptor family in pancreatic cancer

Recent studies have shown that SLIT and ROBO also play an important role in tumorigenesis, tumor growth, angiogenesis and metastasis in different tumor entities (Mehlen et al. 2011). The role of axon guidance molecules in cancer progression has been explored for more than a decade, but their precise function remains elusive. By their nature, axon guidance molecules are bifunctional and act both as attractants and as inhibitors of migratory axons and cells. Depending on the cellular context, they can act as tumor cell promoting and suppressing, by enhancing or inhibiting tumor cell invasion (Ballard and Hinck 2012). In PDA about 20 % of the PDA cases show a mutation of the axon guidance pathways (Figure 5). Thereby, it is one of the most frequently frequented mutant signaling pathways in PDA, which confirms that mutations of the axon guidance are an important genomic event for pancreatic carcinogenesis (Bailey et al. 2016).

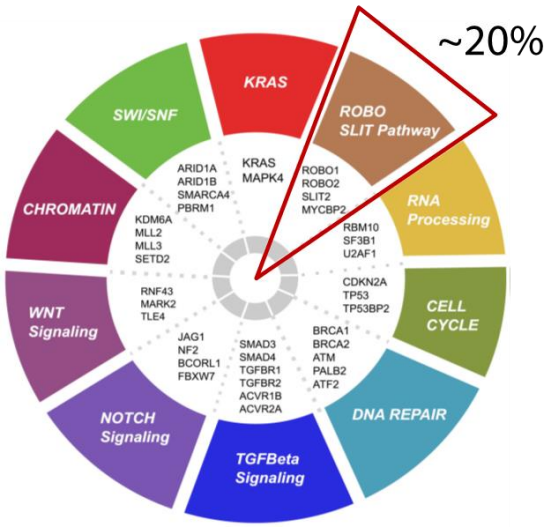

Figure 6. Core signaling pathways in PDA. Schematic illustration of the most frequently mutated signaling pathways in ductal pancreatic adenocarcinoma (Bailey et al. 2016). As indicated in the figure, alterations in axon guidance pathways potentially affect 20% of PDA cases. Adopted and modified after Bailey et al. 2016 with the permission and RightsLink Printable License of Springer Nature.

In PDA, ROBO1 and ROBO2 act as tumor suppressors and are mainly lost through copy number variations. Thus, low expression levels are associated with a poor survival (Biankin et al. 2012). Mechanistically, SLIT/ROBO signaling enhances the formation of β-catenin complexes with E-cadherin and inhibits Wingless-related integration site (WNT) signaling activity (Biankin et al. 2012). Accordingly, the loss of ROBO1/2 signaling facilitates the stabilization of β-catenin, leading to decreased formation of E-cadherin complexes and cell adhesion along with increased WNT signaling activity due to increased nuclear translocation of β-catenin (Biankin et al. 2012; Macias et al. 2011). Furthermore, ROBO/SLIT signaling can down-regulate Tyrosine-Protein Kinase MET (MET) signaling activity via the rho-GTPase

CDC42 (Cell division control protein 42 homolog), suggesting that the loss of ROBO1/2 signaling activity promotes MET signaling downstream, which may influence therapeutic strategies (Stella et al. 2009; Huang et al. 2015). Recently it was demonstrated that the ROBO1/2 pathway is relevant for the establishment of cell identity in the initial phases of pancreatic cancer development (Escot et al. 2018) and stroma activity modulation in pancreatitis and PDA (Pinho et al. 2018).

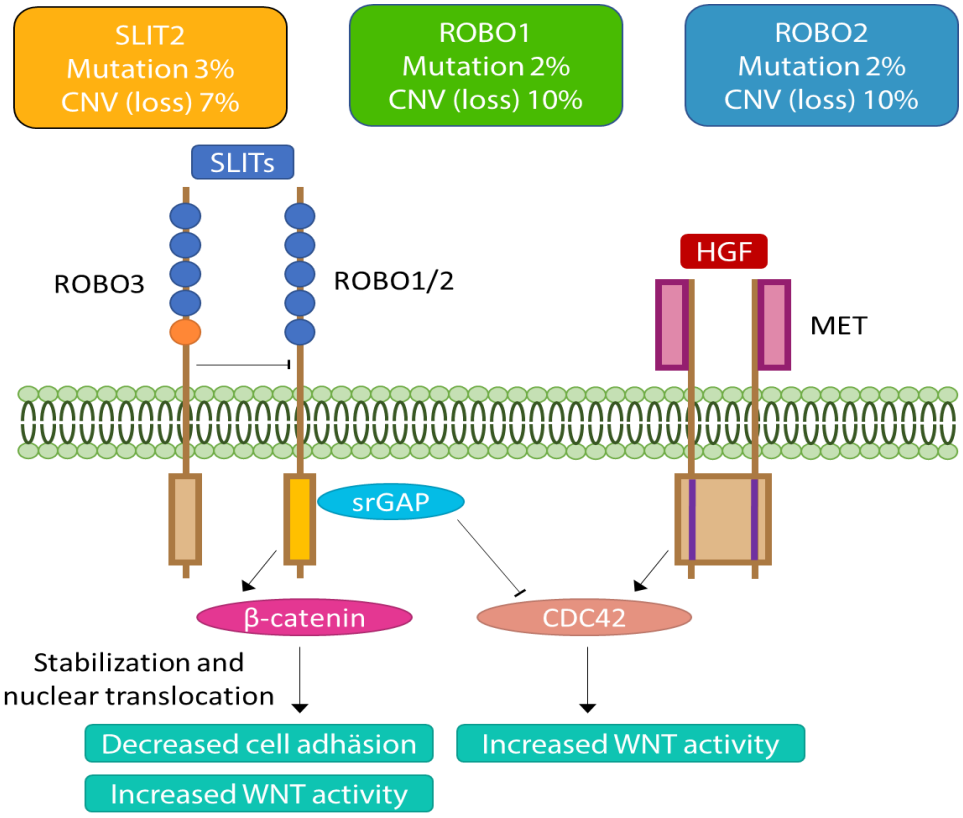

Figure 7. Axon guidance in PDA. Assumed model adopted from Biankin et al. 2012, about the functionality of the Axon guidance pathway in PDA. Loss of ROBO1/2 signaling stimulates b-catenin stabilization, which decreases E-cadherin complex formation and cell adhesion, and augments WNT signaling activity by increasing nuclear translocation of b-catenin (Biankin et al. 2012). Moreover, SLIT/ROBO signaling may downregulate MET signaling activity. It is assumed that ROBO3 also inhibits the function of ROBO1 and ROBO2 in PDA (Sabatier et al. 2004; Biankin et al. 2012). Adopted and modified after Biankin et al. 2012 with the permission and RightsLink Printable License of Springer Nature.

1.5.3 The role of ROBO3 in pancreatic cancer development

In contrast to ROBO1/2, high ROBO3 expression levels are associated with poor prognosis in PDA patients (Biankin et al. 2012). Moreover, other groups reported that overexpression of ROBO3 is associated with growth and invasion in *in vitro* PDA models (Han et al. 2015). Interestingly, a study by Sabatier et al. showed that the expression of ROBO3 is inversely correlated with SLIT sensitivity in mammals. Furthermore, it was assumed that ROBO3 also

inhibits the function of ROBO1 and ROBO2 in PDA (Sabatier et al. 2004; Biankin et al. 2012). However, in PDA it remains unclear how ROBO3 is activated, by which pathways it transduces its signals and how its oncogenic properties are regulated.

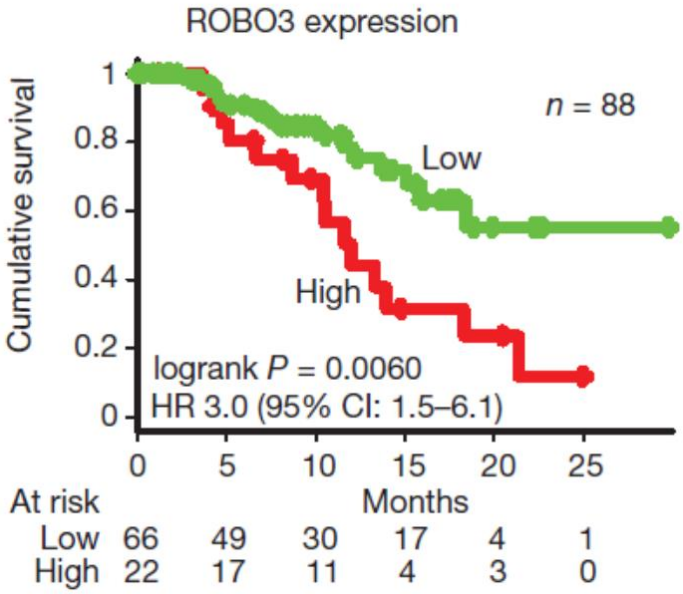

Figure 8. High ROBO3 expression is associated with poor survival of PDA patients. Kaplan–Meier survival curves showing that high levels of ROBO3 are significantly associated with a worse survival of primary operable, untreated PDA patients. N=88. Adopted from Biankin et al. 2012 with the permission and RightsLink Printable License of Springer Nature.

1.6 Aims

Pancreatic cancer remains one of the most lethal cancer entities, with limited therapeutic options and a still basic understanding of the molecular mechanisms of its therapy resistance. Interestingly, the ROBO/SLIT pathway is affected by mutations in about 20 % of all PDA cases. However, the influence of its deregulation remains largely unknown. Especially, regulation of the oncogenic isoform ROBO3-mediated signaling pathways remain greatly unknown and offer and interesting potential in targeting oncogenic features like invasions. Therefore, the aim of this study was to elucidate the role of the ROBO3 signaling pathway in tumor aggressiveness and therapy resistance of the PDA and gain new insights for a possible targeted therapy strategy. Thereby, the major questions we addressed were once to characterize the ROBO3 signaling pathway in the highly invasive basal-like phenotype. Furthermore, we examined the role of ROBO3 regulating cellular plasticity and invasiveness of pancreatic cancer and the mediation of drug resistance.

2 Material and Methods

2.1 Material

Equipment, consumables, and chemicals used for this study are listed below.

Table 1. Equipment

Equipment designation	Company and head office
Aspirator with trap flask FTA-1	Grant Instruments, Cambridge, UK
Autoclave Laboclav LGAK0061	SHP Steriltechnik AG, Detzel Schloss, Germany
Camera E-PL8	Olympus, Shinjuku, Japan
Centrifuge Heraeus Multifuge X1R	Thermo Fischer Scientific, Waltham, MA, USA
Cryo Cooler "Mr Frosty"	Nalgene, Rochester, New York, USA
Detection device ECL ChemoCam Imager	Intas Science Imaging, Göttingen, Germany
ErgoOne Single-Channel Pipette (0,1-2,5µL)	StarLab, Hamburg, Germany
Fluoview F1000 Confocal Microscope	Olympus, Shinjuku, Japan
Freezer -20°C	Liebherr, Bulle, Switzerland
Freezer -80°C	Arctiko, Esbjerg, Denmark
Fume hood Airflow Control EN 14175	Weidner Laboreinrichtungs GmbH, Hardegsen
Heat block "Dry bath incubator"	Benchmark Scientific, Edison, NJ, USA
Heat block "Dry Block, DB 2A"	Techne, Staffordshire, UK
Heat plate "OTS 40"	Medite, Burgdorf, Germany
HERAcell 240i CO2 Incubator	Thermo Fischer Scientific, Waltham, MA, USA
Ice machine AF 80	Scotsman, Vernon Hills, IL, USA
Light microscope BX43	Olympus, Shinjuku, Japan
Light microscope CKX53	Olympus, Shinjuku, Japan
Light microscope ID03	Carl Zeiss, Oberkochen, Germany
Magnetic stirrer RH basic	Ika-Werke, Staufen, Germany
Microplate reader PHOmo	Anthos Mikrosysteme, Krefeld, Germany
Microtome RM2265	Leica Biosystems, Nußloch, Germany
Microwave NN-E209W	Panasonic, Kadoma, Japan
Mini centrifuge Sprout	Heathrow Scientific, Vernon Hills, IL, USA

Mini-PROTEAN Tetra Cell	Bio-Rad, Hercules, CA, USA
Multi-functional Orbital Shaker PSU-20i	Grant-bio, Fisher Science, Schwerte, Germany
Multi-functional orbital shaker PSU-20i	Grant Instruments, Cambridge, UK
Multipette plus	Eppendorf, Hamburg, Germany
Nalgene Mr. Frosty freezing container	Thermo Fischer Scientific, Waltham, MA, USA
Nano-Photometer P330	Intas Science Imaging, Göttingen, Germany
Neubauer counting chamber	Brand, Wertheim, Germany
Paraffin embedding station EG 1150H	Leica Biosystems, Nußloch, Germany
Perfect Spin 24Plus Microcentrifuge	VWR/Peqlab, Erlangen, Germany
Perfect Spin 24R Refrigerated Microcentrifuge	VWR/Peqlab, Erlangen, Germany
pH-Meter Five Easy-Plus	Mettler-Toledo, Columbus, OH, USA
PIPETBOY acu	Integra Biosciences, Biebertal, Germany
PowerPac Basic power supply	Bio-Rad, Hercules, CA, USA
Precision scale MC1 Analytic AC 210 P	Sartorius, Göttingen, Germany
Precision scale PCB M Memory	Kern & Sohn, Bahlingen, Germany
Printer Aficio SG 3110 SFNW	Ricoh, Ota, Japan
Printer Ecosys P3125dn	Kyocera, Kyoto, Japan
Refrigerator 4°C	Liebherr, Bulle, Switzerland
Research Plus Single-Channel Pipettes	Eppendorf, Hamburg, Germany
Step One Plus Real-Time PCR System	Applied Biosystems, Foster City, CA, USA
Tissue float bath GFL 1052	Gesellschaft für Labortechnik, Burgwedel, Germany
Tissue processor TP1020	Leica Biosystems, Nußloch, Germany
Trans-Blot Turbo Transfer System	Bio-Rad, Hercules, CA, USA
Ultrasound scanner Vevo 2100	Fujifilm VisualSonics, Toronto, Canada
Universal oven UN55pa	Memmert, Schwabach, Germany
Vortexer Lab Dancer	Ika-Werke, Staufen, Germany
Vortexer Vornado	Benchmark Scientific, Edison, NJ, USA
Water bath WB14	Memmert, Schwabach, Germany

Table 2. Consumables

Consumables	**Company**
Adhesive foil seal for 96-well plate	Applied Biosystems, Foster City, CA, USA

Cadenza-System	Ted Pella Inc., Redding, CA, USA
Cannula (0.45x25 mm, 26G)	Braun, Melsungen, Germany
Casting Frame	Bio-Rad, Hercules, CA, USA
Cell culture flask (T25, T75 and T175)	Sarstedt, Nümbrecht, Germany
Cell culture multi-well plate (6-, 24- and 96-well	Sarstedt, Nümbrecht, Germany
Comb (western blot)	Bio-Rad, Hercules, CA, USA
Combitips advanced (2.5 and 5 mL)	Eppendorf, Hamburg, Germany
Cover glasses 32x24mm	Thermo Fisher Scientific, Waltham, MA, USA
Coverslips (32x24 mm)	Thermo Fisher Scientific, Waltham, MA, USA
Cryotubes 5ml	Corning, NY, USA
Desco Wipes	Desomed, Freiburg, Germany
Disposable gloves, Latex	Semperguard, Northamptonshire, UK
Disposable gloves, Nitril	LLG Labware, Meckenheim, Germany
Dry ice	Linde Gas, Munich, Germany
Embedding cassettes	Roth, Karlruhe, Germany
Falcon cell culture inserts, 8 µm pores	Corning, Corning, NY, USA
Falcon tubes (15 and 50 mL)	Sarstedt, Nümbrecht, Germany
Kimtech Science Wipes	Kimberly-Clark, Irving, TX, USA
Laboratory tissues	Kimberly-Clark, Surrey, UK
Leukosilk	Braun, Melsungen, Germany
Liquid blocker Super PAP-Pen	Dako, Jena, Germany
Micro tube (1,5 and 2 mL)	Sarstedt, Nümbrecht, Germany
MicroAmp optical 96-well reaction plate	Applied Biosystems, Foster City, CA, USA
Microscope slide box	Ted Pella, Redding, CA, USA
Microtome blade S35	Feather, Osaka, Japan
Microvette 500 LH	Sarstedt, Nümbrecht, Germany
Microvetten, Li-Heparin	Sarstedt, Nümbrecht, Germany
Nitrocellulose membrane	Bio-Rad, Hercules (Kalifornien, USA)
Paraffin wax	Sasol Wax, Hamburg, Germany
Petri dishes 6 and 10cm	Sarstedt, Nümbrecht, Germany
Pipette filter tips (10, 200 and 1000 µL)	StarLab, Hamburg, Germany
Pipette tips (10, 200 and 1000 µL)	StarLab, Hamburg, Germany
Plastipak Syringes (1, 5 and 10 mL)	Becton Dickinson, Franklin Lakes, NJ, USA

Polystyrene tube, 12 mL	Greiner Bio-One, Kremsmünster, Austria
Rapid AF alcoholic disinfectant	Desomed, Freiburg, Germany
Rotilabo snap-cap vial with snap-on lid (20 mL)	Roth, Karlruhe, Germany
Roti-Mount	Roth, Karlruhe, Germany
Scalpel	Dahlhausen, Cologne, Germany
Serologic pipette (2 mL)	Sarstedt, Nümbrecht, Germany
Serologic pipette (5, 10, 25 and 50 mL)	Greiner Bio-One, Kremsmünster, Austria
Shandon Immu-Mount	Thermo Fisher Scientific, Waltham, MA, USA
Superfrost Plus slides	Thermo Fisher Scientific, Waltham, MA, USA
Thick blot filter paper	Bio-Rad, Hercules, CA, USA
Ultrasound gel	Dahlhausen, Cologne, Germany
Western roll	Bio-Rad, Hercules, CA, USA

Table 3. Chemicals and reagents

Chemicals and Reagents	**Company**
Acrylamide solution (30%/0.8%)	AppliChem, Darmstadt, Germany
BGB324 (Bemcentinib)	Selleck Chemicals Llc, Houston, Texas, USA
Bromophenol blue	Sigma-Aldrich, St. Louis, MO, USA,
Calcium chloride (CaCl)	Merck, Darmstadt, Germany
Chloroform	Sigma-Aldrich, St. Louis, MO, USA,
Citric acid monohydrate	Carl Roth, Karlsruhe, Germany
Collagen I, rat tail	Enzo Life Sciences, Farmingdale, NY, USA
cOmplete Protease Inhibitor Cocktail Tablets (25x)	Roche, Basel, Switzerland
DAPI	Sigma-Aldrich, St. Louis, MO, USA
Disodium phosphate (Na_2HPO_4)	Carl Roth, Karlsruhe, Germany
Dithiothreitol (DTT)	Sigma-Aldrich, St. Louis, MO, USA
DMEM medium	Life technologies, Carlsbad, California, USA
DMSO	Sigma-Aldrich, St. Louis, MO, USA
EDTA	Thermo Fisher Scientific, Waltham, MA, USA
EGTA	Sigma-Aldrich, St. Louis, MO, USA

Eosin	Sigma-Aldrich, St. Louis, MO, USA
Ethanol, 99%, denatured	Otto Fischar GmbH & Co.KG
Ethanol, 99%, pure	Th. Geyer, Renningen, Germany
FCS	BioWest, Nuaillé, France
Formalin, 10 %	Sigma-Aldrich, St. Louis, MO, USA
Glycerol	Sigma-Aldrich, St. Louis, MO, USA
Glycine	Carl Roth, Karlsruhe, Germany
Hematoxylin	Sigma-Aldrich, St. Louis, MO, USA
HEPES	Life Technologies, Carlsbad, CA, USA
Hydrochloric acid (HCl)	AppliChem, Darmstadt, Germany
Hydrogen peroxide, 30% (H_2O_2)	Carl Roth, Karlsruhe, Germany
Impact DAB	Vector, Burlingame, California, USA
Interleukin 6	PeproTech, Rocky Hill, NJ, USA
Isopropanol	Carl Roth, Karlsruhe, Germany
KSF medium	Thermo Fisher Scientific, Waltham, MA, USA
Lipofectamine™ 2000	Invitrogen, Waltham, MA, USA
Liquid nitrogen	Linde Gas, Munich, Germany
Magnesium chloride ($MgCl_2$)	Merck, Darmstadt, Germany
Matrigel	Abcam, Cambridge, UK
MEM medium	Life technologies, Carlsbad, California, USA
Monopotassium phosphate (KH_2PO_4)	AppliChem, Darmstadt, Germany
Monosodium phosphate (NaH_2PO_4)	Merck, Darmstadt, Germany
Napabucasin	Tocris Bioscience, Bristol, United Kingdom
Paraformaldehyde (PFA)	Merck, Darmstadt, Germany
Penicillin-Streptomycin	Sigma life Science, St. Louis, Missouri, USA
Penicillin-Streptomycin (10000 U/mL)	Thermo Fisher Scientific, Waltham, MA, USA
PMSF	Sigma-Aldrich, St. Louis, MO, USA
Polyethylene glycol 200	Sigma-Aldrich, St. Louis, MO, USA
Ponceau S	Sigma-Aldrich, St. Louis, MO, USA
Potassium bicarbonate ($KHCO_3$)	AppliChem, Darmstadt, Germany
Potassium chlorid (KCl)	Merck, Darmstadt, Germany
Powdered milk, blotting grade	Carl Roth, Karlsruhe, Germany
Protein Assay Dye Reagent	Bio-Rad, Hercules, CA, USA

Concentrate (Bradford reagent)	
Puromycin	Thermo Fisher Scientific, Waltham, MA, USA
RNAse-free water	B. Braun Melsungen, Germany
Roticlear	Carl Roth, Karlsruhe, Germany
RPMI medium	Life technologies, Carlsbad, California, USA
SilentFect™ Lipid Reagent	Bio-Rad, Hercules, CA, USA
Sodium chlorid (NaCl)	Sigma-Aldrich, St. Louis, MO, USA
Sodium dodecyl sulfate (SDS)	Carl Roth, Karlsruhe, Germany
Sodium fluoride (NaF)	Sigma-Aldrich, St. Louis, MO, USA
Sodium hydroxide (NaOH)	Merck, Darmstadt, Germany
Sodium orthovanadate (Na_3VO_4)	Sigma-Aldrich, St. Louis, MO, USA
SYBR Green	Bio-Rad, Hercules, CA, USA
TEMED	Bio-Rad, Hercules, CA, USA
Tetrasodium pyrophosphate ($Na_4P_2O_7$)	Sigma-Aldrich, St. Louis, MO, USA
Tris(hydroxymethyl)aminomethane (TRIS)	Acros Organics / Thermo Fisher Scientific
TRIS-HCl	Carl Roth, Karlsruhe, Germany
Triton X-100	Carl Roth, Karlsruhe, Germany
TRIzol reagent	Ambion, Kaufungen, Germany
Tween 20	Sigma-Aldrich, St. Louis, MO, USA
Western Lightning ECL plus	PerkinElmer, Waltham, MA, USA
Western Lightning ECL ultra	PerkinElmer, Waltham, MA, USA
Xylene	AppliChem, Darmstadt, Germany

In the following the recipes for all self-made solutions are listed. 5/10x solutions were pre-diluted to the operating concentration with distilled water.

Table 4. Buffers and Solutions

Designation	Composition
Blocking solution	5 % (w/v) 10 g milk pPowder in , 200 mL TBS-T
Citrate buffer	10 mM citric acid monohydrate, pH 6.0
Laemmli buffer 5x	225 mM TRIS-HCl pH 6.8, 50% (v/v) Glycerol, 5% (w(v) sodium dodecyl sulfate (SDS), 100 mM dithiothreitol (DTT) + 0.02% (w/v) bromophenol blue, + 0.2% (v/v) 2-mercaptoethanol

Lysis buffer ready-to-use	100 µM PMSF, 100 µM sodium orthovanadate, 1x cOmplete Protease Inhibitor Cocktail in lysis buffer stock
Lysis buffer stock	50 mM HEPES, 150 mM sodium chloride (NaCl), 1 mM EGTA, 10 % (v/v) glycerol, 1 % (v/v) Triton X-100, 100 mM sodium fluoride (NaF), 10 mM tetrasodium pyrophosphate ($Na_4P_2O_7$), pH 7.5 – 7.9
PBS-Tx	PBS, 0.01 % (v/v) Triton X-100
Phosphate buffer (PB)	17 mM monobasic sodium phosphate, 60 mM dibasic sodium phosphate, adjust to pH 7.4
Phosphate-buffered saline (PBS)	137 mM NaCl, 2.7 mM KCl, 1.8 mM KH_2PO_4,10 mM Na_2HPO_4, adjust to pH 7.2-7.4
Running buffer 10x	25 mM Tris, 190 mM glycine, 0.1 % (w/v) SDS
SDS Separating gel solution, (X %)	x % (v/v) Acrylamide, 375 mM Tris (pH 8.8), 0.1 % (w/v) SDS, 0.1 % (w/v) APS, 0.04 % (v/v) TEMED
Stacking gel solution	5 % (v/v) acrylamide, 125.5 mM Tris (pH 6.8), 0.1 % (w/v) SDS, 0.1 % (w/v) APS, 0.1 % (v/v)
TBST	0.2 M Tris base, 1.5 M NaCl, 0.05 % (v/v) Tween 20
TE buffer 10x	10 mM Tris-HCl (pH 8.0), 1 mM EDTA (pH 8.0), pH 9
TRIS-buffered saline (TBS)	0.2 M Tris base, 1.5 M NaCl, pH 7.4 – 7.6

2.2 Methods

2.2.1 Cell culture

2.2.1.1 Established pancreatic cancer cell lines

This study evaluated the established pancreatic cancer cell lines MiaPaCa2, PANC1, L3.6, CAPAN1 and CAPAN2. All cell lines were kindly provided by the Clinic for General, Visceral and Pediatric Surgery of the University Medical Center Göttingen, Germany. Furthermore, we utilized the KPC (*Kras*^{G12D}; *Trp53*^{R172H}; *PDX Cre*) genetically engineered mouse model, provided by the Ellenrieder Lab. Histopathological features and tumor grading of KPC tumors were examined by Prof. Dr. Ströbel (Head of department of Pathology, University Medicine Göttingen). The corresponding growth media to each cell lines is indicated in Table 5.

Table 5. Cell line specific media

Cell line	Origin	Media Composition

CAPAN1	Human	RPMI, 10 % (v/v) FCS, 1% (v/v) penicillin/streptomycin solution
CAPAN2	Human	RPMI, 10 % (v/v) FCS, 1% (v/v) penicillin/streptomycin solution
L3.6	Human	MEM, 10 % (v/v) FCS, 1% (v/v) penicillin/streptomycin solution
PANC1	Human	DMEM, 10 % (v/v) FCS, 1% (v/v) penicillin/streptomycin solution
MiaPaCa2	Human	DMEM, 10 % (v/v) FCS, 1% (v/v) penicillin/streptomycin solution
GCDX-5	Human	KSF medium, 2% (v/v) FCS, 1% (v/v) penicillin/streptomycin solution, 50 µg/µL bovine pituitary extract and 0.05 ng/mL recombinant human epidermal growth factor.
GCDX-57	Human	KSF medium, 2% (v/v) FCS, 1% penicil-lin/streptomycin solution, 50 µg/µL bovine pituitary extract and 0.05 ng/mL recombinant human epidermal growth factor.
CDX-62	Human	KSF medium, 2% (v/v) FCS, 1% penicil-lin/streptomycin solution, 50 µg/µL bovine pituitary extract and 0.05 ng/mL recombinant human epidermal growth factor.
GCDX-62	Human	KSF medium, 2% (v/v) FCS, 1% penicil-lin/streptomycin solution, 50 µg/µL bovine pituitary extract and 0.05 ng/mL recombinant human epidermal growth factor.

The CRISPR dcas9 generated ROBO3 deficient clones in PANC1 and MiaPaCa2 were treated additionally with 1 µg/ml puromycin (Thermo Fisher Scientific, Waltham, MA, USA), to undergo a selection process.

The cell lines were cultivated in incubators at 37°C and 5% CO_2. At the time of confluence, the medium was aspirated, washed once with 1x Phosphate-buffered saline (PBS) and then separated by trypsin/EDTA. After complete detachment from the cell culture plate, trypsinization was blocked by the addition of culture medium and mixture of the cells. After centrifugation at 300 g for 3 minutes (min) and resuspension in fresh medium, the cells were reseeded and reused, either for continuous cultivation or in culture vessels for experiments.

2.2.1.2 Cell lines established from patient-derived xenografts

The cell lines of the Patient-Derived Xenograft (PDX) were provided by the KFO 5002. Briefly, the PDX mouse model was generated by utilizing surgically resected PDA specimens from patients with written consent at the UMG and the Comprehensive Cancer Center, Ruhr-University Bochum. The ethics committee of the UMG (permission no. 70112108) and Ruhr University Bochum (permission no. 3534-9, 3841-10, 16-5792) approved the study. PDA tumor biopsies were implanted in the flanks of immunocompromised mice. After 4-5 weeks post xenograft implantation, these tumors were isolated and re-implanted for further

expansion for at least three to four generations. All animal experiments were performed following the guidelines of the local Animal Use and Care Committees at the Ruhr University Bochum (8.87-50.10.32.09.018) and the UMG (14/1634, 18/2953). The corresponding PDX tumors were harvested, and subsequently primary tumor cells were isolated as described previously (Patil et al. 2020). As shown in Figure 9, the PDX tumor implantation and isolation of the corresponding primary PDX cell lines were conducted by the lab of Prof. Elisabeth Hessmann and Prof. Volker Ellenrieder in the frame of the KFO 5002 (Department of Gastroenterology and Gastrointestinal Oncology, University Hospital Göttingen, Germany). Primary pancreatic tumor cells (GCDX cells) were maintained in type I collagen-coated plates for three to four passages. GCDX cells were transferred to the normal culture flask and maintained in Keratinocyte-SF medium (KSF).

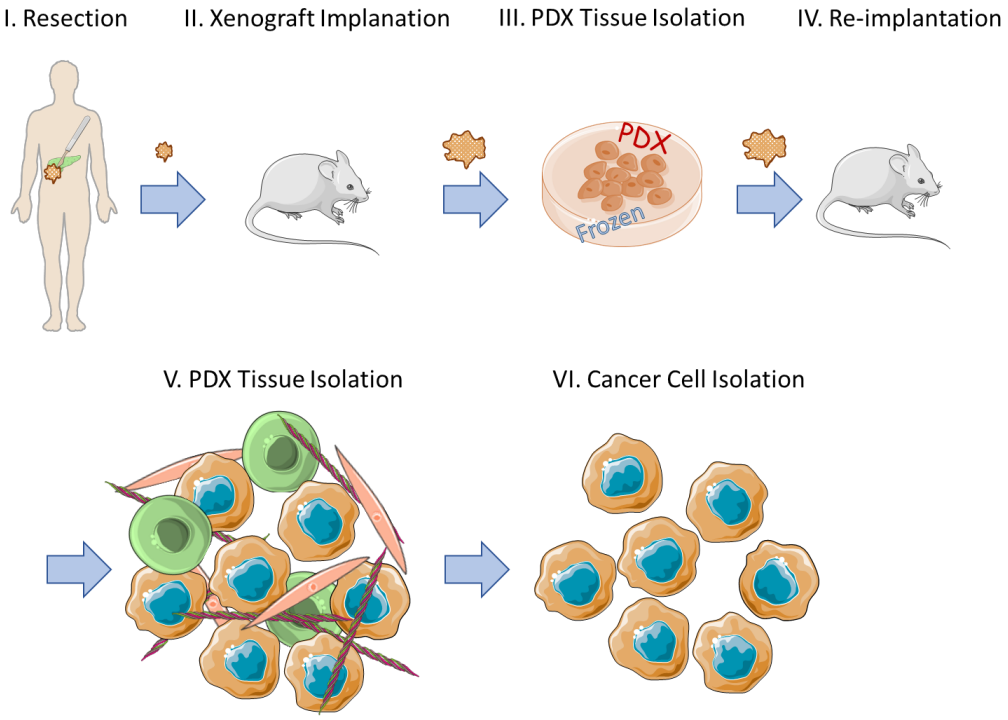

Figure 9. Establishment of cell lines from patient-derived xenografts. Representation of the process of generating cell lines from patient resection material. I) Tumor tissue is obtained from pancreatic carcinoma resection material. II) The tissues are implanted subcutaneously into immunocompromised mice and cultured until a larger tumor is formed. III) The patient's subcutaneous xenograft tumor (PDX) is isolated and frozen for preservation. IV) Reimplantation of PDX tissue into new mice and cultivation over a period of time until sufficient old material is available. V) PDX tumor tissue isolation, which comprises not only tumor cells (orange), but also fibroblasts (red), extracellular matrix (grey) and other stromal cells (green). VI) A pure tumor culture is generated from the heterogeneous tissue, which has been determined for use in experiments. Illustration was created using Servier Medical Art.

2.2.1.2.1 CRISPR/dCas9

The CRISPR (Clustered Regularly Interspaced Short Palindromic Repeats) -dCas9 method is based on a natural system used by bacteria to protect themselves from infection by viruses.

CRISPR/Cas9 can be used to manipulate the genome and regulate the expression of different target genes. For that purpose, a chimeric single guide RNA (sgRNA) can be engineered, which pairs to the target gene sequence of interest (18- to 25bp). The sgRNA- binding site must be located near a short DNA motif termed the protospacer-adjacent motif (PAM) (Jinek et al. 2012). The double-stranded breaks activate the DNA repairing systems of the cell. Two different repairing pathways can be utilized: Non-Homologous End Joining (NHEJ) or homology directed repair. Both processes have an error capability that leads to an induction of insertions or deletion mutations (indels) during the repair process, leading to the loss of the target gene sequence (Hsu et al. 2014).

In 2013, Qi et al. mutated the nuclease domains of Cas9 from *S. pyogenes* to generate a nuclease-deficient Cas9 (dCas9) (Qi et al. 2013). Thus, dCas9 can modulate the transcription of any gene without cleaving the DNA and genetically altering the target sequence (Qi et al. 2013). Even though this deficient version of Cas9 is not capable of cleaving DNA, it can still target and bind DNA with the same precision when guided by sgRNA (Moradpour and Abdulah 2020). However, instead of irreversibly altering the genome like the standard CRISPR/Cas9 system, which is based on the induction of double-strand breaks in DNA by Cas9 endonuclease activity, binding of dCas9 interferes transcription at the target site, resulting in reversible silencing of the gene (Moradpour and Abdulah 2020). The use of the dCas9 protein allows targeting endogenous gene expression by controlling RNA polymerase activity or modulating promoter accessibility when fused to transcription factors (Chen et al. 2013).

The guide RNA constructs for this study were designed and provided by Dr. Xingbo Xu (University Medical Center Goettingen, Department of Cardiology and Pneumology).

The constructs utilized to generate a dCas9-based ROBO3 knockdown are indicated in Table 6.

Table 6. Constructs for dCas9-based ROBO3 silencing

Construct	Catalog-No.	Company
pSLQ1658-dCas9-EGFP vector	51023	Addgene, Watertown, Massachusetts, USA
Cas9 sgRNA vector	68463	Addgene, Watertown, Massachusetts, USA

Table 7. ROBO3 sgRNA constructs

ROBO3 sgRNA	Sequence
#1	GGGACTCCGGCACTAGGGGG
#2	CCCCTAGTGCCGGAGTCCCC
#3	TTCTCTCCACCCCCTAGTGC
#4	CCACGGTGCCGCTCTCCTGC

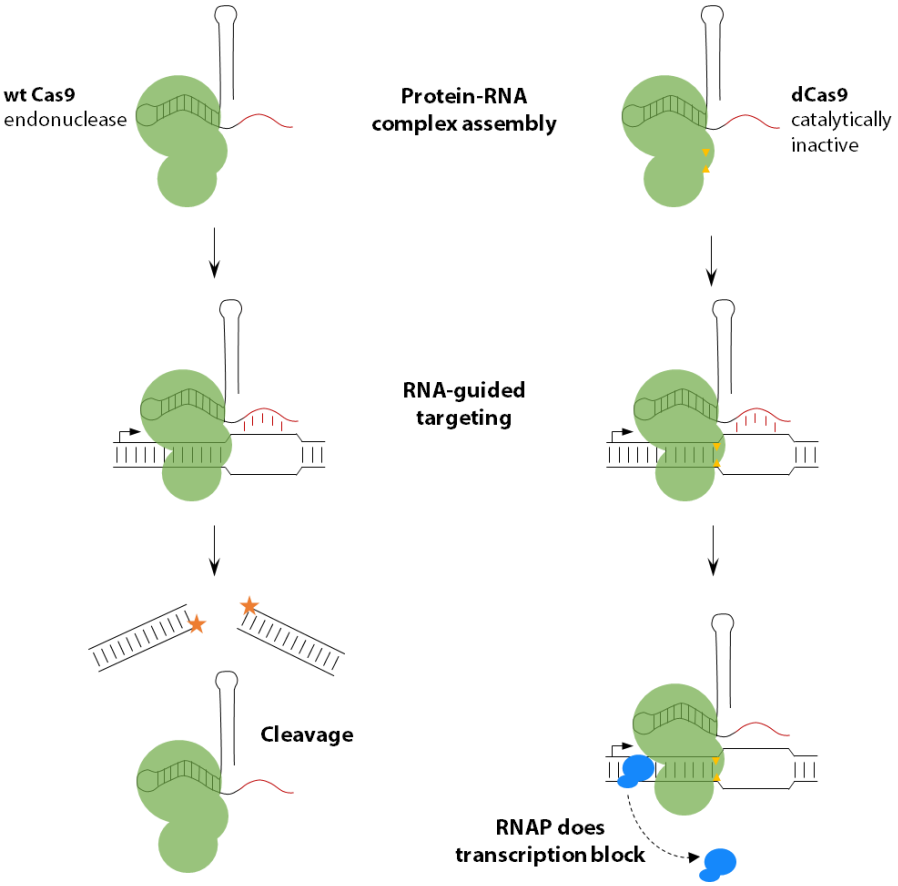

Figure 10. Difference between the dCas9 and Cas9 regulated CRISPR system. By binding to the sgRNA, the wild-type Cas9 protein forms a protein-RNA complex. This complex binds to specific DNA targets by base pairing between the sgRNA and the DNA target. In the case of wild-type Cas9, the DNA is cleaved due to the nuclease activity of the Cas9 protein and thus transcription is interrupted, while the dCas9 is still able to form a complex with the sgRNA and bind to a specific DNA target, but it blocks RNA polymerase and transcript elongation. Modified after Qi et al. 2013 (Qi et al. 2013) with the permission and RightsLink Printable License of Cell Press.

Transfection of the cell lines was performed in the following manner:

For the transfection of the CRISPR/dCas9 constructs 200.000 cells per well were seeded in a 6-well plate. The transfection was performed the following day. As control the dCas9-EGFP vector in combination with the sgRNA-*LacZ* was used. For the different knockdown reaction approaches the different sgRNA for *ROBO3* (#1, #2, #3, #4) were combined with dCas9-EGFP vector. All components were used at a concentration of 1 μg/μL. The reaction mix for one well contained the sgRNA (1 μg), the dCas9-EGFP vector (1 μg) and 5 μL Lipofectamine™ 2000, mixed in 500 μl Opti-MEM™ in a polystyrol falcon and incubated for 20 minutes at room temperature. The mixture was added into the well and supplemented with 1500 μL growth media. The medium was changed after one day, and the transfected cells were then selected by using puromycin (1 μg/μl).

2.2.1.2.2 siRNA mediated knockdown

For a transient knock-down, PDA cells were seeded in 6-well plates and transfected with either 20 nM siRNA against ROBO3, AXL, STAT3 or control siRNA (indicated in Table 8). For the transfection siLentFect™ lipid reagent were used following manufacturer's instructions. Briefly, for one well siRNA was mixed with the corresponding transfection reagent and 500 μl OptiMEM and incubated for 20 min at room temp. In the well the transfection mix was supplemented with 1500 μl growth media. After 48-72 h, protein and RNA were extracted for the analysis.

Table 8. Oligonucleotides used for siRNA mediated knockdown

All targeting siRNAs were purchased by Thermo Fischer Scientific (Waltham, MA, USA). The negative Control siRNA was purchased by Applied Biosystems(Waltham, MA, USA).

OligonucleotideTarget	**Sense (5´→3´)**	**Antisense (5´→3´)**	**siRNA ID**
siRNA AXL #1	GGGUG-GAGGUUAUCCUGAAtt	UUCAGGAUAAC-CUCCACCCtc	s1846
siRNA AXL #2	CAGCGAGAU-UUAUGACUAUtt	AUAGUCAU-AAAUCUCGCUGtt	s1847
siRNA ROBO3 #1	CGGUGCAA-GACUCAAGGAAtt	UUCCUUGAGUCUU GCACCGtc	241788

siRNA ROBO3 #2	GCAAAGUACUGUG-CUAAGAtt	UCUUAG-CACAGUACU-UUGCtg	s34572
siRNA ROBO3 #3	GGAACCAAGAU-GACCCUUGtt	CAAGGGUCAU-CUUGGUUCCtc	29905
Silencer® Negative Control #1 siRNA Negative			AM4611
siRNA STAT3 #3	GCACAAUCUAC-GAAGAAGAAUCtt	GAUUCUUCGUA-GAUUGUGCtg	116558

2.2.1.3 CRISPR dCas9 mediated overexpression of ROBO3

As described above, the CRISPR/ dCas9 system can be used not only for reversible inhibition of gene expression, but also for overexpression by modulating promoter accessibility. In this work, we used this system to target ROBO3 overexpression

The constructs for this study were provided by Dr. Florian Wegwitz (University Medical Center Goettingen, Department of Gynecology).

The following constructs were utilized to generate a dCas9-based ROBO3 overexpression:

Table 9. Constructs for dCas9-based ROBO3 overexpression

Construct	Catalog-No.	Company
pcDNA-dCas9-p300 Core vector	61357	Addgene, Watertown, Massachusetts, USA
pcDNA-dCas9-p300 Core (D1399Y) vector	61358	Addgene, Watertown, Massachusetts, USA
pSPgRNA vector	47108	Addgene, Watertown, Massachusetts, USA

Table 10. ROBO3 sgRNA constructs

ROBO3 sgRNA	Sequence
3.1	TCTAGTGTCCTTACGGCCCT
4.1	GGCTCGGATTTATGTCTTCCC
5.1	GCTTCTGCCCAACTTTAGAAC

Transfection of the cell lines was performed in the following manner:

For the transfection of the CRISPR/dCas9 constructs 500.000 cells per well were seeded in a 6-well plate. The transfection was performed the following day. As control pcDNA-dCas9-p300 Core (D1399Y) vector with the sgRNA was used. For the different overexpression reaction approaches the different sgRNA for *ROBO3* (3.1, 4.1 and 5.1) were combined with pcDNA-dCas9-p300 Core vector. The reaction mix for one well contained the sgRNA (700 ng), the pcDNA-dCas9-p300 Core vector (2µg) and 7,5 µL Lipofectamine™ 2000, mixed in 500 µl Opti-MEM™ in a polystyrol falcon and incubated for 20 minutes at room temperature. The mixture was added into the well and supplemented with 1500 µL growth media. The medium was changed after one day, and the transfected cells were then harvested after 48 hours.

2.2.1.4 Cryopreservation of cells

For the cryopreservation of cell lines, cells were trypsined and aliquots of the cells were resuspendend in freezing media (10 % (v/v) DMSO in FCS) . To ensure slow cooling (1 °C per minute), the cryogenic vessels were stored overnight at -80°C in a cryocontainer ("Mr. Frosty"). For long term storage, cell stocks were transferred in liquid nitrogen.

2.2.1.5 Thawing of cells

The cell stocks were thawed in a water bath (37°C), resuspended in the corresponding culture medium, then centrifuged (300 g, 3 min, RT), the supernatant was removed, resuspended in culture media and then transferred and incubated at 37°C and 5 % CO_2 in a cell culture flask.

2.2.1.6 Cell counting

In order to calculate the exact amount of cells for certain experiments, a hemocytometer with a Neubauer classification was used. Therefore, a defined volume of the cell suspension, was applied to the Neubauer chamber, all four corner quadrants were counted. To determine the cell count per milliliter, the number was divided by four and then multiplied by the dilution and the factor 10,000.

2.2.2 *In vitro* Cell Treatments

For all experiments, the cells were seeded in order to reach a confluence of 60 - 80% at the beginning of treatment.

Interleukin 6 (PeproTech, Rocky Hill, NJ, USA) was dissolved in water and 10 % (w/v) trehalose. Cells were treated with 50 nM IL-6 or control (solvent without IL-6) for the indicated periods mentioned in the results.

The STAT3 inhibitor napabucasion (Tocris Bioscience, Bristol, United Kingdom) and the AXL inhibitors bemcentinib or BGB 324 (Selleck Chemicals Llc, Houston, Texas, USA) were dissolved in DMSO. As treatment control an equal volume of DMSO was used. Cells were treated with different concentrations for the indicated periods of time before harvesting protein or RNA.

2.2.2.1 Harvesting of Cells

2.2.2.1.1 Protein isolation from cell lines

To obtain protein material from total cell lysate, the cells were first washed with PBS. Depending on the desired experiment, around 65 µL/200 µL of the lysis buffer was added per 6-well/10cm dish. After a short incubation time on ice, the cells were and transferred into a reaction tube. After 30 minutes incubation on ice the lysates were centrifuged at 4°C, 17,000 g for 25 minutes. After centrifugation, the supernatant, containing the proteins, were transferred to a new tube and either processed directly or stored at -80°C for later use.

2.2.2.1.2 Determination of protein concentration

Protein Assay Dye Reagent Concentrate (Bio-Rad, Hercules, CA, USA) was used to measure protein concentration according to the manufacturer's instructions. Briefly, 200 µL of the dye reagent was added to each well of a 96-well plate and then mixed with 1 µL of the protein sample. Samples and standards were measured in duplicates. For the quantitative measurement of the protein concentration a standard curve was used, with a series of BSA protein dilutions (1, 2, 4, 6 µg) in the cell lysis buffer. For concentration determination, absorbance at 595 nm was measured in a photometer and calculated with the help of the standard curve.

2.2.2.1.3 RNA isolation

RNA extraction was performed via phenol-chloroform extraction using TRIzol (ThermoFisher Scientific, Waltham, MA, USA) reagent. After aspiration of the medium 700 µL TRIzol reagent was added per well in a 6 well culture plate. The cells were lysed in the reagent and transferred into a tube, 200 µL chloroform was added, the solution vortexed and incubated for 5 minutes at room temperature. The mixture was centrifuged for 15 minutes (17000 g, 4 °C). The upper aqueous phase was transferred to new tube and isopropanol was added

in a 1:1 ratio. After incubation at room temperature for 10 minutes, the samples were centrifuged for 30 minutes at 17,000 g and 4 °C, followed by discarding the supernatant. The pellet was washed twice by adding 500 µl of 75 % ethanol, centrifuging (17000 g and 4°C) for 5 minutes and discarding the supernatant. Following the second wash step, the pellet dried for about 30 minutes. Finally, the pellet was resuspended in a suitable volume of nuclease-free water (~30 µL). To determine the RNA concentration and purity, the samples were measured at 230, 260 and 280 nm with a nano photometer P330 (Intas Science Imaging, Göttingen, Germany).

2.2.2.2 Immunoblot analysis

For the separation of proteins, Sodium Dodecyl Sulfate Poly Acrylamide Gel Electrophoresis (SDS-PAGE) was performed. The Mini-PROTEAN Tetra Cell System (Bio-Rad, Hercules, CA, USA) was used to perform gel preparation, gel electrophoresis. First, the SDS gels were prepared with 7.5-, 10-, or 15-percentage of acrylamide separation gel solutions, depending on the protein size examined. The protein lysates (produced as described in 5.2.2.1.1) were diluted, in Whole Cell Lysate buffer with 1x Laemmli, to a final concentration of 1 µg/µL protein. Afterwards, samples were heated at 95°C for 5 minutes. The gels were then transferred to an electrophoresis chamber which was filled with running buffer. A protein marker PageRuler Plus Prestained Protein Ladder (Thermo Fisher Scientific, Waltham, MA, USA) was used for later assignment of the molecular weight. After boiling, the protein samples were loaded on the polyacrylamide gel. The electrophoresis was conducted in running buffer at 100 V for about 30 minutes until the samples had passed the collecting gel. Then the electrophoresis was performed at 160 V until completion. Once the proteins had been successfully separated, they were transferred to a nitrocellusose (NC) membrane by using a Trans-Blot Turbo Transfer System (Bio-Rad, Hercules, CA, USA). Filter paper and the nitrocellulose membrane were moistened with blotting buffer (Turbo-Blot-Puffer, Bio-Rad, Hercules, CA, USA) according to manufacturer's protocol. Upon completion of 25 minute blotting with 25 Volt, the transfer can be checked by staining with Ponceau S and then destained by washing with TBS-T. Subsequently membranes were blocked in 5% (w/v) powdered milk in TBS-T for one hour on a shaker at room temperature and then washed shortly with TBS-T to remove the blocking solution. Primary antibodies (see table 7) were applied overnight in a 5% (w/v) milk solution and the appropriate antibody in different concentrations, in 4 °C on a shaker. The following day, the membranes were first washed three times with TBS-T for 10 minutes while shaking and then incubated with a primary antibody-spe-

cific, horseradish peroxidase (HRP)-linked secondary antibody for a further 60 minutes. After repeated three washes of 10 minutes with TBS, the proteins were incubated with Enhanced Chemiluminescence Reagent (ECL-) developer solution for 10- 60 seconds, before being detected with the ChemoCam Imager (Intas Science Imaging, Göttingen, Germany).

Table 11. Primary antibodies used for immunoblot analysis

Target	Origin	Company	Catalog-No.	Dilution
AXL	rabbit	Cell signaling technologies, Danvers, MA, USA	8661	1:1000
HNF 1α	mouse	Santa Cruz, Dallas, Texas, USA	sc-393925	1:1000
HRP-linked β-Actin		Sigma-Aldrich, St. Louis, MO, USA	A3854	1:40000
Keratin 81	mouse	Santa Cruz, Dallas, Texas, USA	sc-100929	1:1000
KLF5	mouse	Sigma-Aldrich, St. Luis, MO, USA	SAB4200338	1:1000
pSTAT3	rabbit	Cell signaling technologies Danvers, MA, USA	9145	1:1000
pSTAT3	rabbit	Abcam Cambridge, UK	ab76315	1:1000
ROBO3	goat	Abcam, Cambridge, UK	ab77261	1:1000
ROBO3	goat	R & D Systems, Minneapolis, Minnesota, USA	AF3076	1:1000
Sox2 cterm	rabbit	Abcam Cambridge, UK	ab97959	1:1000
STAT3	mouse	Cell signaling technologies, Danvers, MA, USA	9139	1:1000
Wnt10a	rabbit	Sigma-Aldrich, St. Louis, MO, USA	ABS456	1:1000
Wnt10a	rabbit	Novus Biologicals, Centennial, Colorado, USA	NBP1-76916	1:1000
ZEB1	rabbit	Merck Millipore, Burlington, MA, USA	ABN285	1:1000

Table 12. Secondary antibodies used for immunoblot analysis

Target	Origin	Company	Catalog-No.	Dilution

HRP-linked anti-goat	Santa Cruz, Dallas, Texas, USA	sc-2020	1:5000
HRP-linked anti-mouse IgG	Cell signaling technologies, Danvers, MA, USA	7076S	1:7000
HRP-linked anti-rabbit IgG	Cell signaling technologies, Danvers, MA, USA	7074S	1:7000

2.2.2.3 cDNA Synthesis

Synthesis of cDNA from previously isolated RNA (as mentioned in 4.5.1.3) was accomplished with the iScript cDNA Synthesis Kit (Bio-Rad Laboratories, Hercules, USA) in accordance with the manufacturer's instructions. The cDNA was either used immediately for experiments or stored at -20°C until further use.

2.2.2.4 Real-time quantitative PCR analysis

RT-qPCR analysis was performed by using the fluorescent dye SYBR Green (Bio-Rad, Hercules, CA, USA) on a StepOnePlus real-time system (Applied Biosystems, Foster City, CA, USA) to quantify mRNA expression The reaction mix for one well consist of 5 µL SYBR Green (Bio-Rad, Hercules, CA, USA), 0.25 µL forward and reverse primers (10 µM each), 3.5 µL nuclease-free water and 1 µL cDNA (conc. 1 µg/µL) were added for each reaction. Then the RT-qPCR analysis was carried out using a comparative Ct calculation relative to the housekeeping gene *Rplp0* for quantification. The data analysis (e.g., the relative quantification values [RQ] calculation) was performed with the help of the corresponding StepOnePlus software v2.3 (Applied Biosystems, Foster City, CA, USA). The primers (Table 13) were obtained from Sigma-Aldrich (St. Louis, MI, USA).

Table 13. Human primers used for RT-qPCR analysis

Target		Sequence (5'-3')
A2ML1	Forward	CTAGGAATGTTGGCCCTATCACC
	Reverse	CCAAACAAACCTTCTGAACGGAG
AGR2	Forward	GTCAGCATTCTTGCTCCTTGT
	Reverse	GGGTCGAGAGTCCTTTGTGTC
ALDH1B	Forward	CCCATTCTGAACCCAGACATC
	Reverse	AATGACCTCCCCGGTGGTA

AXL	Forward	GTGGGCAACCCAGCGAATATC
	Reverse	GTACTGTCCCGTGTCGGAAAG
CAPN8	Forward	TGGCTCCAACCAAAACGCTT
	Reverse	CCTGGTCCAAGATCCTTGTAGC
CDC42	Forward	CCATCGGAATATGTACCGACTG
	Reverse	CTCAGCGGTCGTAATCTGTCA
cMET	Forward	AGCAATGGGGAGTGTAAAGAGG
	Reverse	CCCAGTCTTGTACTCAGCAAC
ERBB3	Forward	GGTGATGGGGAACCTTGAGAT
	Reverse	CTGTCACTTCTCGAATCCACTG
FAM83A	Forward	GGCCCTAAGGGACTGGACT
	Reverse	CACAGTGGCGCTGGATTTTT
KRT5	Forward	CCAAGGTTGATGCACTGATGG
	Reverse	TGTCAGAGACATGCGTCTGC
MAPKBP1	Forward	CTGTGGAAGGGTCAACCATTAC
	Reverse	GTCCTCTCGTCGGTTTCCTG
Nestin	Forward	CTGCTACCCTTGAGACACCTG
	Reverse	GGGCTCTGATCTCTGCATCTAC
PLEKHG 1	Forward	CTGCACCTGGACTTGACAG
	Reverse	CCAACAGCAGATCCGTGAAGA
ROBO3	Forward	GTAGGACCGGAGGACGCTAT
	Reverse	CCCCGTTCTTGTACCACTCA
SLC39A13	Forward	TCAGCGGCTACCTCAACCT
	Reverse	AGGAGCCCGATCTTCTTGCT
SOX2	Forward	GCCGAGTGGAAACTTTTGTCG
	Reverse	GGCAGCGTGTACTTATCCTTCT
TGFBI	Forward	CTTCGCCCCTAGCAACGAG
	Reverse	TGAGGGTTCATGCCGTGTTTC
TNC	Forward	TCCCAGTGTTCGGTGGATCT
	Reverse	TTGATGCGATGTGTGAAGACA

UHRF2	Forward	GGCACATCTACACAGATTGAGG
	Reverse	CAAGGCCGACATCTCTGGC
Rplp0	Forward	TGGGCAAGAACACCATGATG
	Reverse	AGTTTCTCCAGAGCTGGGTTGT

2.2.2.5 Viability Assay

The CellTiter- Glo Luminescent Cell Viability Assay (Promega, Madison, WI, USA) was used to quantify the viability of cell lines under various treatments. The Cell Viability Assay was conducted using the manufacturer's instructions. For each experiment, the cells were seeded in 96-well plates in triplicates and treated the following day with napabucasin, gemcitabine, BGB-324 or a vehicle control in monotherapy or in combination with different concentrations. After 48- or 72-hours incubation the CellTiter- Glo assay was performed. Viability was measured in relative light units (RLUs). Inhibitory concentration 50% (IC_{50})-Calculations were performed as described before (Hessmann et al. 2018).

2.2.2.6 Invasion assay

The invasion capacity was determined by the 3D-transwell Invasion assay. Therefore, 100,000 cells were seeded on a collagen-coated (collagen I, Rat-Tail, Enzo, Farmingdale, New York) transwell inserts (cell culture inserts, Falcon, Corning, New York, USA) with a pore size of 8 µm. The bottom of transwell inserts (8 µm) was coated with 50 µL collagen I solution (16 µL collagen I stock in 1 mL 0.1 M HCl). After collagen solidification, cells were mixed with 50 µL thawed Matrigel (Abcam, Cambridge, UK), and seeded into the transwell inserts. Cells were incubated for at least 30 min at 37°C. Next, culture medium was poured into the inserts (250 µL) and in the 24 well plates (750 µL) and incubated for 48 h at 37°C. Experiments were conducted in technical duplicates and biological duplicates. After incubation, the Matrigel was removed from the inner part of the inserts. The invaded cells, accumulated on the bottom surface of the transwell insert membrane, were fixed with 4 % PFA (paraformaldehyde) for 15 minutes and washed 2 times for 4 minutes with PB-buffer. The membranes were subsequently cut out and washed again 2 times for 4 minutes with PB-buffer. After blocking incubation for 1 hour at 4°C in PB-T (0.4 % (v/v) Triton X-100 in PB) supplemented with 10 % (v/v) normal goat serum (NGS; Abcam, Cambridge, UK), the membranes were incubated with the primary antibodies for 12 hours at 4°C in PB-T (0.4 % (v/v) Triton X-100, 2 % (v/v) NGS in PB). Following 3 washing steps for 4 minutes, the incubation with secondary antibodies was performed for 1 hour at 4°C in PB-T (0.4 % (v/v)

Triton X-100, 2 % (v/v) NGS in PB). Nuclear counterstaining was achieved with DAPI (0.5 μg/mL) in PB-buffer for one minute. Membranes were mounted by using Immu-Mount (Thermo Fisher Scientific, Waltham, Massachusetts, USA) and then analyzed with Olympus FluoView 1000 confocal microscope and FV10-ASW software version 4.2 (Olympus, Shinjuku, Japan). Total number of invading cells per 20x (magnification) field of view (F.o.V.) were manually counted by ImageJ software. For dCas9 ROBO3 related experiments total number of triple positive cells (DAPI, EGFP and ROBO3) in control samples and double positive (DAPI, EGFP) for ROBO3 knockdown samples, per 20x field of view (F.o.V.) in at least ten different images per biological repeat, were manually counted by ImageJ software.

Table 14. Primary antibodies and dilutions used for Invasion Assay

Name	Origin	Company	Catalog-No.	Dilution
ROBO3	goat	R & D Systems, Minneapolis, Minnesota, USA	AF3076	1:25
GFP	rabbit	Abcam, Cambridge, UK	ab13970	1:1000

Table 15. Secondary antibodies and dilutions used for invasion assay

Name	Origin	Company	Catalog-No.	Dilution
Anti-rabbit IgG Alexa Fluor 488	Donkey	Thermo Fisher Scientific, Waltham, MA, USA	A-11008	1:500
Anti-goat IgG Alexa Fluor 568	Donkey	Thermo Fisher Scientific, Waltham, MA, USA	A-11057	1:500

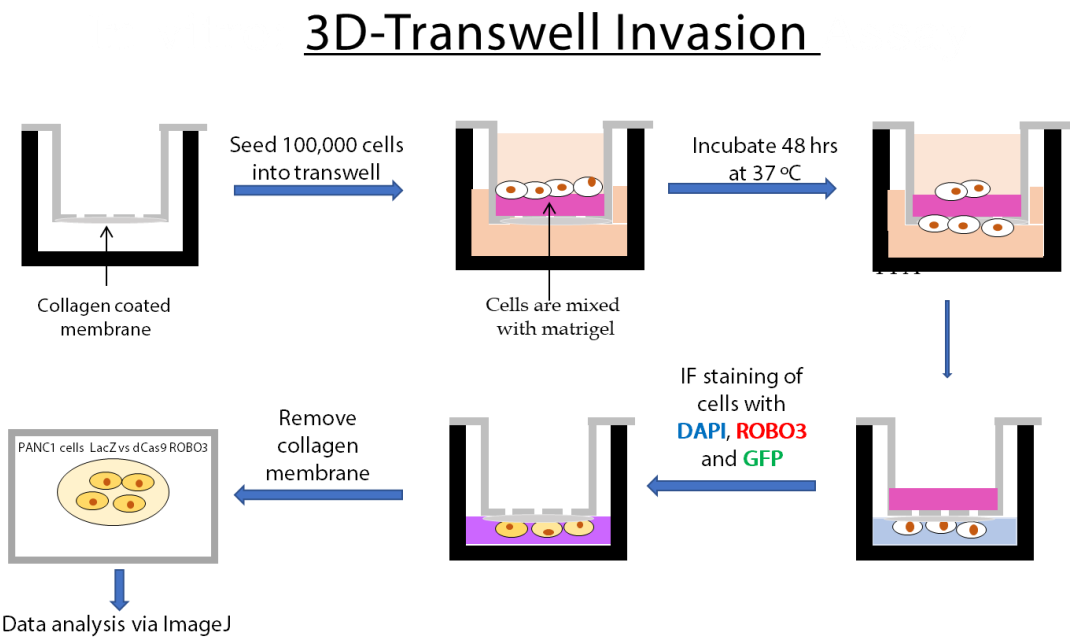

Figure 11. Schematic overview about 3D-Transwell Invasion Assay. Illustration of the different working steps for the 3-D Transwell Invasion Assay. First, 100,000 cells are seeded onto a collagen-coated transwell insert in matrigel solution. After 48 hours of incubation, the membrane is removed and stained for the indicated antibodies and then analyzed by immunoflourescence microscopy.

2.2.3 Histology

Murine and human PDA tissue specimens were fixed in 4 % (v/v) PFA. Formalin-fixed tissues were dehydrated by an automatic tissue processor (Leica Biosystems, Nußloch, Germany) and embedded in paraffin wax (Table 16). Subsequently, 4 µm thin sections were produced of the formalin-fixed paraffin-embedded (FFPE) tissues. Tissues were sectioned at a thickness of 4-5 µm.

Table 16. Different processing steps of the automatic tissue processor

Solvents	Duration (in hours)
Formalin	1:15
Alcohol 55%	0:30
Alcohol 85%	0:45
Alcohol 96%	1:00
Alcohol 100%	1:15
Alcohol 100%	1:10

Alcohol 100%	1:30
Xylol	0:20
Xylol	0:30
Xylol	1:10
Wax	0:30
Wax	0:45
Wax	1:30

2.2.3.1 Hematoxylin and eosin staining

The hematoxylin and eosin (H.E) staining was used to assess the overall histology of the tumor. For this purpose, the slide with the tissue was first deparaffinized and rehydrated by two-times incubation in ROTICLEAR® (Carl Roth, Karlsruhe, Germany) for 10 minutes. Subsequently, the tissue section was dehydrated in a descending alcohol series with 99 %, 85 %, 70 % and 50 % ethanol for 2 minutes each, then placed in distilled water for 5 minutes, followed by staining in hematoxylin solution for 6 minutes. Immediately afterwards, the tissue sections were incubated in flowing tap water for 8 minutes. After incubation in 0.2 % (v/v) acetic acid for five seconds, the sections were counterstained in eosin solution supplemented with 0.2 % (v/v) acetic acid for 3 minutes and then shortly washed in distilled water to wash off excess dye. A series of ascending alcohols dehydrated the freshly stained slides. Therefore, they were placed consecutively for 2 minutes in 50 %, 70 %, 85 % and 99 % ethanol. Finally, the slides were placed in ROTICLEAR® for two 10-minute periods and then mounted with RotiMount (Carl Roth, Karlsruhe, Germany) and a cover slip.

2.2.3.2 Immunohistochemistry

In order to visualize and quantify specific antibodies in tissue sections, immunohistochemical staining using the ABC (Avidin-Biotin-Complex) method was performed according to the following protocol. The slides were initially labelled with the appropriate antibody and the concentration used, then deparaffinized in ROTICLEAR® for two 10-minute periods, followed by rehydration in a descending ethanol series (99 %, 96 %, 80 %, 70 %, 50 %) for 3 minutes each. The rehydrated slides were then washed in distilled water. The slides were subsequently cooked for 15 minutes in the microwave in citrate buffer near boiling point, then cooled for 20 minutes on ice. Afterwards, the slides were rinsed in distilled water. The

endogenous peroxidase was blocked by treating the slides with 3 % H_2O_2 (hydrogen peroxide) for 10 minutes, then slides were shortly washed with distilled water. For further continuation of the staining, the slides were transferred to a Cadenza system, 600 µL PBS-Tween (PBS-T) were applied to the slide holder and the sections with the tissue side were placed on the slide holders bubble-free and transferred to the fixture. The slides were then washed twice with PBST for 5 minutes and thereafter non-specific binding was blocked by the application of 10% (v/v) BSA in PBS-Tween for one hour at room temperature. After one hour in 10% (v/v) BSA, the BSA solution was discarded, and the tissue incubated overnight at 4°C with the primary antibodies in 10% (v/v) BSA-containing PBS-Tween. The next day, the slides were rinsed four times with PBS-Tween for 5 minutes. Subsequently, the secondary antibody was added to the slides for one hour at room temperature in a dilution of 1:200 in 10% (v/v) BSA-containing PBS-Tween. The ABC complex (Vectastain ABC Standard Kit, Catalog-No. PK-4000, Vector Laboratories, Burlingame, CA, USA) incubates for 30 minutes prior use. Therefore, 2 µL Solution-A and 2 µL Solution B are mixed with 200 µL PBS-Tween per slide. Before applying the ABC solution for one hour at room temperature, the slides were previously rinsed with PBS-Tween four times for 5 minutes. Subsequently, the brown coloration of the ABC complexes was induced by DAB (ImmPACT® DAB Peroxidase Substrate Kit, Cat. No.SK-4105, Vector Laboratories, Burlingame, CA, USA), which forms a water-insoluble brown precipitate during oxidation. The DAB was applied to the preparation in a ratio of 30:1 with DAB diluent according to manufacturer´s protocol for an antibody specific time and then the reaction was stopped by tap water. Subsequently the counterstaining with hematoxylin was performed for 3- 5 minutes and immediately afterwards the slides were incubated under running tap water for 5 minutes. The dehydration of the slides was achieved by an ascending alcohol series. Therefore, they were kept in 50%, 70%, 85% and 99% ethanol for 2 minutes consecutively. Finally, the slides were placed in ROTICLEAR® for two 10-minute periods and mounted with RotiMount and a cover slip.

2.2.3.3 Immunofluorescence staining in tissues

To deparaffining the tissues, ROTICLEAR® was applied and the slides were incubated for 25 minutes, followed by a descending alcohol concentration series (99 %, 96 %, 80 %) and washing with distilled water for each 4 minutes. Afterwards the slides were washed 3 times for 4 minutes with PB-buffer and cocked in Citrate-buffer (pH 6.0) for 25 minutes in a microwave for antigen retrieval. After cooling for 15 minutes on ice the slides were washed with PB-buffer 5 times for 5 minutes and the tissue on the slides was surrounded by Liquid blocker super pap pen (Darko Pen; Darko, Jena, Germany), followed by further washing

with PB-buffer (5 times for 5 minutes). After a permeabilization and blocking incubation for 1.5 hours at 4°C in 0.4% (v/v) PB-T supplemented with 10% normal goat serum (NGS), the sections were washed thrice for five minutes each. Afterwards, the tissue was stained overnight with the primary antibodies for 12 hours at 4°C in 2 % (v/v) NGS-containing PB-T. Incubation with secondary antibodies was performed for 2 hours at 4°C in 2% (v/v) NGS-containing PB-T after washing with PB-buffer (6 times for 5 minutes). Nuclear counterstaining was achieved with DAPI (0.5 µg/mL). After two final PB washes, five minutes each, the stained tissue was fixed with Immu-Mount(Thermo Fisher Scientific, Waltham, Massachusetts, USA) and a cover glass.

Table 17. Primary antibodies used for immunofluorescence

Target	Origin	Company	Catalog-No.	Dilution
cMet	rabbit	Abcam, Cambridge, UK	ab74217	1:100
GFP	rabbit	Abcam, Cambridge, UK	ab13970	1:1000
IL-6	rabbit	Abcam, Cambridge, UK	ab6672	1:50
KRT81	mouse	Santa Cruz, Dallas, Texas, USA	sc-100929	1:100
pSTAT3 Y705	rabbit	Abcam, Cambridge, UK	ab76315	1:50
pSTAT3 Y705	rabbit	Cell signaling technologies Danvers, MA, USA	9145	1:50
ROBO3	goat	R & D Systems, Minneapolis, Minnesota, USA	AF3076	1:25
ROBO3	goat	Abcam, Cambridge, UK	ab77261	1:50
Sox2 c-term.	rabbit	Abcam, Cambridge, UK	ab97959	1:100

Table 18. Secondary antibodies used for immunofluorescence

Name	Origin	Company	Catalog-No.	Dilution
Anti-rabbit Alexa Fluor 488	Donkey	Invitrogen, Waltham, MA, USA	A-11008	1:500
Anti-goat Alexa Fluor 568	Donkey	Invitrogen, Waltham, MA, USA	A-11057	1:500

Anti-mouse Alexa Fluor 568	Donkey	Invitrogen, Waltham, MA, USA	A-21124	1:500

2.2.3.4 Immunofluorescence of cells

Immunofluorescence was used to detect the expression of various proteins in established human pancreatic tumor cells. For this purpose, the cells were seeded on cover slips and treated for a certain period of time. After incubation cells were fixed with 4% (v/v) PFA for 15 minutes and washed 4 times for 4 minutes with BP-buffer cover slips were blocked for 1 hour at 4°C in PB-T (PB containing 0.4% Triton X-100) supplemented with 10% (v/v) normal goat serum (NGS; Abcam, Cambridge, UK). Before the cells were stained overnight with the primary antibodies in 2% (v/v) NGS-containing PB-T, the cover slips were washed twice each for 4 minutes. On the following day, after three washing steps for 4 minutes, incubation with secondary antibodies was performed for 1 hour at 4°C in PB-T, 2% (v/v) NGS. Nuclear counterstaining was obtained with DAPI (0.5 µg/mL) in the BP buffer for 1 minute. The cover glasses were mounted with Immu-Mount (Thermo Fisher Scientific, Waltham, Massachusetts, USA) and then analyzed with the confocal microscope Olympus FluoView 1000 and the software FV10-ASW Version 4.2 (Olympus, Shinjuku, Japan). The number of positive stained cells per 20x field of view (F.o.V.) were manually counted by the ImageJ software.

Table 19. Antibodies used for immunofluorescence

Name	Origin	Company	Catalog-No.	Dilution
Anti-rabbit IgG Alexa Fluor 488	Donkey	Invitrogen, Waltham, MA, USA	A-11008	1:500
Anti-goat IgG Alexa Fluor 568	Donkey	Invitrogen, Waltham, MA, USA	A-11057	1:500
GFP	rabbit	Abcam, Cambridge, UK	ab13970	1:1000
cMet	rabbit	Abcam, Cambridge, UK	ab74217	1:100
pSTAT3	rabbit	Cell signaling technologies Danvers, MA, USA	9145	1:100
IL-6	rabbit	Abcam, Cambridge, UK	ab6672	1:100

2.2.4 Orthotopic PDA model

For the orthtoptic transplantation, of PANC1 cells into the pancreas, were used immunocompromised mice The Central Animal-experimental authority of University of Göttingen

approved the animal experiments. Animal experiments were performed according to the guidelines of the local Animal Use and Care Committees at the University Medical Center Göttingen (UMG) (permission no. 15/2057). One million cells per mouse were injected into the pancreas of NMRI Foxn1$^{nu/nu}$ mice under isoflurane inhalation anesthesia. For analgesia of the mice during the procedure, buprenorphine (trade name Buprenovet, Bayer Vital, Leverkusen, Germany; 100 µg/kg body weight, i.p. 30 min before surgery) and carprofen (trade name Carprieve, Nor-brook Laboratories, Newry, UK; 5 mg/kg body weight, s.c. during surgery) were administered, respectively. Thus, two different cohorts emerged, one cohort consisting of 8 NMRI Foxn1$^{nu/nu}$ mice received PANC1 Lacz control cells with intact ROBO3 expression and the other received PANC1 dCAs9 ROBO3 suppressed cells. After implantation, tumor growth was monitored weekly by ultrasound imaging as described before (Goetze et al. 2018). For the calculation of tumor volume, the height (x), width (y) and, by turning the animal by 90°, depth (z) of the tumor are measured. Assuming an ellipsoid shape of the tumor, the volume can be calculated as $4/3*\pi*$ (0,5*x)*(0,5*y)*(0,5*z). Mice were inspected daily and weighed 3 times weekly to document the health status of the mice. After detection of a tumor size greater than 8 mm diameter, the mice were sacrificed after 3 weeks and tumor tissues were collected. If the animals developed signs of a severe tumor burden or lost a massive amount of weight (more than 20% of body weight) prior to the defined end point, they were sacrificed before. The animals were sacrificed with a lethal Carbon dioxide inhalation (graduate fill) and cervical dislocation according to the animal welfare laboratory animal ordinance. Tumor, remaining normal pancreas, liver, spleen and lung tissue was isolated and fixed in formalin for histological analysis. In addition, a piece of tumor was frozen in liquid nitrogen for protein or RNA analysis and blood samples were collected.

2.2.5 RNA-Sequencing

To retrace alterations of the transcriptome after ROBO3 knockdown, RNA-Sequencing (RNA-Seq) was performed. For the analysis 3 independent biological replicates were used. Experiments were conducted in cells after siRNA (#3, ID: 29905, Thermo Fisher) mediated knockdown of ROBO3 or control treatment. After RNA quality measurement via agarose gel electrophoresis, 500 ng of total RNA and TruSeq RNA Library Prep kits (Illumina, RS-122-2001; RS-122-2002, San Diego, California, U.S.) was used for cDNA library preparation as per manufacturer's instructions. Qubit dsDNA high sensitivity assay was utilized for cDNA concentration measurement (Thermo Fisher, Q32854). Bioanalyzer high sensitivity DNA analysis (Agilent, 5067-4626) was used for DNA fragment size measurement prior to

sequencing (single-end 50bp). HiSeq2000 (Illumina, San Diego, California, U.S.) was performed at the Genomics core facility at UMG, Göttingen. The library preparation was realized with the aid of Lukas Klein. The detailed data analysis, including GSEA analysis, was conducted by Dr. Florian Wegwitz (Department of General, Visceral and Pediatric Surgery).

Sequencing data were processed in the GALAXY-environment provided by the Gesellschaft für wissenschaftliche Datenverarbeitung mbH Göttingen, the raw read quality was examined using FastQC v0.71 (https://www.bioinformatics.babraham.ac.uk/projects/fastqc/). After, hg38 human reference genome STAR v2.5.2b (Dobin et al. 2013) was utilized to align sequence reads. Next, the featureCounts program (version 1.6.0.2; (Liao et al. 2014), https://doi.org/10.1093/bioinformatics/btt656) was used to align the sequence reads, followed by DESeq2 v2.11.40.1 ((Love et al. 2014), https://doi.org/10.1186/s13059-014-0550-8) for differential gene expression.

2.2.6 Software

Table 20 showing the software used in this study.

Table 20. Software used in the study

Name	Usage	Company/Source
Adope Photoshop CS6	Image processing	Adobe Systems, San José, California (USA)
CellSence Micoscope	Light microscopy	Olympus, Shinjuku, Tokio (Japan)
ChemoStar Imager 3.2	Chemiluminescence	Intas Science Imaging, Göttingen (Germany)
Confocal microscope	IF	Olympus, Shinjuku, Tokio (Japan)
DESeq2 v2.11.40.1	RNA-Seq	Love et al. 2014
FastQC v0.71	RNA-Seq	Babraham Bioinformatics Institute, Cambridge (UK)
featureCounts program (version 1.6.0.2)	RNA-seq	Liao et al. 2014
GraphPad Prism® 6.01	Data processing	GraphPad Software, La Jolla, CA, USA)
ImageJ	Data processing and analysis	Developer Wayne Rasband, National Institutes of Health, Bethesda, Maryland, U.S.
Microsoft Office 2016	Text and data procesing	Microsoft, Redmond (USA)

NanoPhotometer PVC-Viewer	RNA concentration measurement	Intas Science Imaging, Göttingen (Germany)
PhoMo AutoSoft	Protein concentration measurement	Zhengzhou City (China)
STAR v2.5.2b	RNA-Seq	Dobin et al. 2013
Step One Plus Software v2.3	PCR	Thermo Fisher , Waltham, Massachusetts (USA)

2.2.7 Evaluation of the data

Statistical analysis and visualization of data were performed using GraphPad Prism version 6.01 for Windows (GraphPad Software, La Jolla, CA, USA), using an unpaired Student's t-test where applicable and not otherwise specified. Results were considered significant if p values were less than 0.05 and are indicated as such in the figures by asterisks (* $p \leq 0.05$, ** $p \leq 0.01$, *** $p \leq 0.001$, **** $p \leq 0.0001$)

3 Results

Pancreatic ductal adenocarcinoma is one of the most lethal human malignancies with dismal 5-years survival rate below 10 %, and it is estimated to become second leading cause of cancer-related death by end of 2030 (Siegel et al. 2019; Rahib et al. 2014). Pancreatic tumor heterogeneity is one of the key hallmarks in disease progression and treatment. Recently, it has been shown that ROBO3, potentially involve in pancreatic cancer progression. Furthermore, high expression of ROBO3 is associated with poor survival of pancreatic cancer patients (Biankin et al. 2012). However, the molecular and cellular mechanism involved in the regulation of ROBO3 signaling in pancreatic cancer progression remains elusive.

3.1 Subtype-specific expression of ROBO3 in pancreatic cancer

In order to analyze if ROBO3 shows a subtype dependent expression pattern, we used published RNA-seq data sets to compare its mRNA expression in human pancreatic cancer cell lines (Diaferia et al. 2016). Interestingly, we found increased ROBO3 expression in pancreatic cancer cell lines with a basal-like subtype (PANC1, MiaPaCa2 and PT45P1) compared to cell lines with a classical subtype (CAPAN1, CAPAN2, CFPAC1 and HPAF2) (Figure 12 A). To confirm increased ROBO3 expression at protein levels, we performed immunoblot analysis in different human PDA derived cell lines. While ROBO3 was absent or weakly expressed in classical cell lines such as CAPAN1 and CAPAN2, we identified high levels of the protein in basal-like cell lines (e.g. PANC1 and MiaPaCa2) (Figure 12 B). To further analyze the ROBO3 expression, we used tumor tissue provided by Mengyu Tu (AG Singh). She orthotopically injected classical (CAPAN1) and basal-like (MiaPaCa2) cells into the pancreas of nude mice. Thus, we could examine a consistency of ROBO3 levels as well as the cell line associated phenotypes. Notably, tumor cells with a classical phenotype formed well differentiated tumors with weak ROBO3 expression and low metastatic potential, as demonstrated in Figure 12. Conversely, implanted basal-like tumor cells developed poorly differentiated and highly metastatic cancers alongside with high expression levels of ROBO3. Moreover, liver metastases also exhibited high ROBO3 levels (Figure 12 C)

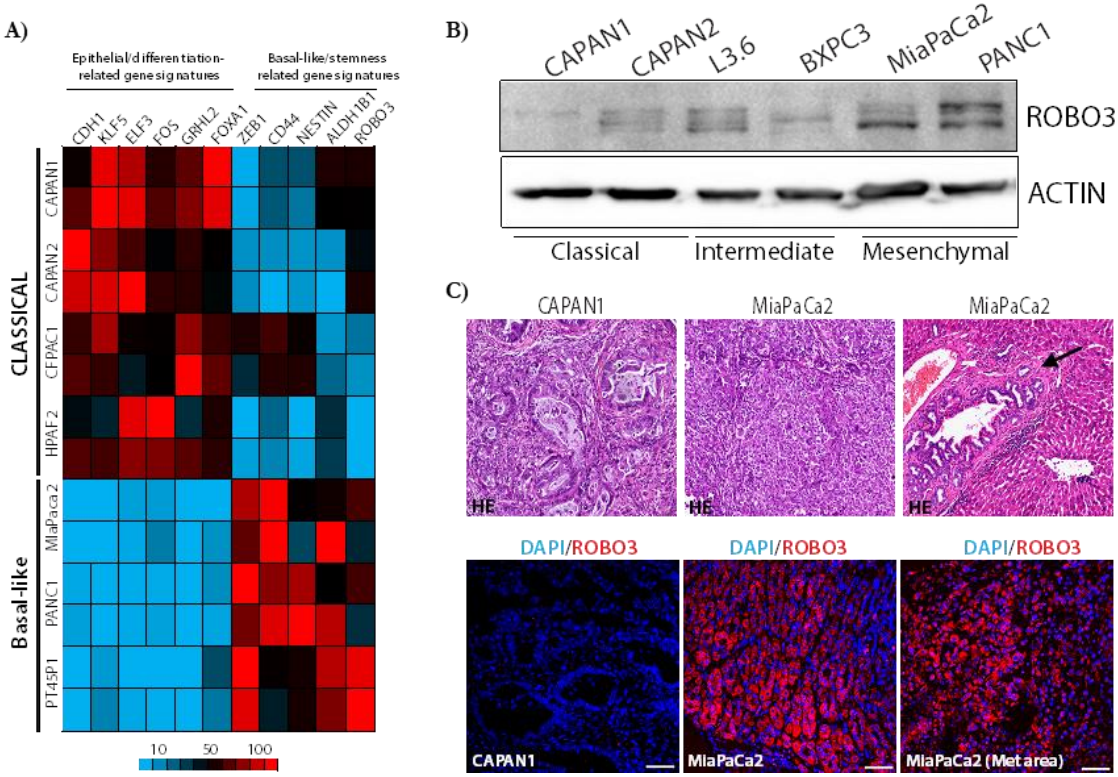

Figure 12. Subtype dependent ROBO3 expression in pancreatic cancer cell plasticity. A) Gene expression (RNA-seq published by Diaferia et al. 2016) analysis in classical and basal-like PDA cell lines. Differentially expressed classical and basal-like-related gene signatures are indicated in heatmap (indicated as FPKM value). Gene sets are marked in red for upregulated genes and in blue for downregulated genes. B) Immunoblot analysis of basal-like representing MiaPaCa2 and PANC1 cells as well as classical representing CAPAN1 and CAPAN2 cells, using indicated antibodies was performed. n = 3. C) Representative H.E staining and immunofluorescence (IF) staining were performed on orthotopic Capan1 and MiaPaCa2 primary tumor tissue and liver tissue. Scale bar 100 µM.

Furthermore, we examined the ROBO3 expression in the well-established genetically modified mouse model KPC. The KPC model harbors activating point mutation in *Kras*^{G12D} and dominant negative mutation in *p53*^{R172H} that are specifically inserted into mouse pancreas using Cre-Lox technology (Hingorani et al. 2005). Thereby, we differentiated the tumors based on the tumor grade. The grading and the staining for ROBO3 were performed in cooperation with Prof. Ströbel (Department of Pathology, University Medicine Göttingen). The comparison of low-grade (G1, G2) and high-grade (G3, G4) pancreatic tumors shows

that ROBO3 was predominantly expressed in poorly differentiated tumors and only marginally expressed in well differentiated G1/G2 tumors (Figure 13).

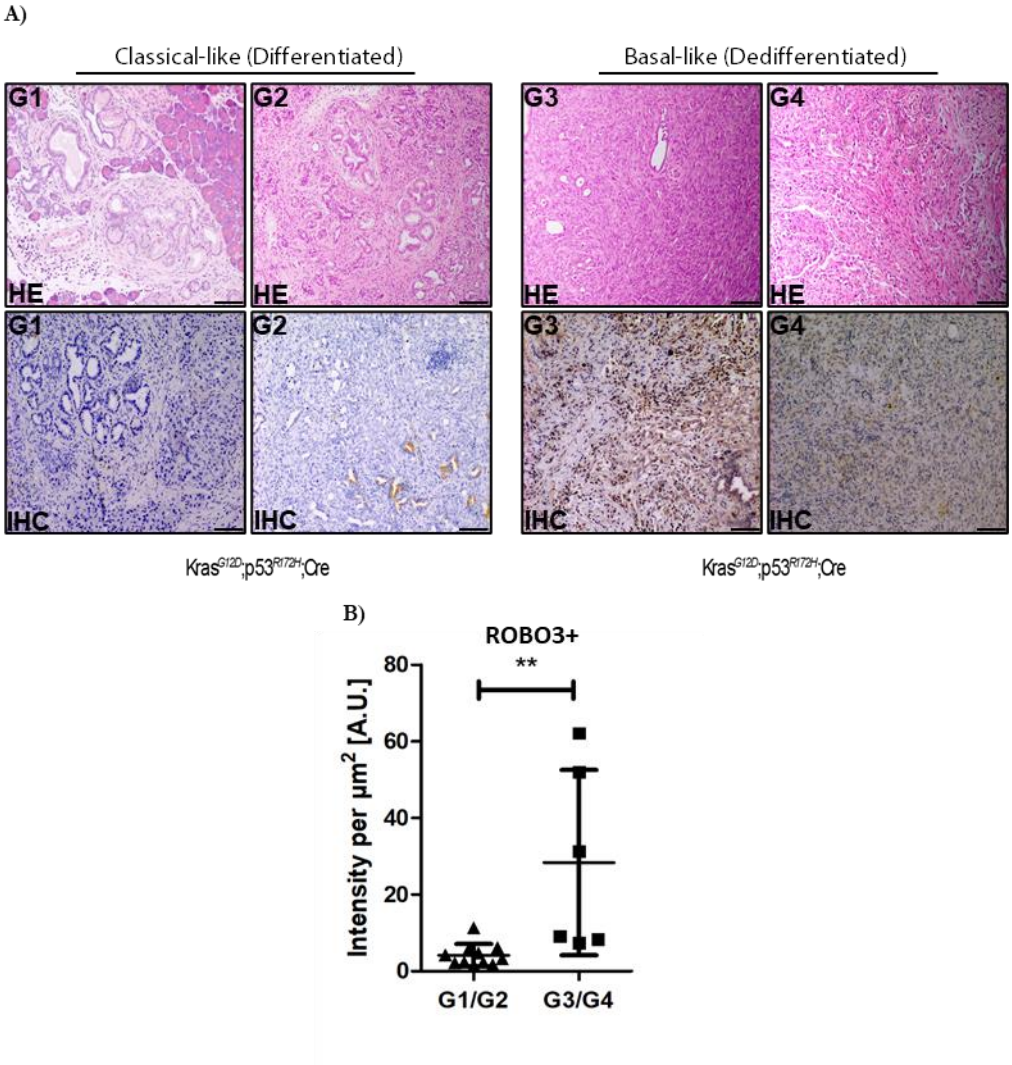

Figure 13. High grade KPC tumors show an increased ROBO3 expression. A) Representative H.E staining and IHC staining of ROBO3 in KPC tumors, grading of the tissue sections was performed by Prof. Ströbel, Department of Pathology, University Medicine Göttingen. Scale bar indicates 100 µm. B) Quantification of the ROBO3 intensity in IHC staining's. 20x field of view (F.o.V.), given as arbitrary units (A.U.). The measurement of the staining intensity was evaluated using ImageJ Fiji. Asterisks indicate significant changes as determined by Mann-Whitney test. G1/G2, n=11; G3/G4, n=6. P-Value = 0.0043

For further mechanistic and functional studies, we suppressed ROBO3 expression in pancreatic cancer cells by CRISPR-dCas9 technology. Successfully transfected cells could be detected by the EGFP signal of the dCas9 vector. We generated four knockdown clones (e.g. dCas9-ROBO3). For further experiments the clone dCas9-ROBO3 #4 was used as well as a LacZ expressing clone as control (Figure 14 B). Furthermore, we tested the expression of ROBO3 and the vector-based lineage marker EGFP by Immunofluorescence. Finally, co-

expression of ROBO3 and the lineage-specific marker EGFP enabled transfected cells to be detected in the corresponding basal-like cell line (Figure 14 C).

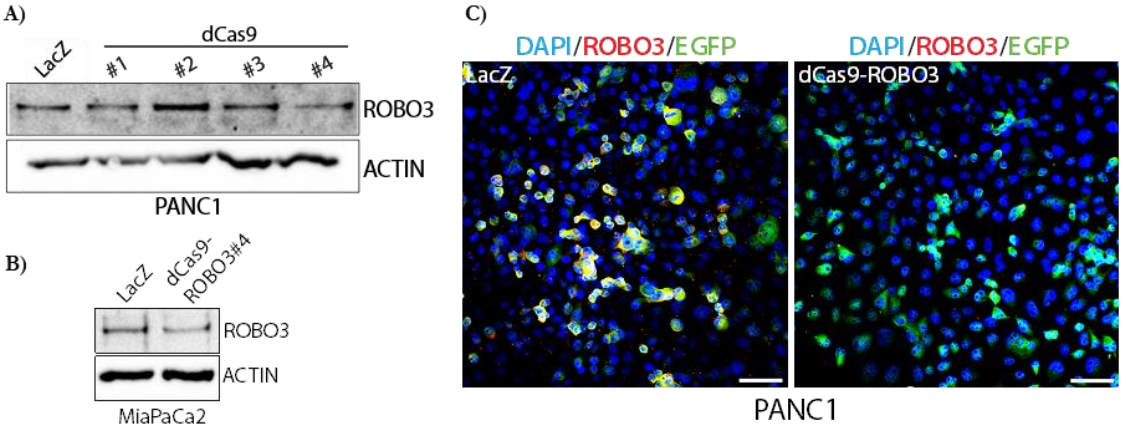

Figure 14. CRISPR/dCas9-mediated knockdown of ROBO3 in basal-like pancreatic cancer cells. A) and B) Immunoblot analysis of PANC1 and MiaPaCa2 (Basal-like subtype) CRISPR-dCas9 ROBO3 knockdown and control cells. C) Representative immunofluorescence staining for ROBO3 and EGFP in PANC1 LacZ and dCas9-ROBO3 cells. Scale bar 100 μM.

3.2 Correlation between ROBO3 signaling and cMet

Previous studies reported a functional link between ROBO3 and C-MET signaling in pancreatic cancer (Biankin et al. 2012). ROBO/SLIT signaling has been shown to downregulate MET signaling activity via the Rho GTPase CDC42, suggesting that loss of ROBO1/2 signaling activity promotes MET signaling downstream, which may represent a potential therapeutic target, as shown in Figure 7 (Biankin et al. 2012; Stella et al. 2009). Therefore, we tested whether ROBO3 silencing affects C-MET and CDC42 expression levels in pancreatic cancer cells with a basal-like phenotype. However, upon depletion of ROBO3 no changes in C-MET neither CDC42 levels were detected, suggesting that this pathway is not directly regulated by ROBO3 (Figure 15 A, C). Interestingly, analysis of certain EMT markers show a reduction in their expression. For instance, we found a significant loss of Sox2 and Zeb1 expression following ROBO3 depletion in cells (Figure 15 B and D).

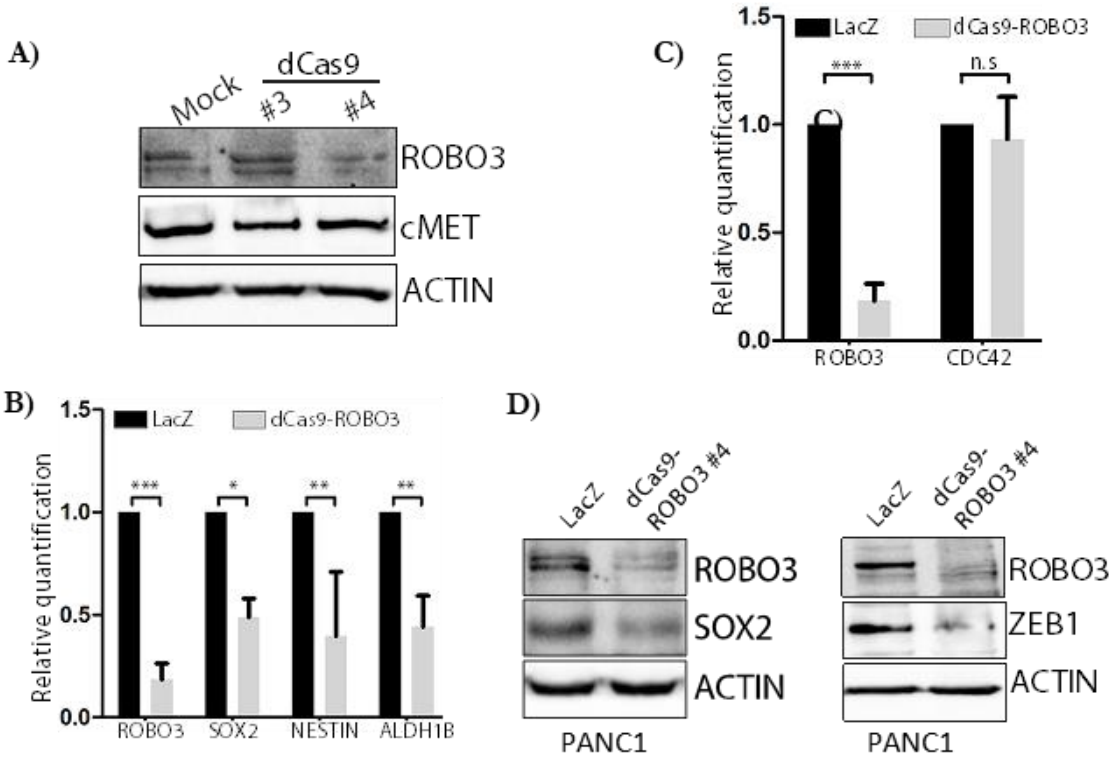

Figure 15. ROBO3 mediates EMT and stemness related gene signatures. A) and D) Immunoblot analysis using indicated antibodies following CRISPR-dCas9 mediated ROBO3 knockdown in PANC1 cells. n = 3. B) and C) RT-qPCR analysis of ROBO3, SOX2, Nestin, ALDH1B and CDC42 primer in PANC1. Results show average relative quantification (to control treatment) ± SD. Asterisks indicate significant changes to control treatment as determined by an unpaired Student's t-test. $P \leq 0.001$. n = 3.

3.3 ROBO3 promotes invasiveness and chemoresistence of basal-like PDA cells

In order to determine the functional consequences of a ROBO3 suppression in basal-like PDA cells, we performed proliferation studies as well as 3D-transwell invasion assays. In the comparison between untreated LacZ control cells and dCas9 ROBO3 silenced cells no significant difference in proliferation was observed, but downregulation of ROBO3 leads to a significant reduction of the invasive behavior compared to the LacZ control cells (Figure 16). Staining of invading cells confirmed the reduction of ROBO3 in our dCas9-ROBO3 cells, as well as the decreasing number of invading cells quantified by nuclear staining. Furthermore, we were also interested in ascertaining what effect the loss of ROBO3 causes on responsiveness to chemotherapy.

ROBO3 significantly modulates sensitivity to chemotherapy. In detail, depletion of the protein overcame resistance and rendered cells sensitive towards gemcitabine, even at low doses (Figure 16 B).

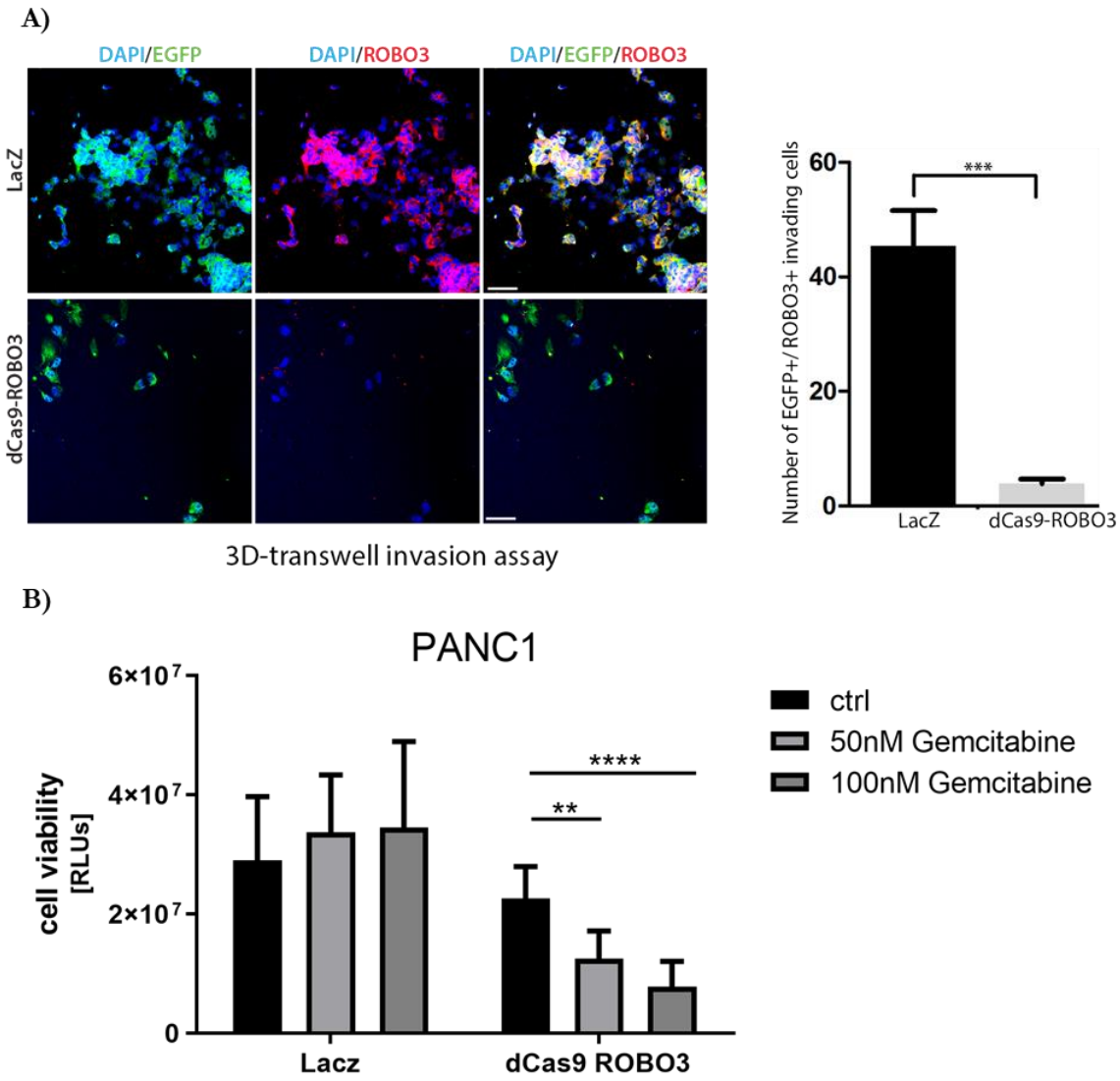

Figure 16. ROBO3 fosters invasion and mediates chemoresistance in basal-like subtype cells. Invasion Assay in LacZ control and dCas9 ROBO3 PANC1. After 48 hours incubation, the membranes were removed, the cells fixed and stained with DAPI, GFP and ROBO3. A) Representative fluorescence microscopy images for each condition. Quantification of tumor cell invasion, evidenced in 10x field of view (F.o.V.). B) Cell viability assay in ROBO3 CRISPR dCas9 depleted and LacZ control cells following treatment with Gemcitabine (2.000 cells for 72 hours). Measured in relative light units (RLUs). Scale bar 50 µM. Asterisks indicate changes to control, as determined by an unpaired Student's t-test. n = 2.

3.4 ROBO3 depletion affects basal-like cell gene signatures

In order to receive a more mechanistic insight into ROBO3 regulated gene signatures, we carried out RNA-Seq analysis in ROBO3 depleted and control PANC1 cells. For this purpose, we utilized three different sequences of ROBO3 for transient silencing and experimentally validated for better efficiency by qRT-PCR and western blot. As shown in Figure 17 A) and B), sequence number three has the most prominent effect on ROBO3 silencing on mRNA as well as on protein level, therefore we utilized this sequence for RNA-Seq analysis.

Displaying the plug-in principal component analysis (PCA), we could see a homogenous regulation within our treatment groups (Figure 17 C).

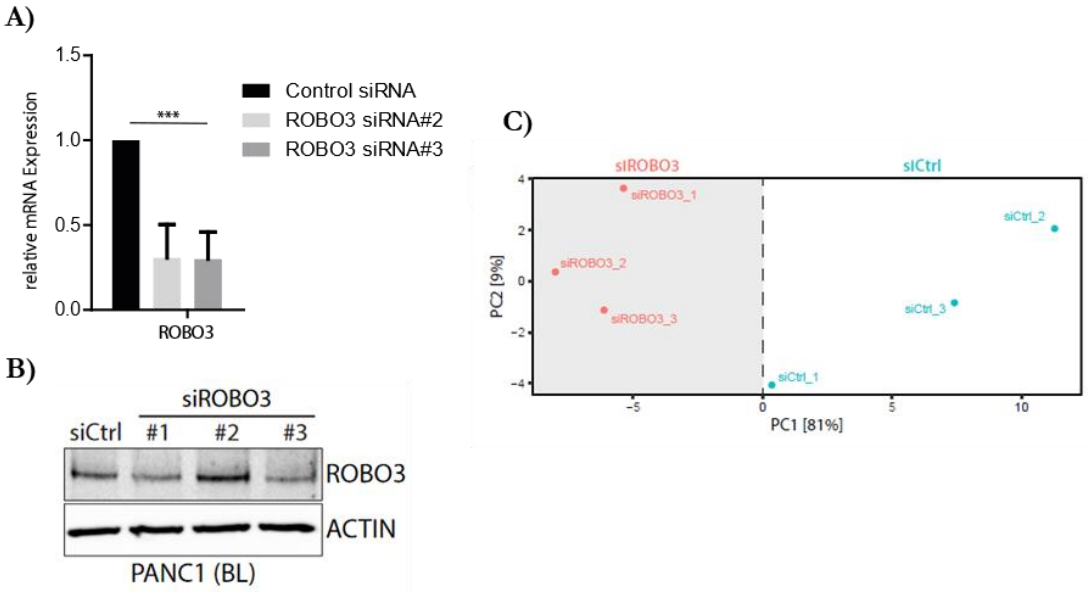

Figure 17. siRNA mediated ROBO3 knockdown for RNA-Seq analysis. A) Validation of ROBO3 silencing for RNA-Seq samples (three triplicates) via RT-qPCR analysis in PANC1 following siRNA mediated ROBO3 knockdown. Results show average relative quantification (to control treatment) ± SD. n = 3. B) Immunoblot analysis using indicated antibodies following ROBO3 silencing in PANC1 cells. n = 3. C) PCA plot of RNA-seq data performed on BL PANC1 cells transfected with siROBO3 or siCtrl. n =3.

Gene set enrichment analysis (GSEA) shows that numerous gene signatures associated with pancreatic cancer cell identity were significantly affected following ROBO3 silencing and also revealed a subtype-switch from basal-like to classical subtype in ROBO3 depleted cells. In particular, our findings showed that the hallmarks genes associated with EMT, mitotic spindle and apical junction, respectively assigned to the basal-like subtype, were significantly downregulated (Figure 18). Notably, this subtype switch was also emphasized by upregulation of genes involved in fatty acid metabolism and xenobiotic metabolism, which are attributed to the classical subtype (data not shown) (Gabitova-Cornell et al. 2020).

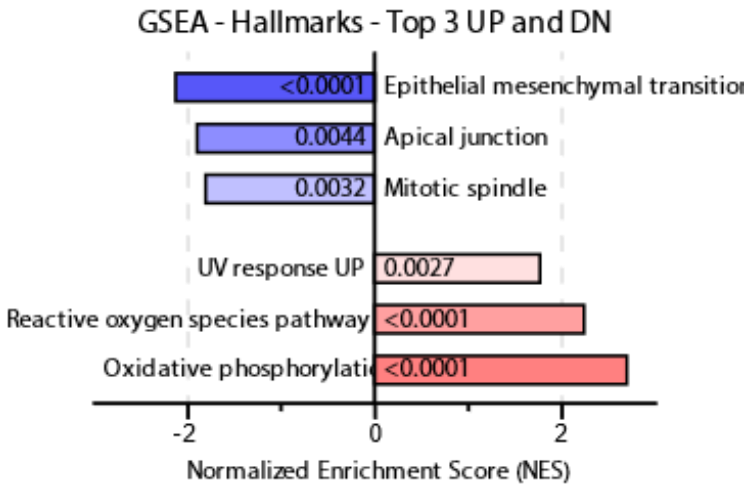

Figure 18. Transcriptional subtype switch upon ROBO3 silencing. The bar graph shows normalized enrichment values (NESs) of the gene set enrichment analysis (GSEA) on the top three upregulated and downregulated hallmark pathways for the ROBO3 knockdown RNA-Seq analyses. Significant gene sets (FDR < 0,05) are marked in red for upregulated genes and in blue for downregulated genes, respectively.

A selection of subtype-specific markers was compiled based on the published data of Collisson, Moffitt and Bailey. The regulation of those subtype markers under ROBO3 knockdown was visualized in the volcano blot. As Figure 19 A) illustrates, there is a distinct tendency for basal-like gene signatures to be downregulated after ROBO3 knockdown (e. g. ZEB1, AXL or KRT5), while some classical gene signatures are upregulated (e. g. AGR2). To validate ROBO3 mediated basal-like subtype specificity we performed qRT-PCR for selected basal-like and classical subtype related genes following ROBO3 silencing. All three replicates showed a significant siRNA mediated knockdown of ROBO3 in PANC1 cells and demonstrate that AGR2, ERBB2 and CAPN8 as markers of classical lineage differentiation are (approx. 2-fold) upregulated upon ROBO3 silencing, whereas basal-like gene signatures, e.g. AXL, TNC and SLC39A13 are significantly downregulated (Figure 19 B).

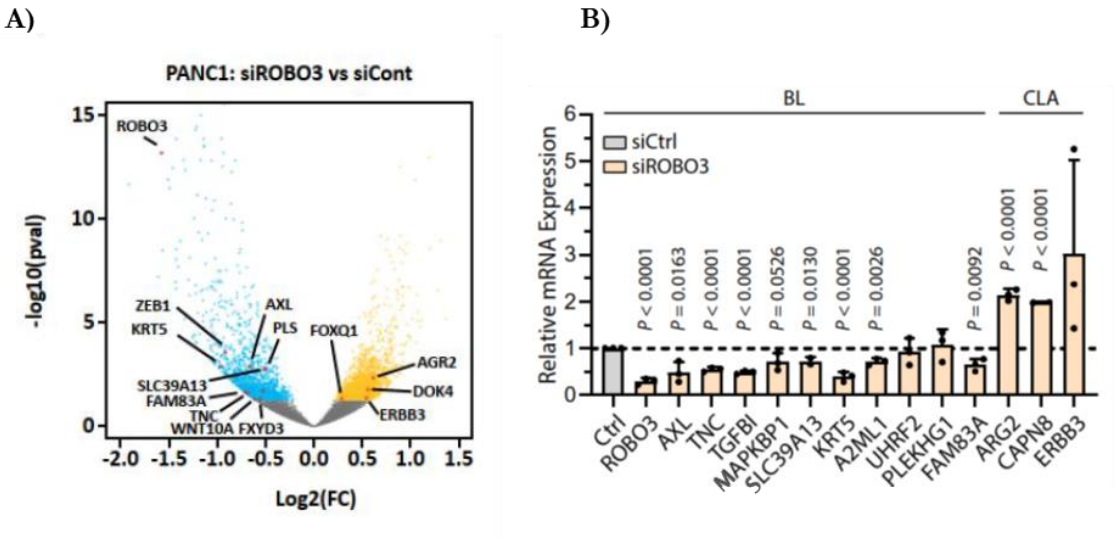

Figure 19. Volcano plot and evaluation of RNA-Seq results. A) Volcano plot shows indicated up- and down regulated genes from RNA-Seq. B) Verification of RNA-Seq results via RT-qPCR analysis of selected basal-like and classical defined primer, based on the published data of Collisson, Moffitt and Bailey, in PANC1. Results show average relative quantification (to control treatment) ± SD. n = 3.

Next, we examined potential major gene signatures involved in ROBO3 mediated PDA invasiveness. Our GSEA analysis revealed STAT3_target genes and invasiveness signatures were significantly affected following ROBO3 depletion in PANC1 cells (Figure 20).

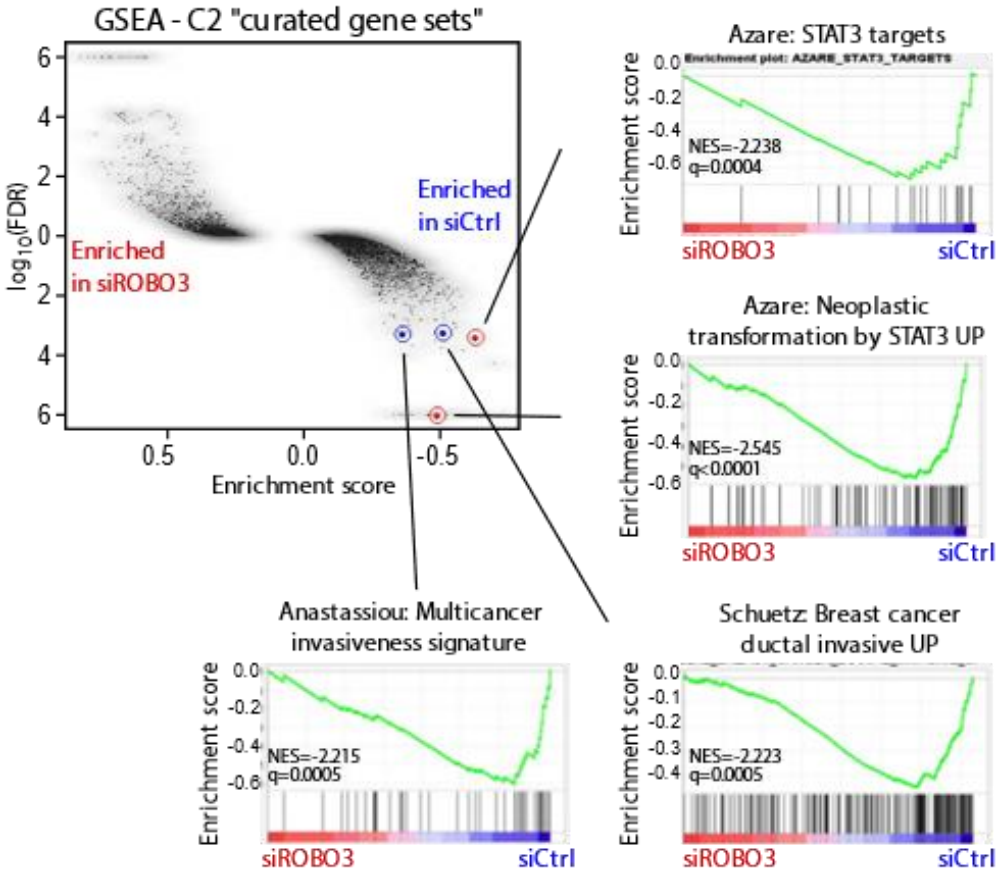

Figure 20. Major hallmark gene sets following ROBO3 knockdown in RNA-Seq. Gene set enrichment analysis (GSEA) on the selected hallmark gene sets for the ROBO3 knockdown RNA-seq analyses. The alteration of different hallmark gen sets based on the enrichment score (ES) is plotted logarithmically. The most significant individual hallmarks are highlighted. Significance is indicated by FDR q (FDR q < 0.05), enrichment scores (ES), and normalized enrichment scores (NES) marked in each graph.

3.5 ROBO3 regulates pSTAT3 activity in PDA cell lines

To address the molecular mechanism of ROBO3 signaling pathway, we focused on the IL-6/STAT3 pathway, which was significantly downregulated under ROBO3 knock-down in our RNA-Seq analysis (Figure 21) Immunoblot analysis revealed that pSTAT3 is highly expressed in basal-like phenotype, especially in MiaPaCa2, whereas classical-like cells such as CAPAN1 and L3.6 display very low levels (Figure 21 A). Accordingly, IF analysis showed the highest pSTAT3 levels in MiaPaca2 cells (Figure 21 B). Figure 21 C) and D) show the effect of ROBO3 dCas9 mediated knockdown on pSTAT3 (tyrosine 705) expression in MiaPaCa2 and PANC1. Reduction of pSTAT3 in ROBO3 depleted PANC1 cells is accompanied with silencing of Sox2 and Wnt10a, which are both associated with dedifferentiated,

basal-like tumors. The transcription factor Sox2 is a key regulator of pluripotency during mammalian development and is involved in tumorigenesis of pancreatic cancer (Cox et al. 2012; Leis et al. 2012). In particular, Sox2 maintains the self-renewal of undifferentiated embryonic stem cells and through its ability to regulate gene regulation, promotes tumorigenesis in various epithelial tumors, including pancreatic cancer (Herreros-Villanueva et al. 2013; Sarkar and Hochedlinger 2013; Singh et al. 2015). Current studies indicate that self-renewing cancer stem cells (CSCs) contribute to the dissemination of metastases and therapeutic failure. Seino et al. demonstrated that epithelial Wnt ligand expression including Wnt10a is associated with clinical progression and reduced overall survival of PDAs (Seino et al. 2018). To determine whether STAT3 controls ROBO3, a siRNA mediated knockout of STAT3 was performed and evaluated by immunoblot. However, the ROBO3 expression remained unaffected by STAT3 silencing. Therefore, our results did not support the hypothesis that STAT3 is an upstream regulator of ROBO3 in PDA (Figure 21 E).

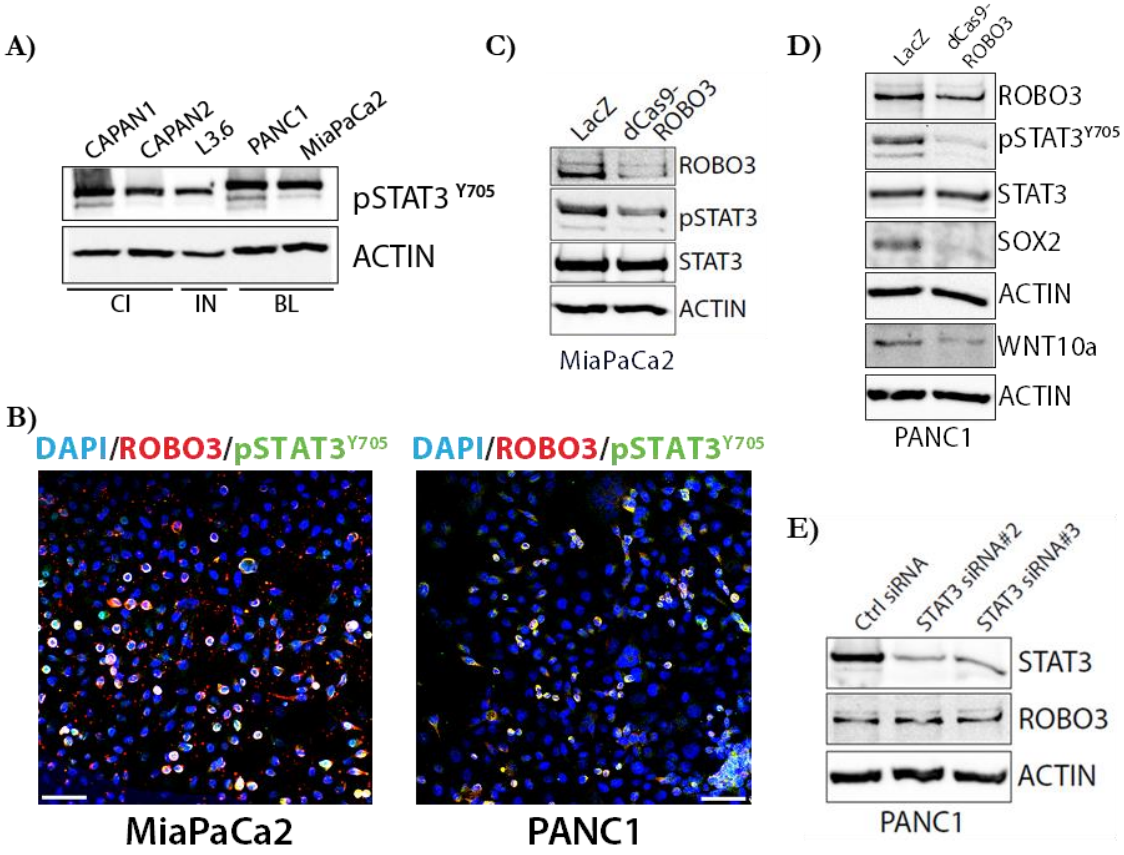

Figure 21. ROBO3 controls phosphorylation of STAT3 in Pancreatic cancer. A) Immunoblot analysis of classical (Cl): Capan1 and Capan2, intermediate (IN): L3.6 and basal-like(BL): PANC1, MiaPaCa2 cell lines using indicated antibodies. B) Representative immunofluorescence staining for ROBO3 and pSTAT3 (Tyr 705) in MiaPaCa2 and PANC1 cells. Scale bar indicates 100 µM. C) and D) Immunoblot analysis of LacZ ctrl and dCas9 ROBO3 depleted MiaPaCa2 and PANC1 cells using indicated antibodies. E) Immunoblot analysis of STAT3 siRNA mediated silenced PANC1 cells using indicated antibodies.

In order to study the role of ROBO3 signaling on STAT3 regulation, we carried out CRISPR dCas9 mediated ROBO3 overexpression in classical PDA and assessed the resulting effects on pSTAT3 levels. Indeed, we observed increasing pSTAT3 levels in both classical cell lines after ROBO3 overexpression, which underlines the relationship of ROBO3-dependent regulation of STAT3 phosphorylation (Figure 22 A). While only CAPAN2 shows a slight increase of Wnt10a, CAPAN1 shows no change. In addition, we also performed immunofluorescence staining and could confirm that the phosphorylation of STAT3 in dCas9 ROBO3 silenced cells is significantly lower than in Lacz control cells (Figure 22 B).

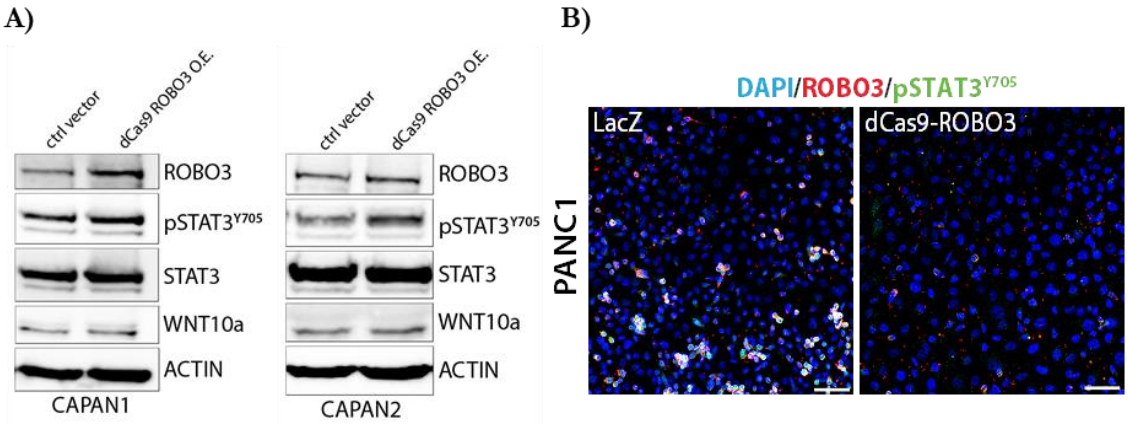

Figure 22. ROBO3 dependent pSTAT3 activation in PDA. A) Immunoblot analysis of dCas9 mediated ROBO3 overexpression (O.E.) in CAPAN1 and CAPAN2 (CL) cells using indicated antibodies. The STAT3 antibody was probed after stripping pSTAT3 membrane. B) Representative immunofluorescence staining for ROBO3 and pSTAT3 (Tyr 705) in LacZ control and dCas9 ROBO3 PANC1 cells. Scale bar 100 µM.

3.6 ROBO3 mediated pSTAT3 activity in both PDX-derived cell lines and KPC tumors

In order further elaborate on this novel pathway, we used Patient-derived Xenograft (PDX) models (generation described in Figure 9). Thereby, we could show that ROBO3 levels correlate at least in part with those of pSTAT3 and WNT10a in PDX cell lines, especially in GCDX-57. ROBO3 knockdown in the GCDX-5 cells (classified as "ROBO3 high") reduced the expression levels of the downstream targets pSTAT3 and WNT10a (Figure 23 B).

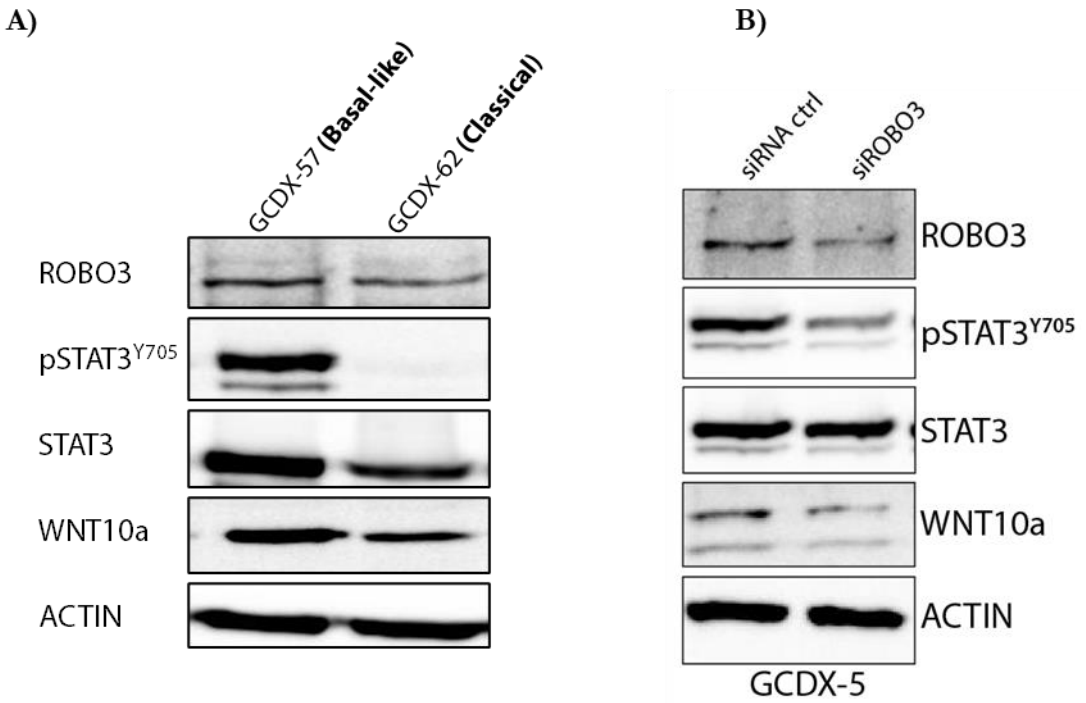

Figure 23 ROBO3 depletion in Patient-derived Xenografts confirms mechanism *in vitro*. A) Immunoblot analysis of CDX-62, GCDX-57 and GCDX-62 patient-derived cell lines using indicated antibodies. B) Immunoblot analysis of GCDX-5 siRNA mediated ROBO3 depleted cells using indicated antibodies. The STAT3 antibody was probed after stripping pSTAT3 membrane.

To validate our data from the functional invasion assays we carried out ROBO3 knockdown experiments using the PDX cell lines GCDX-5 and GCDX-57, which were categorized as ROBO3 high (Figure 24 and Figure 25). In order to test whether sufficient silencing was achieved, the same cells were used to verify the ROBO3 knockdown using immunoblot analysis (Figure 24 and Figure 25 C). In these cell lines we observed a significant reduction of invasive capacity, by significantly fewer cells migrating after ROBO3 knockdown.

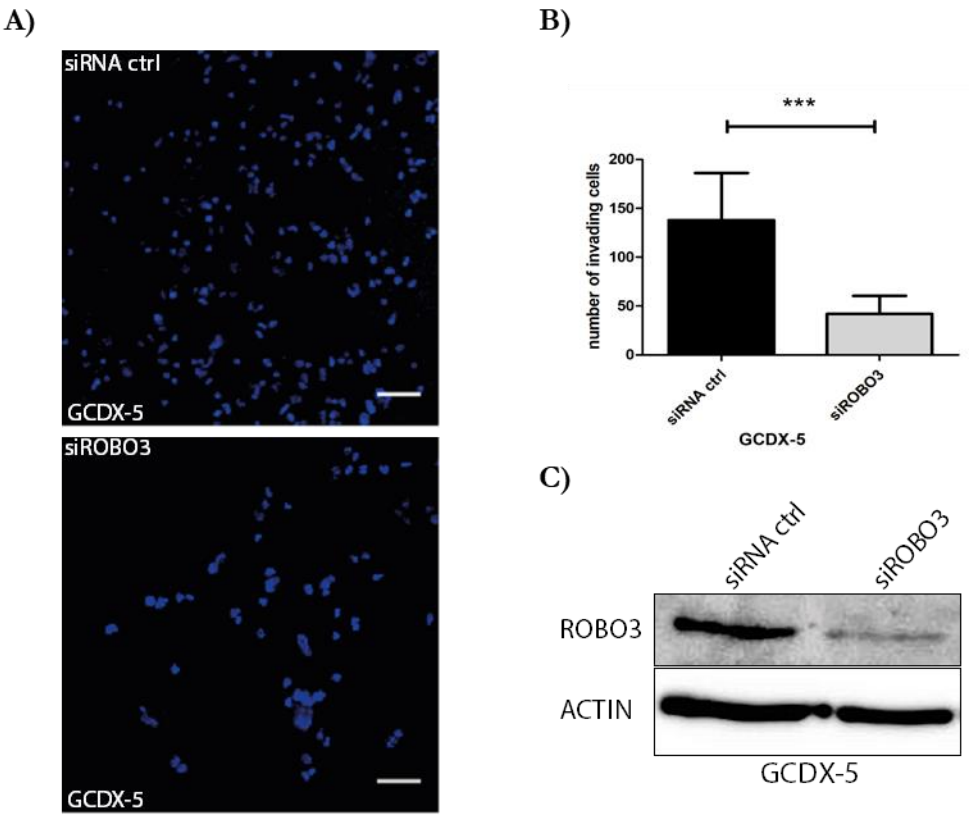

Figure 24. SiRNA mediated ROBO3 silencing in GCDX-5 patient-derived Xenograft results in reduced invasive capacity. Invasion assay of GCDX-5 siRNA control and siRNA ROBO3 silenced cells. A) Representative fluorescence microscopy images for each condition. Scale bar 50 μm. B) Bar graph of quantification, given as invading DAPI positive per 20x field of view (F.o.V.). $P \leq 0.001$. $n = 2$. C) Immunoblot analysis of each condition using indicated antibodies was performed to control silencing.

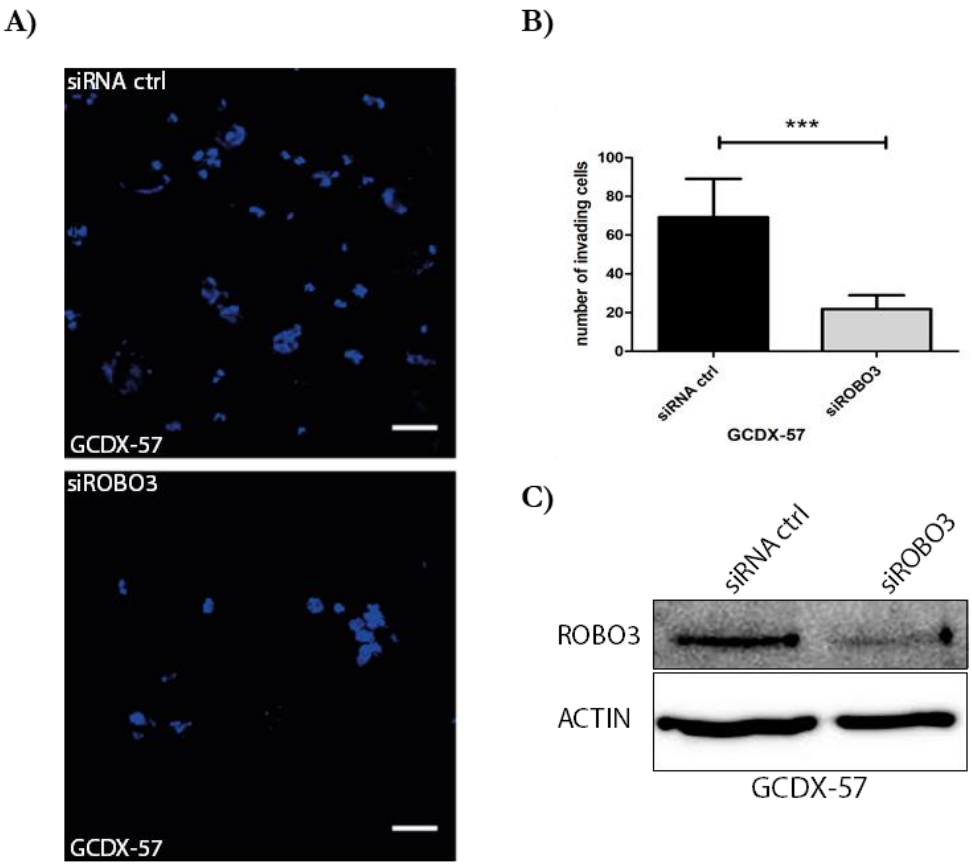

Figure 25. SiRNA mediated ROBO3 silencing in GCDX-57 patient-derived Xenograft results in reduced invasive capacity. Invasion assay of GCDX-57 siRNA control and siRNA ROBO3 silenced cells. A) Representative fluorescence microscopy images for each condition. Scale bar 50 μm. B) Bar graph quantification, given as invading DAPI positive per 20x field of view (F.o.V.). $P \leq 0.001$. $n = 2$. C) Immunoblot analysis of each condition using indicated antibodies was performed to control silencing.

3.7 ROBO3 regulates the tyrosine kinase AXL to maintain STAT3 activity in PDA

To further dissect the ROBO3 mediated phosphorylation of STAT3, we specifically searched our RNA-seq analysis data for downregulated tyrosine kinases. This approach attracted our attention to the receptor tyrosine kinase AXL (Figure 19). AXL belongs to the subfamily of TAM (Ty-ro3, AXL, MerTK), and its high expression is associated with tumor aggressiveness, drug-resistant and metastatic phenotype in variety of malignant tumor types (Gjerdrum et al. 2010; Wu et al. 2014; Rankin and Giaccia 2016; Cruz et al. 2019). In order to test for a correlation between AXL and ROBO3, we investigated the mRNA expression from AXL after siRNA-mediated knockdown of ROBO3 by qRT-PCR and revealed a decreased expression as indicated in Figure 19 B). In PDA, a high expression of AXL is associated with a poor prognosis and is considered as a marker for the basal-like subtype (Ludwig et al. 2018). Therefore, we determined the AXL expression via immunoblot analysis in our basal-like

representing cell lines MiaPaCa2 and PANC1 compared to the classical cell line CAPAN1. We found strong differences in the expression levels as hence, we found very low AXL expression in CAPAN1 cells and high levels of the kinase in PANC1 and MiaPACA2 cells (Figure 26 A). Furthermore, we analyzed the effect of ROBO3 knockdown on AXL expression. In line with our model of a ROBO3 regulated pathway, we observed AXL downregulation upon siRNA mediated knockdown of ROBO3, both in both PANC1 and MiaPaCa2 cell lines as well as in the ROBO3-high classified PDX cell line GCDX-57 (Figure 26 B-D).

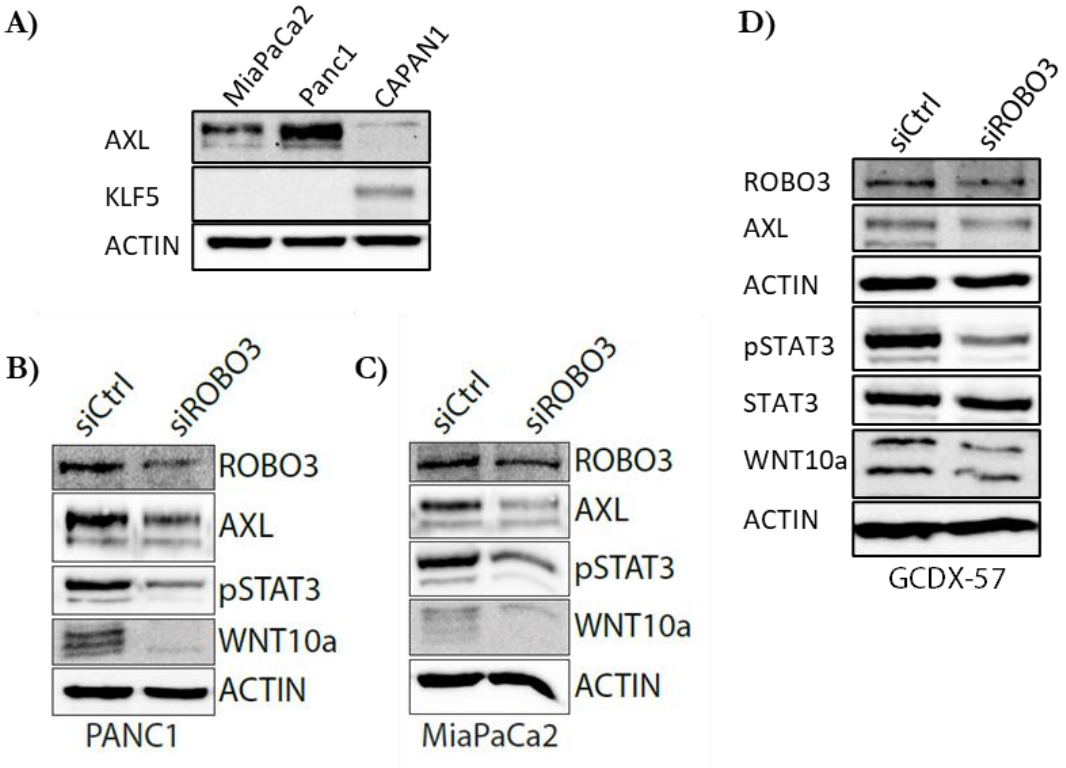

Figure 26. ROBO3 governs tyrosine kinase AXL to control pSTAT3 levels in Basal-like subtype. A) Immunoblot analysis of MiaPaCa2, PANC1 and CAPAN1 using indicated antibodies. B) and C) Immunoblot analysis of PANC1 and MiaPaCa2 following siRNA mediated ROBO3 silencing was performed using indicated antibodies. D) Immunoblot analysis of PDX cell line GCDX-57 following siRNA mediated ROBO3 silencing was performed using indicated antibodies. The STAT3 antibody was probed after stripping pSTAT3 membrane.

However, another important question was whether the tyrosine kinase AXL actually influences the phosphorylation of STAT3 and other downstream targets of ROBO3 such as Wnt10a in PDA. To address this question, we used a siRNA mediated knockdown of AXL and could show that pSTAT3 levels are significantly reduced following AXL knockdown (Figure 27). In addition, no alterations of ROBO3 levels were observed, supporting the hypothesis that ROBO3 is an upstream regulator of AXL in this signaling loop (Figure 27).

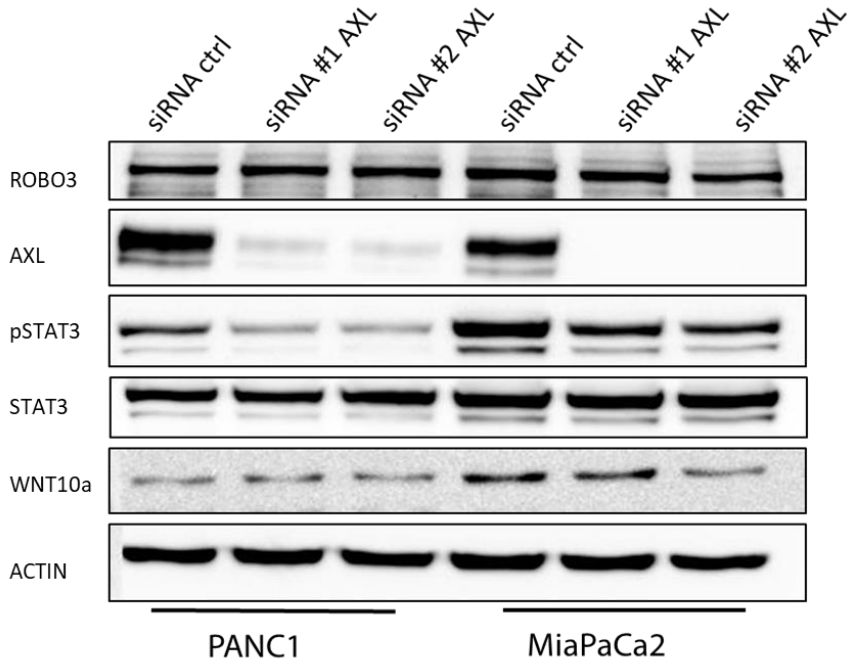

Figure 27. Tyrosine kinase AXL regulates pSTAT3 in basal-like PDA phenotype.Immunoblot analysis of PANC1 and MiaPaCa2 following siRNA mediated AXL silencing using indicated antibodies was performed (n=2). The STAT3 antibody was probed after stripping pSTAT3 membrane.

3.8 AXL depletion leads to reduced invasion in basal-like PDA cells

Based on the observed effects of AXL on the phosphorylation of STAT3, we wanted to determine if these changes also result in functional consequences in the invasion assay. Therefore, we performed an invasion assay following siRNA mediated AXL knockdown in basal-like cell lines and tested pSTAT3 levels by immunoblot analysis. We observed a significant reduction in invasiveness of the basal-like subtype representing cells MiaPaCa2 and PANC1, accompanied by a significant reduction of the pSTAT3 levels (Figure 28).

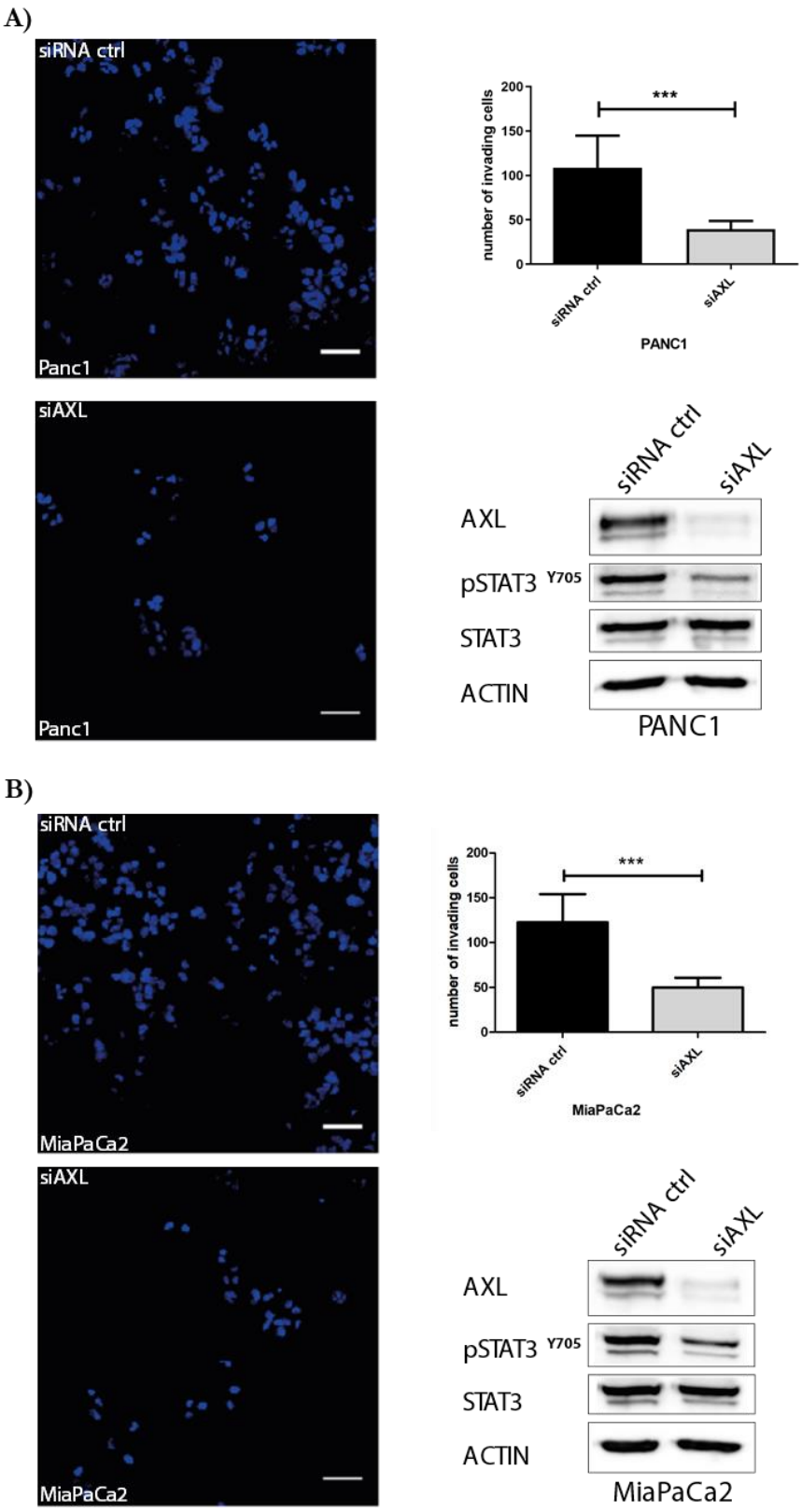

Figure 28. siRNA mediated AXL silencing in MiaPaCa2 and PANC1 results in reduced invasive capacity and reduced pSTAT3 expression. Invasion assay of PANC1 (A) and MiaPaca2 (B) following siRNA mediated AXL (#2) silencing. Representative fluorescence microscopy images for each condition. Scale bar 50 μm. Bar graph of quantification, given as invading DAPI positive per 20x field of view (F.o.V.). P=≤ 0.001. n = 2. Immunoblot analysis of each condition using indicated antibodies was performed to control silencing. The STAT3 antibody was probed after stripping pSTAT3 membrane.

3.9 ROBO3 mediated IL-6/pSTAT3 signaling axis in PDA cells

The STAT3 pathway is linked to the inflammatory cytokine interleukin 6 (IL-6). To investigate potential interactions between IL-6 and the expression of basal-like gene signatures such as ROBO3 in pancreatic tumor cells, we treated cells with IL-6. Treatment with the cytokine induced an increase of pSTAT3 expression in PDA cells (Figure 29 A and B). The strongest increase of pSTAT3 was observed after 48 hours treatment, while the total STAT3 levels remain constant (Figure 29 A). Interestingly, ROBO3 expression increased following IL-6 treatment in almost all PDA cell lines (Figure 29 A). In particular, ROBO3 expression was markedly high in classical cell lines such as CAPAN1 or intermediate classified L3.6 cells following IL-6 treatment. Furthermore, IF staining showed that ROBO3 and pSTAT3 substantially co-localize within the same cells following IL-6 treatment (Figure 29 B).

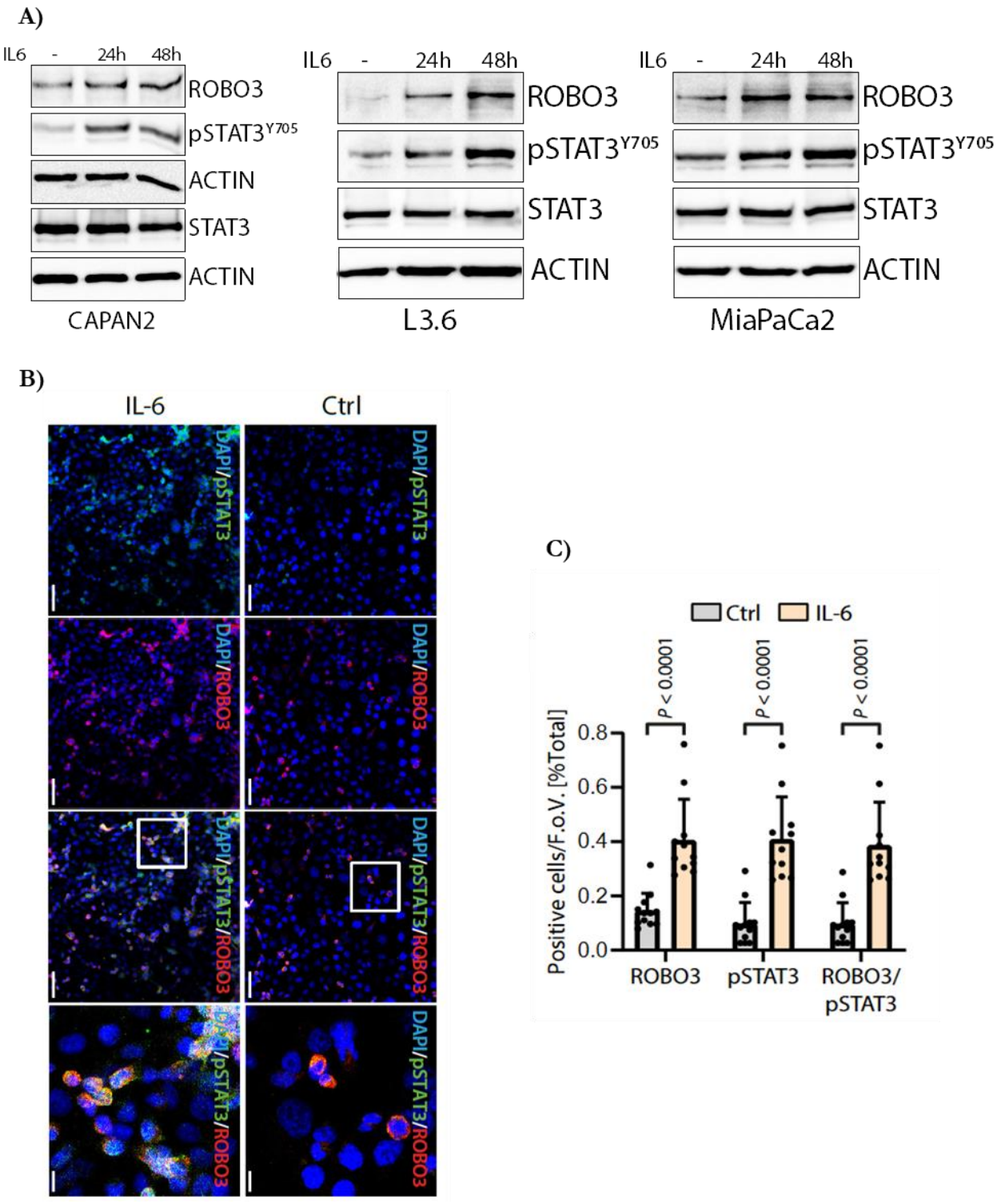

Figure 29. IL-6 induces ROBO3 expression in PDA cells. A) Immunoblot analysis of CAPAN2, L3.6 and MiaPaCa2 cells were performed following treatment with 50 ng/ml IL-6 for 24 hours and 48 hours using indicated antibodies. The STAT3 antibody was probed after stripping pSTAT3 membrane. B) Representative immunofluorescence images of PANC1 cells following treatment with 50 ng/ml IL-6 for 48 hours and subsequently stained for ROBO3 and pSTAT3 (Tyr 705). Scale bar 50 µm. C) Bar graph of quantification, given as ROBO3, pSTAT3 and ROBO3/pSTAT3 positive cells per 20x field of view (F.o.V.). n = 2. Statistical significance was determined by Mann-Whitney test.

In addition, IL-6 treatment was performed in co-staining with ROBO3 and IL-6 antibodies in PANC1 cells. The statistical evaluation clearly shows an induction of ROBO3 after treatment (Figure 30 A). The number of IL-6 positive cells also increased significantly, which can be considered a control for adequate treatment. Immunofluorescence staining for ROBO3 together with IL-6 was performed to evaluate whether ROBO3 knockdown also influences IL-6 expression (Figure 30 B). Figure 30 B) illustrates that no difference in IL-6 expression could be observed after ROBO3 depletion.

As previously mentioned, our study has revealed that exposure to the inflammatory cytokine IL-6 leads to induction of ROBO3 and pSTAT3 expression in various molecular subtypes of pancreatic cancer and can consequently alter tumor transcription. To get an indication of the mechanism underlying this particular network, a so-called rescue experiment was performed by treating both wildtype LacZ control cells and dCas9 ROBO3 silenced PANC1 with interleukin 6 (Figure 30 C). As in normal control lysates of different PDA subtypes, treatment with IL-6 in LacZ control cells results in an increase of the ROBO3 and pSTAT3 levels, with a maximum of 48 hours. Total STAT3 levels remaining the same. In untreated dCas9 ROBO3 clones, a reduction of ROBO3 can be seen compared to LacZ control cells. However, a reduction of pSTAT3 in this immunoblot is not as evident as other experiments show. Nevertheless, this immunoblot allows to illustrate that the relative increase of pSTAT3 after treatment with IL-6 in the dCAs9 ROBO3 PANC1 clones is significantly reduced compared to the LacZ control PANC1 cells.

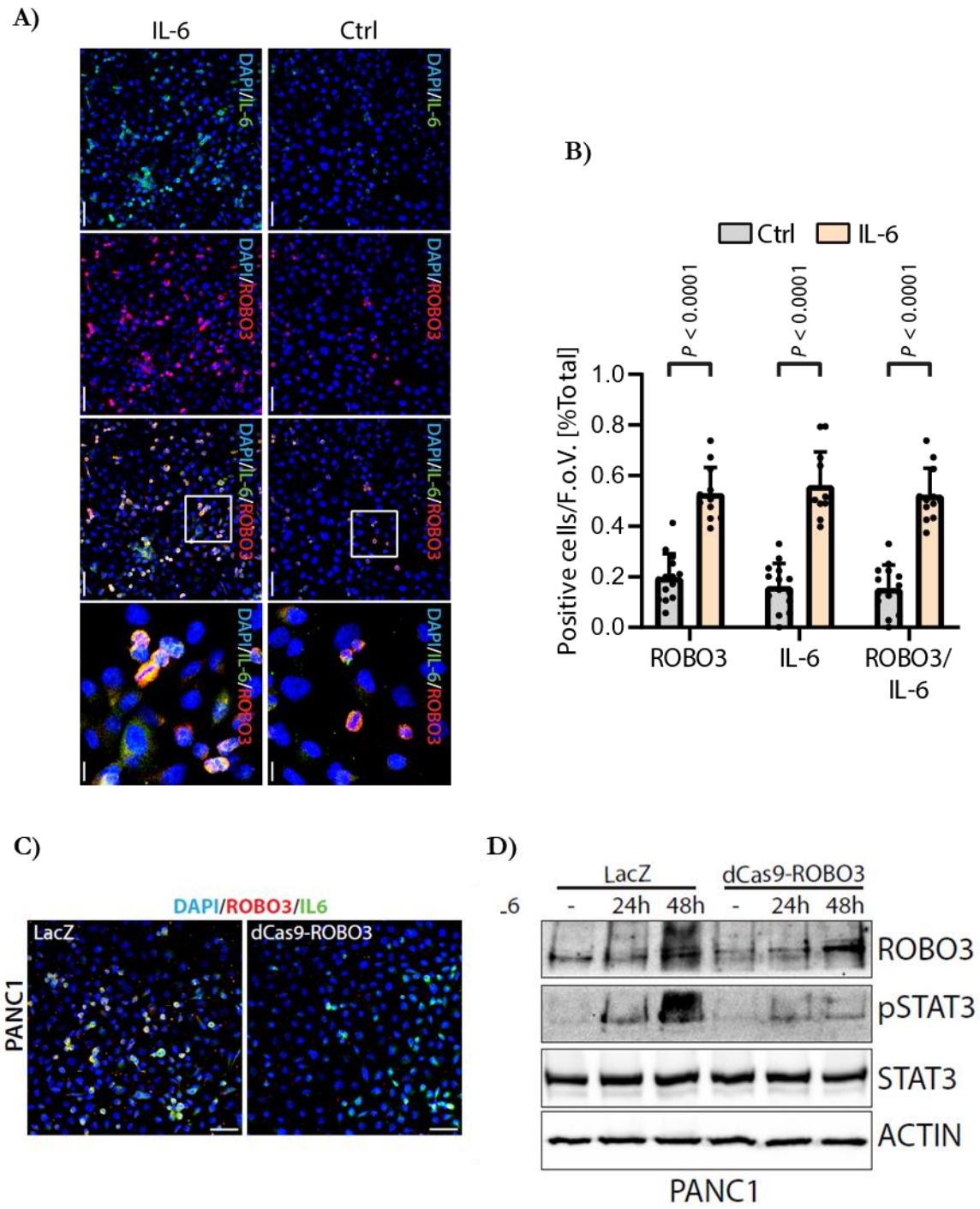

Figure 30. Linkage between IL-6 and ROBO3. A) Representative immunofluorescence images of PANC1 cells following treatment with 50 ng/ml IL-6 for 48 hours and subsequently stained for ROBO3 and IL-6. Scale bar 50 µm. B) Bar graph of quantification, given as ROBO3, IL-6 and ROBO3/IL-6 positive cells per 20x field of view (F.o.V.). n = 2. Statistical significance was determined by Mann-Whitney test.. C) Representative immunofluorescence images of LacZ control and dCas9 ROBO3 PANC1 cells stained for ROBO3 and IL-6. Scale bar 50 µm. D) Immunoblot analysis of LacZ and dCas9 ROBO3 depleted PANC1 cells following IL-6 treatment (50 ng/mL) for 48 hours using indicated antibodies was performed. The STAT3 antibody was probed after stripping pSTAT3 membrane.

3.10 Disruption of IL-6 mediated AXL induction following ROBO3 silencing in PDA

To validate these findings, the same experimental design was additionally executed with a siRNA mediated knockdown of ROBO3. In contrast to the dCas9 ROBO3 clones, siRNA mediated knockdown can detect a significant downregulation of pSTAT3 in the untreated samples after ROBO3 depletion (Figure 31). In both MiaPaCa2 and PANC1, which represent the basal-like subtype, pSTAT3 values in the silenced samples after the ROBO3 knockdown do not show the expression increase as in the control samples after IL-6 treatment (Figure 31). Additionally, we tested our signal axis with AXL and, interestingly, two important observations could be obtained. On the one hand, AXL expression is induced by IL-6 treatment and on the other hand AXL is also suppressed after ROBO3 knockdown and does not respond to IL-6 treatment with an increased expression following ROBO3 knockdown. Wnt10a is down-regulated in ROBO3 siRNA knockdown samples, however, shows no change after IL-6 treatment. The findings were obtained in both basal-like representing cell lines PANC1 and MiaPaCa2 (Figure 31).

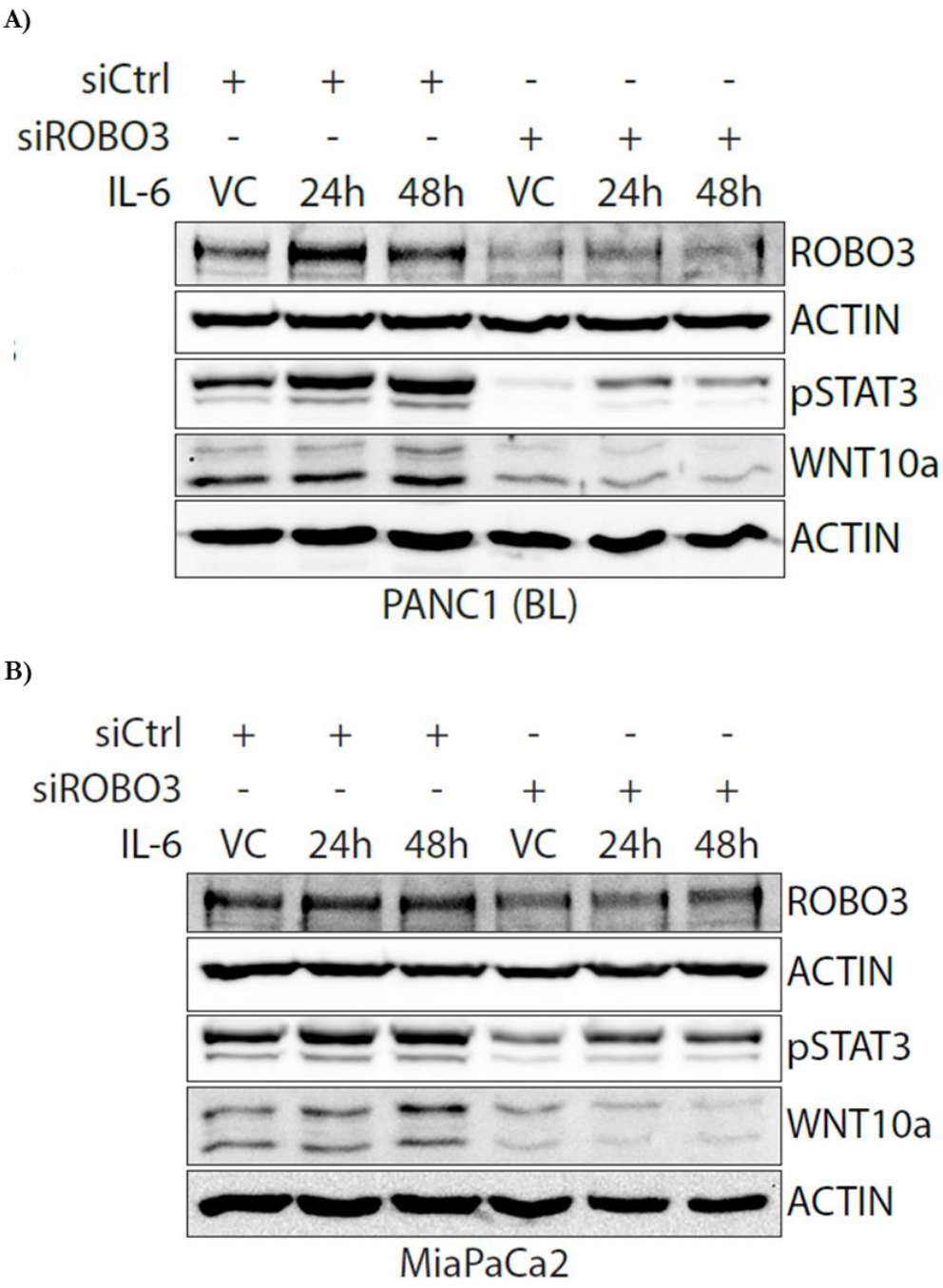

Figure 31. ROBO3 dependent pSTAT3 regulation in context of IL-6. A) and B) Immunoblot analysis of MiaPaCa2 and PANC1 cells following combined siRNA mediated ROBO3 silencing and IL-6 treatment (50 ng/mL) for 24 and 48 hours was performed with indicated antibodies.

3.11 IL-6 mediated STAT3 activity is independent of AXL status

We used the same experimental design with AXL knockdown in order to determine if this kinase, as a downstream target of ROBO3, is also able to decouple the phosphorylation of pSTAT3 under IL-6 treatment. As the immunoblot analysis shows, a sufficient AXL knockdown was achieved with both different siRNAs (#1 and #2). However, the treatment with IL-6 in this approach was limited to 24h, so that in contrast to an IL-6 treatment over 48h, no significant expression increase of AXL can be detected (Figure 32). The knockdown of AXL is maintained under IL-6 treatment, only in PANC1 #2 siAXL a slight induction of AXL under IL-6 treatment can be detected. The silencing of AXL leads to a downregulation of pSTAT3 in the untreated siRNA AXL samples compared to the control. Interestingly, the AXL knockdown does not suppress or attenuate phosphorylation of STAT3 after IL-6 treatment in contrast to a ROBO3 knockdown. ROBO3 shows a slight induction in the controls after IL-6 treatment, which is in accordance with the previous results. However, under AXL knockdown no constant and significant changes can be seen, which is also applicable for Wnt10a (Figure 32). These observations are consistent for both basal-like representing cell lines MiaPaCa2 and PANC1.

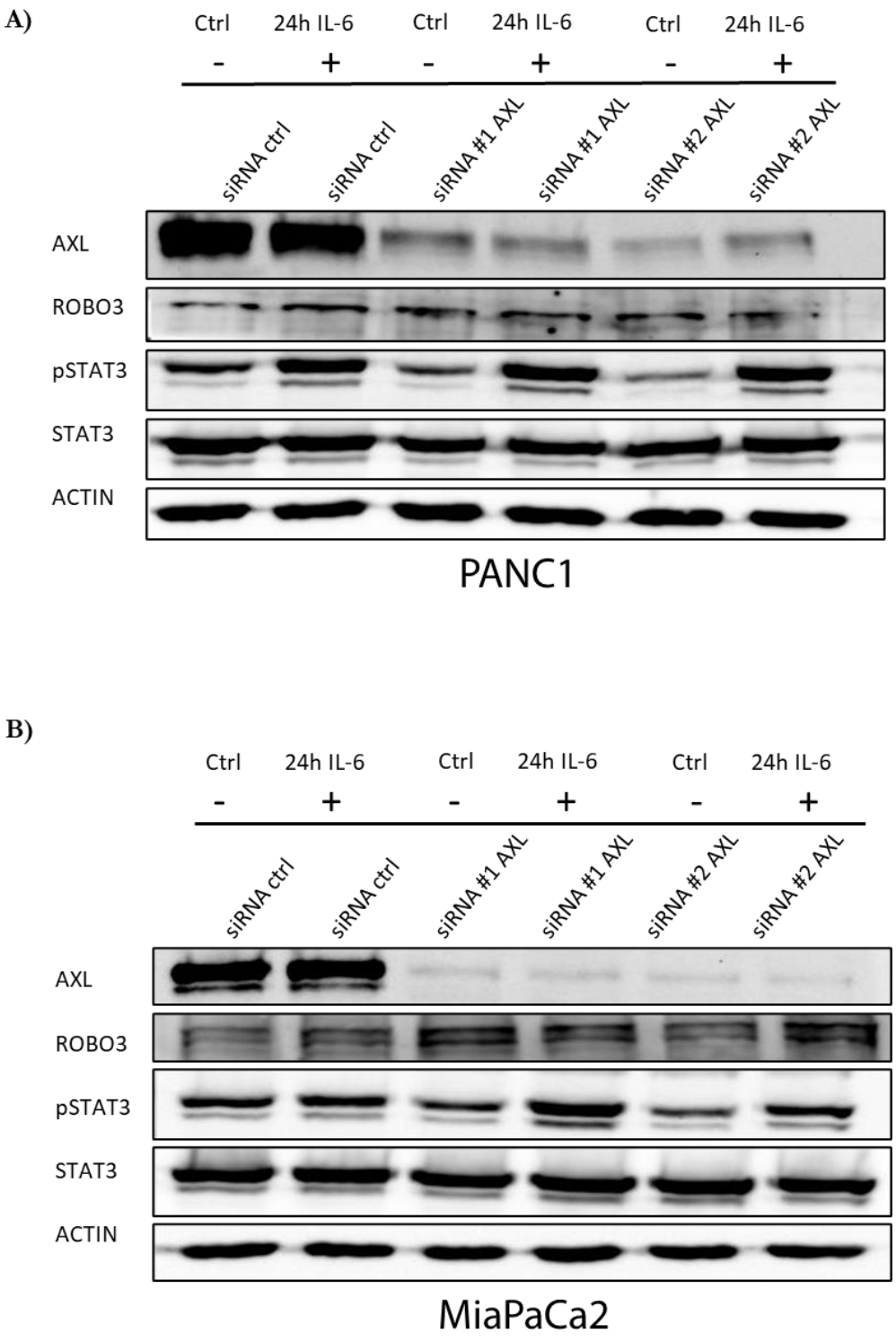

Figure 32. AXL knockdown does not affect the IL-6 pSTAT3 axis in PDA. A) and B) Immunoblot analysis of PANC1 and MiaPaca2 cells following combined siRNA mediated AXL (#2) silencing and IL-6 treatment (50 ng/mL) for 24 hours was performed with indicated antibodies. The STAT3 antibody was probed after stripping pSTAT3 membrane.

3.12 ROBO3-deficiency reduces metastatic burden in an orthotopic PDA model

In order to analyze the functional relevance of ROBO3 signaling in PDA growth, invasion and metastases, we performed *in vivo* experiments in an orthotopic PDA model. For this purpose, one million cells were injected into the pancreas of NMRI Foxn1$^{nu/nu}$ mice of either PANC1 ROBO3 wild LacZ control cells or ROBO3 silenced, PANC1 dCas9-ROBO3 cells. During the experiment, we monitored the weight of the animals twice a week, as well as the tumor growth by weekly ultrasound imaging, recording height, width and depth of the tumor (Figure 33 B). However, due to animal well fare the animals had to be sacrificed at the latest 3 weeks after reaching a certain tumor diameter (> 8 mm).

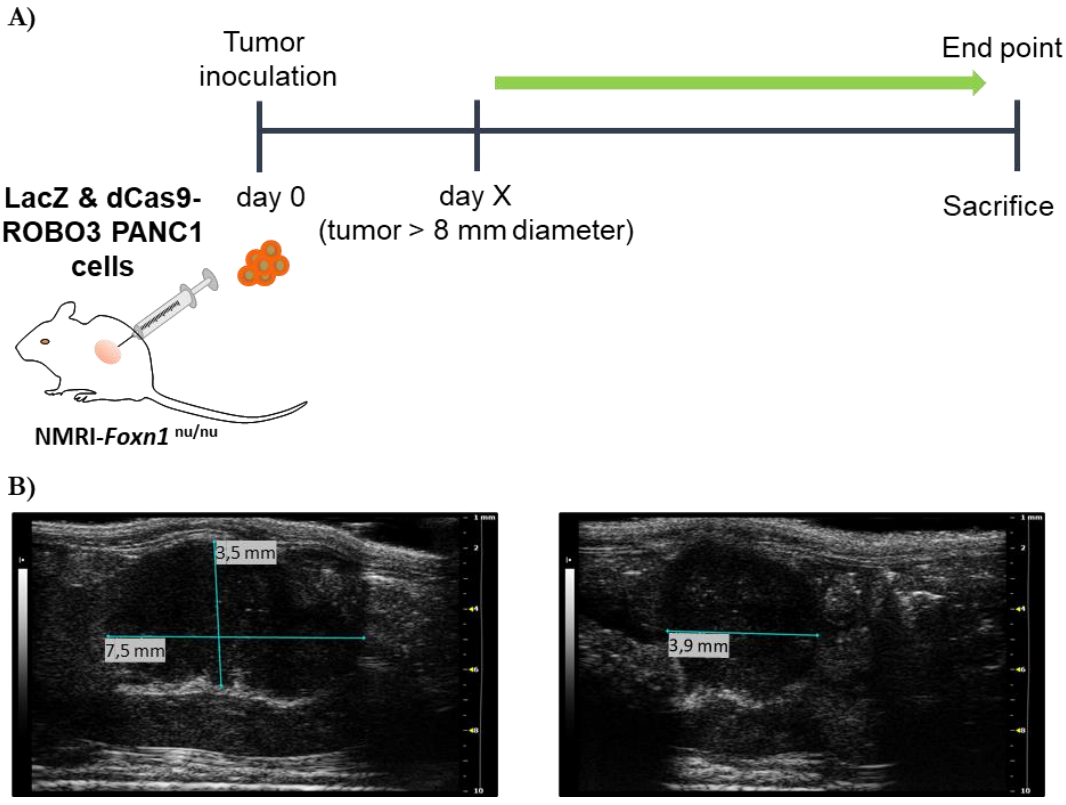

Figure 33. Experimental design for orthotopic implantation of ROBO3 silenced PANC1 cells *in vivo*. A) Model of the experimental design. Immunocompromised NMRI Foxn1nu/nu mice were injected by one million cells of PANC1 LacZ control cells and one million of ROBO3 silenced dCas9 PANC1 cells orthotopically into the pancreas. Once the tumors reached a decent size (>8 mm in diameter), it was only allowed to keep the mice alive for a maximum of 6 weeks according to the animal experiment application. B) Representative ultrasound images of an established orthotopic tumor of PANC1 cells *in vivo*.

The body weight did not significantly change between the groups during the entire course of the experiment, as well as we did not observe any severe weight loss, which would indicate a poor health condition of the animal.

After sacrificing the animals, the tumor (Figure 34 B) and the weight of the spleen (Figure 34 C) were recorded. No difference in tumor weight between LacZ control and ROBO3 knockdown was observed. Also, the weight of the spleen was not influenced. After ROBO3 silencing, the histology did not change significantly. In both cases, the implanted PANC1 cells form dedifferentiated, high-quality tumors.

After completion of the experiment, we additionally analyzed the survival although an end point was defined before the experiment since the LacZ control group reached the defined tumor size earlier and also performed worse in their clinical appearance due to massive ascites (Figure 35). The mean survival in the lacZ control group was 79 days, whereas the mean survival in the ROBO3 knockdown group was 83 days. Although the difference in mean survival is only 4 days, the survival of the ROBO3 knockdown group is significantly longer ($p < 0.0032$) compared to the LacZ control group, caused by some mice in the ROBO3 knockdown group who survived 90 days, while no mouse in the LacZ control group survived longer than 79 days due to massive tumor progress and metastasis (Figure 34 D). Survival statistics were calculated using the Log-rank (Mantel-Cox) test.

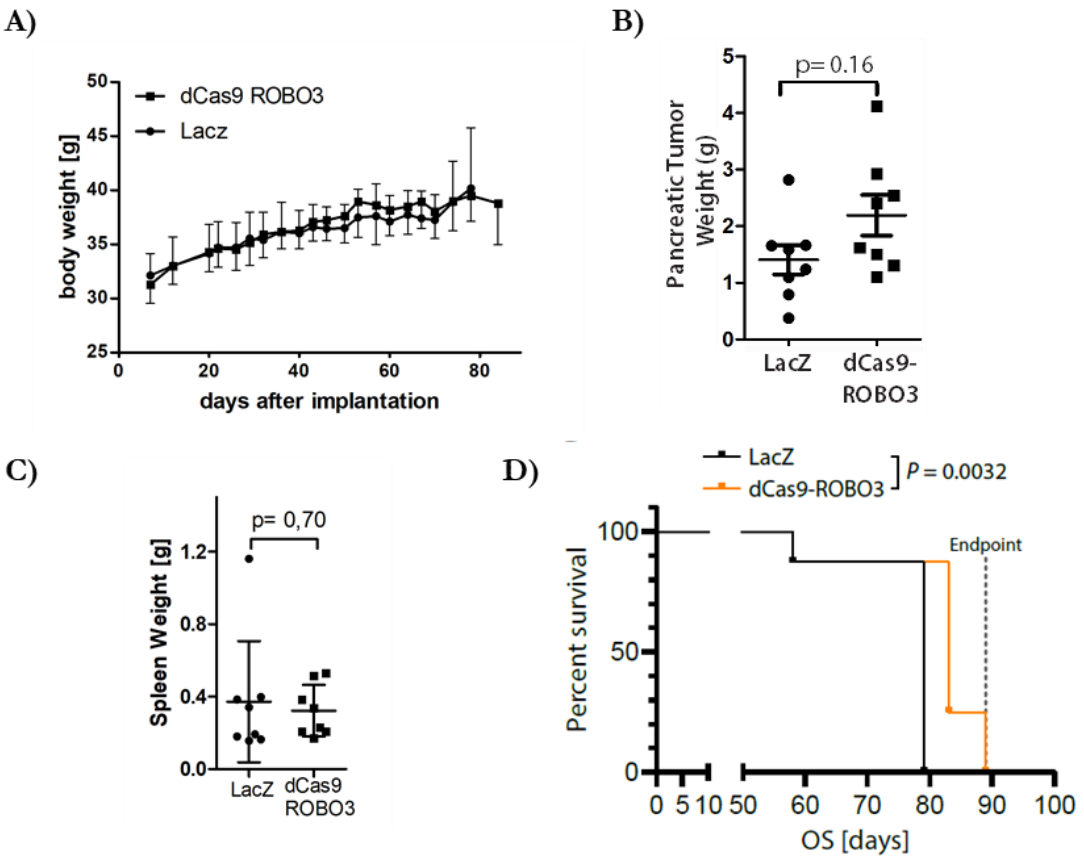

Figure 34. Disease Progression of orthotopic PANC1 tumors. A) Average body weight of LacZ control and dCas9 ROBO3 mice ± SD, from implantation to sacrifice. B) and C) Scatter plots of average tumor (B) and spleen (C) weight. Significance based on an unpaired Student's t-test is indicated by the p-value in the respective graph. D) Kaplan-Meier graph for survival analysis comparing the Lacz control and dCas9 ROBO3 cohort. Significance determined by Log-rank (Mantel-Cox) test. For all, LacZ control n = 8, dCas9 ROBO3 n = 8.

Since our *in vitro* experiments suggested that ROBO3 controls tumor cell invasion rather than growth, we also analyzed the metastasis rate. Furthermore, the clinical appearance of the mice was noticeably different during the experiment. In the LacZ control group, ascites was detected in 5 out of 8 experimental animals, which is an important clinical indicator for liver or peritoneal metastases, compared to only 1 out of 8 experimental animals in the ROBO3 knockdown group (Figure 35 D). Figure 35 A) and B) illustrate the difference in clinical appearance between the two study groups.

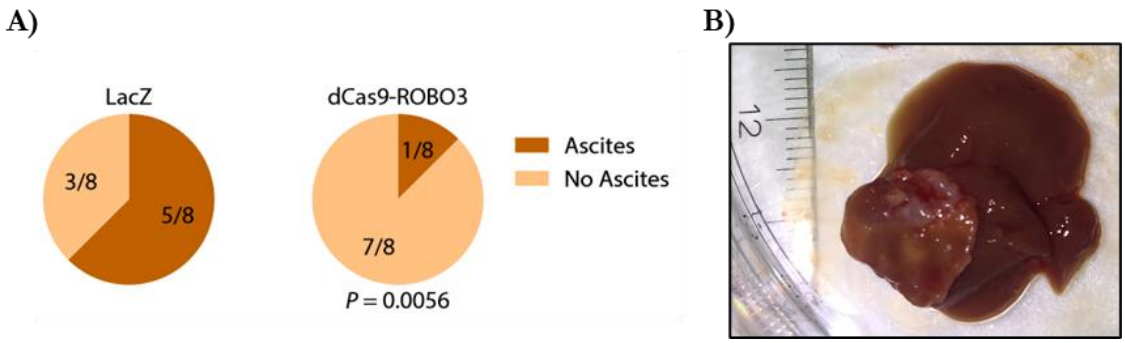

Figure 35. ROBO3 depletion leads to less ascites in orthotopic PANC1 PDA model. A) Ascites rates from dCas9 ROBO3 depleted mice and LacZ control mice during the orthotopic PANC1 animal experiment. Significance based on an unpaired Student's t-test is indicated by the p-value in the respective graph. B) Representative Image of macro-metastasis from a LacZ control mouse.

In order to investigate metastasis more closely, the entire liver tissue was embedded for further analysis. The relative metastatic area was determined by using H.E staining of the liver tissue at different cutting depths. The area of the respective metastasis in the liver was measured and subsequently divided by the whole liver area, to obtain a percentage value it was multiplied by factor 100. As illustrated in Figure 36 A), LacZ and ROBO3 knockdown group differ significantly, confirming clinical observations from the experiment and showing that mice with ROBO3 deficient inoculated tumor cells have less metastasis. In addition, we could show by immunofluorescence metastases clearly express ROBO3 and EGFP) (Figure 36 C), as expected from previous results (Figure 14) for cells belonging to the basal subtype. Through our lineage marker GFP it is also possible to clearly track our transfected cells, displaying the origin of the metastasis from the injected PANC1 cells

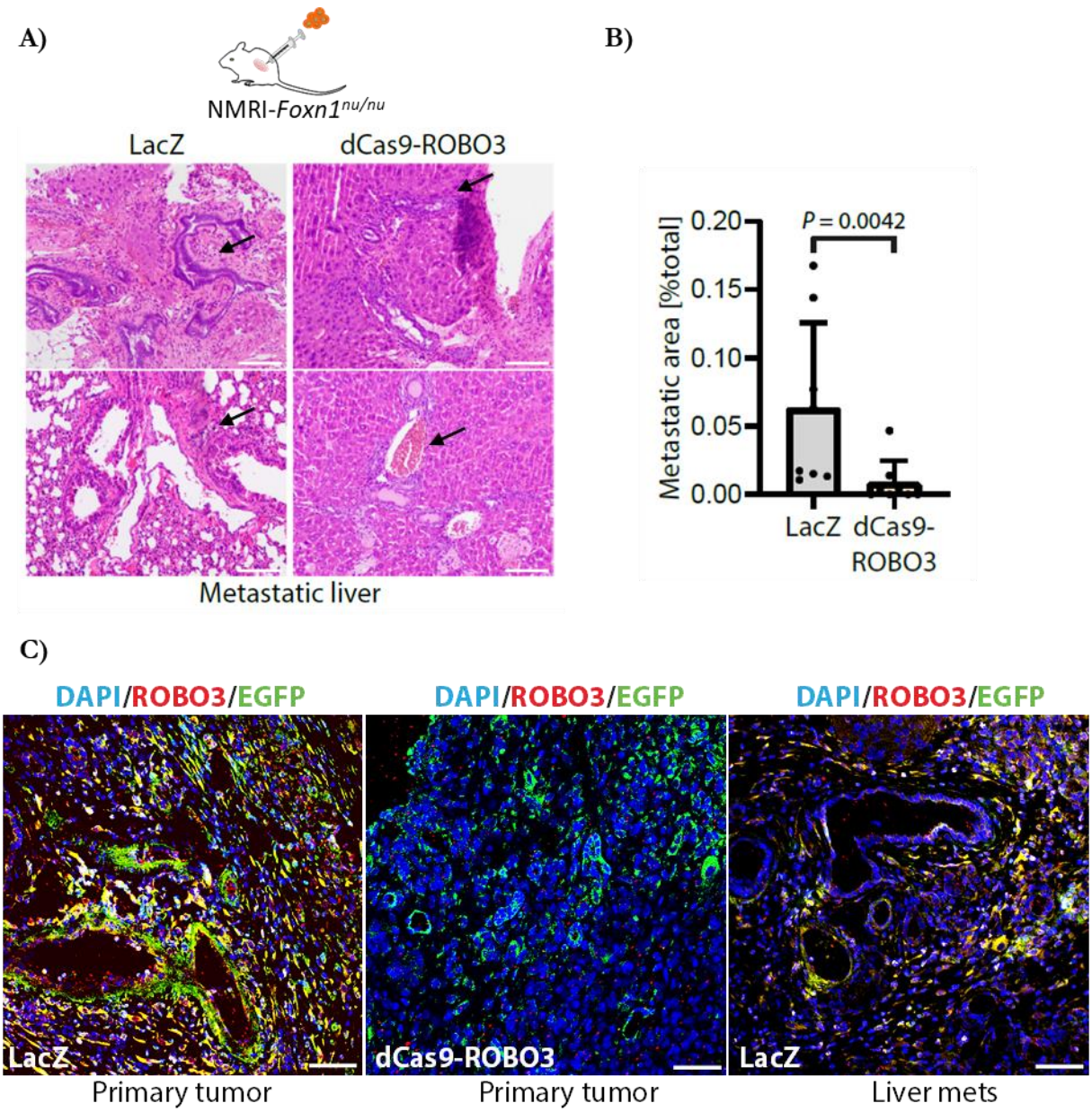

Figure 36. ROBO3 promotes metastasis in the orthotopic PANC1 PDA model. A) Representative H.E images of LacZ tumor liver metastasis. Scale bar 500 µm. B) Relative metastatic area comparison between dCas9 ROBO3 silenced mice and LacZ control mice in the orthotopic PANC1 PDA model (n=8 each group). Significance was determined by Mann-Whitney test. C) Representative IF image of primary LacZ and dCAs9-ROBO3 tumors as well as liver metastasis stained for ROBO3 and EGFP as a lineage marker. Scale bar 100 µm.

3.13 dCas9 ROBO3 knockdown imparted degradation of the ROBO3-pSTAT3 feed-forward loop in orthotopic *in vivo* model

In order to investigate whether pSTAT3 expression is also downregulated *in vivo* after ROBO3 silencing to validate our *in vitro* findings, we analyzed the tumors of at least 5 animals per group on the pSTAT3 levels. The pSTAT3 levels show a significant reduction of in ROBO3 dCas9 silenced tumors compared to LacZ tumors (Figure 37).

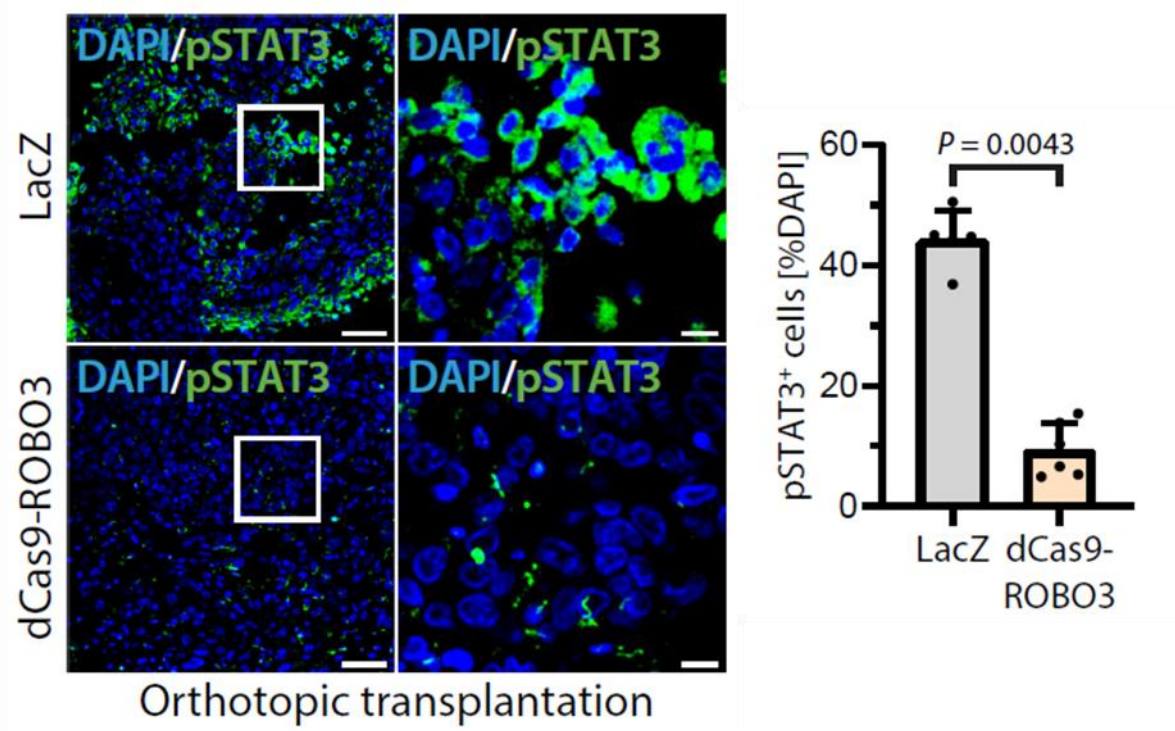

Figure 37. ROBO3 mediated downregulation of pSTAT3 levels in orthotopic dCas9 ROBO3 PANC1 PDA tumor model. Representative fluorescence microscopy images of primary LacZ and dCAs9-ROBO3 tumors as well as liver metastasis stained for pSTAT3 and KRT81 as a basal-like marker. Scale bar 50 μM. Scatter blot quantification of 5 Lacz and 6 dCas9-ROBO3 tumors with 10 images each, indicated as pSTAT3-positive per 20x field of view (F.o.V.).

3.13.1 Combination of Napabucasin and gemcitabine treatment in PDA cells

Based on our observations of the role of ROBO3 on invasiveness, we aimed to target ROBO3 pharmacologically. However, so far there is no inhibitor against ROBO3. Hence, we explored further therapeutic approaches which could potentially block ROBO3 mediated effects in PDA. As, our study identified pSTAT3 and AXL as potential downstream targets of ROBO3, we decided to use napabucasin as a known STAT3 and cancer stem cell inhibitor to test the effects on the ROBO3-mediated signaling axis. Figure 38 A) shows that, with increasing concentrations of napabucasin treatment in PANC1 cells, the pSTAT3 expression is significantly reduced. A significant effect can be observed at a concentration of 2 μM and above for a treatment duration of 24 hours. Additionally, a reduction of Sox2 and WNT10a is evident, while ROBO3 levels remain constant under napabucasin treatment.

To determine the effect of STAT3 inhibition on chemosensitivity, we analyzed the cell viability under napabucasin treatment alone or in combination with gemcitabine (standard chemotherapeutic agent for PDA) in GCDX-57 and GCDX-5 (Figure 38 B and C). Thereby, we observed a different response to the therapy. Both cell lines showed an insufficient response to therapy with gemcitabine alone, displayed by an IC50 concentration of 460 nM

for GCDX-5 and an IC50 value of 4.34 µM for GCDX-57. GCDX-57 showed a significantly higher IC50 value when treated with napabucasin at an IC50 concentration of 192 nM than GCDX-5 with 60 nM (Figure 38 B and C). However, the combination therapy of gemcitabine with napabucasin shows that in the GCDX-57 cell line a significant increase in efficacy and thus sensitivity to gemcitabine can be achieved, resulting in cells showing only 50% viability at a concentration of 68 nM. While in the case of GCDX-57 the IC-50 concentration is also lowest in combination therapy, but no significant increase in sensitivity to the chemotherapeutic agent can be observed compared to the other values (Figure 38 C). These results illustrate the heterogeneity and different response rates in the PDA.

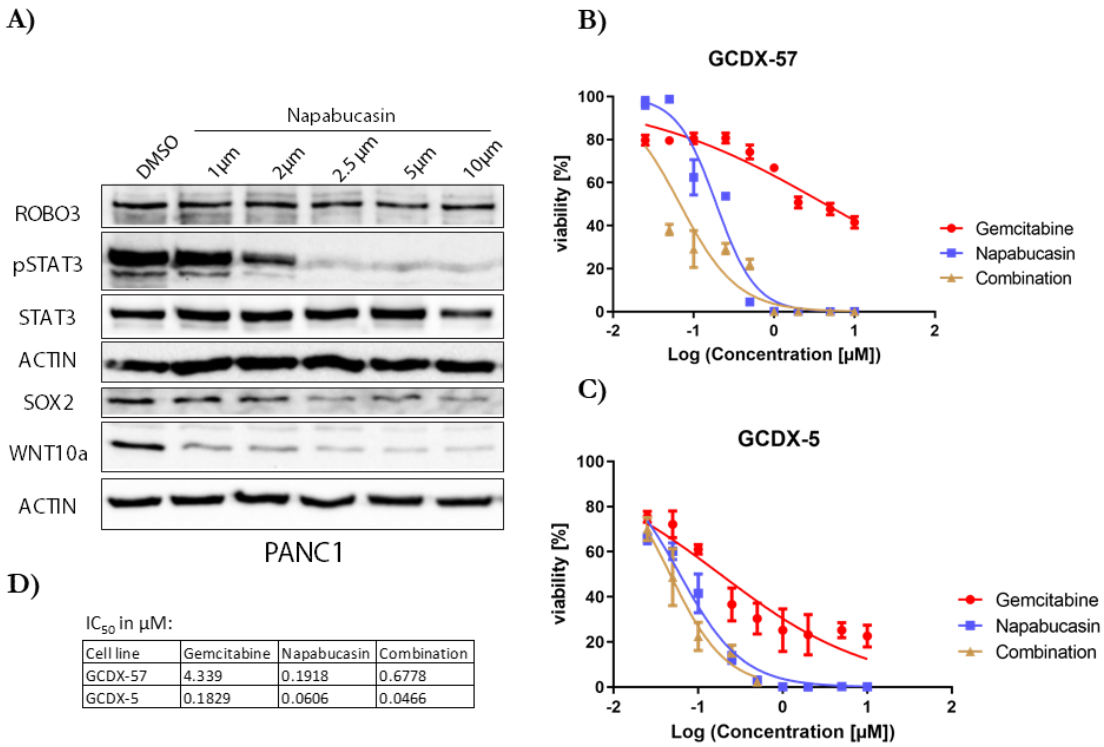

Figure 38. STAT3 inhibitor napabucasin increases the effectiveness of gemcitabine in selective cell lines and affects the expression of pSTAT3 and basal-like markers Wnt10a and Sox2. A) Immunoblot analysis of PANC1 cells following napabucasin treatment for 24 hours with indicated concentration antibodies was performed. The STAT3 antibody was probed after stripping pSTAT3 membrane. B-D) IC50-Concentration calculation from cell viability assay after gemcitabine, napabucasin and combination therapy in different concentrations for 72 hours using 3 replicates of indicated cell lines. n = 2.

3.13.2 Pharmacologically targeted inhibition of the tyrosine kinase AXL results in reduced STAT3 activity and proliferation

Next, we tested whether AXL inhibition through application of BGB324 (Bemcentinib) an agent that is currently being analyzed in phase III clinical trials. In this study we demonstrated

that AXL as a receptor tyrosine kinase is involved in the regulation of STAT3 activity, as illustrated in Figure 39. While the expression of ROBO3 and Wnt10a in the siRNA mediated AXL knockdown remains unaffected. We were particularly interested in the effect on cell viability following AXL knockdown alone and in combination with gemcitabine, since Ludwig et al. were able to show that the selective AXL kinase inhibitor BGB324 affects the tumor immune interface to attenuate the aggressive features of PDA cells in vitro and increase gemcitabine efficacy *in vivo* (Ludwig et al. 2018). To investigate the combined effect of AXL inhibition and gemcitabine, we performed a combination of siRNA mediated knockdown of AXL and gemcitabine administration for the basal-like cell lines PANC1 and MiaPaCa2 (Figure 39 B, C). The siRNA mediated knockdown alone led to a significant reduction in viability in both cell lines. An additional treatment with gemcitabine showed an even more significant reduction in viability. While an administration of gemcitabine alone in the concentrations of 50 μM and 100 μM has no significant effect on the viability of the cells (Figure 39 B, C).

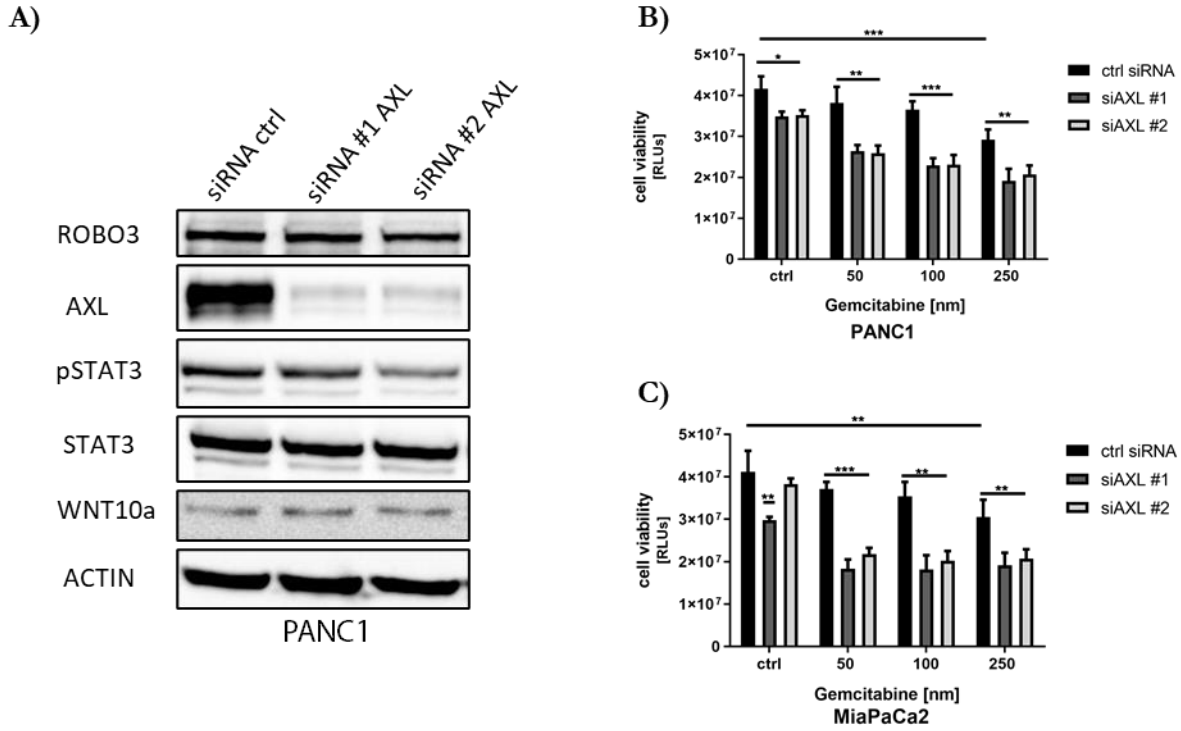

Figure 39. AXL knockdown leads to reduced STAT3 activity and proliferation in basal-like PDA phenotype. A) Immunoblot analysis of PANC1 cells following siRNA mediated AXL silencing using indicated antibodies was performed (n=2). The STAT3 antibody was probed after stripping pSTAT3 membrane. B) and C) Cell viability assay following combined siRNA mediated AXL silencing and gemcitabine treatment for 48 hours (3 replicates). Measured in relative light units (RLUs). Asterisks indicate significant changes to control treatment as determined by Kruskal-Wallis test and Dunn's Multiple Comparison Test. n = 2.

To test the inhibition of AXL with the pharmacological inhibitor BGB324 in basal-like or ROBO3 high PDA cell lines we used the cell viability assay to determine the IC50 concentration of BGB324 with different dosages. Figure 40 A) and B) show that PANC1 and MiaPaCa2 react analogously to BGB324 treatment and show an IC50 concentration of 44 nM and 61 nM. The PDX-derived cell line GCDX-5, on the other hand, shows a 50% reduction in viability only at a concentration of 251 nM. To investigate the molecular modifications after BGB324 treatment we performed an immunoblot assay after 6 and 24 hours of treatment with different concentrations. BGB324 reduces the phosphorylation of AXL so that total AXL remains unchanged as a result of the treatment. Interestingly, we can also observe that the phosphorylation of STAT3 is reduced with increasing concentrations during BGB324 treatment (Figure 40 A). These results are in line with our previous results, which show that pSTAT3 is significantly decreased as a result of AXL knockdown (Figure 39). After 6 hours of BGB324 treatment, a reduction of Wnt10a can also be detected.

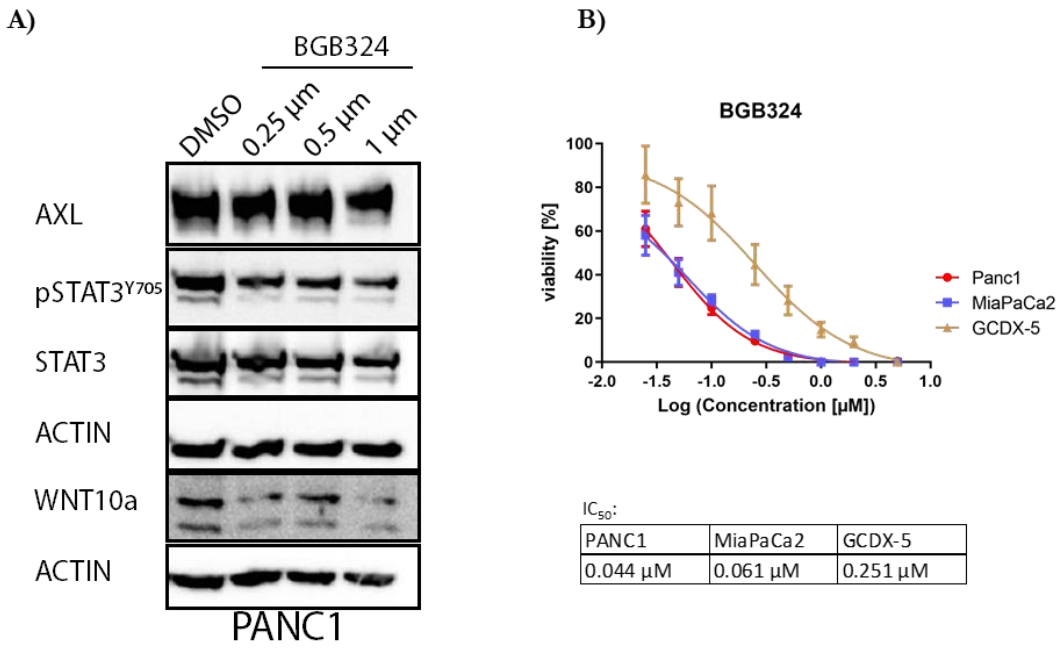

Figure 40. BGB324 (Bemcentinib) treatment in basal-like PDA phenotype leads to reduced pSTAT3 expression. A) Immunoblot analysis of PANC1 following BGB324 (Bemcentinib) treatment for 16 hours using indicated concentrations and antibodies. The STAT3 antibody was probed after stripping pSTAT3 membrane. B) IC50 calculations from cell viability assay following BGB324 (Bemcentinib) treatment for 24 hours using 3 replicates in indicated cell lines. n = 2.

4 Discussion

Despite enormous advancement in the molecular understanding, the prognosis of PDA is fatal and remains largely unchanged within the last decade. Specifically, the clinical outcome of advanced and metastatic PDA patients is extremely poor. Considerably, tumor stroma heterogeneity is a central biomedical obstacle in the prognosis and treatment of pancreatic cancer. Recent studies show that the axon guidance SLIT-ROBO pathway is frequently altered in PDA and associated with poor prognosis (Biankin et al. 2012; Bailey et al. 2016). This is in particular true for the member of axon guidance receptor family ROBO3 (Biankin et al. 2012), although the underlying mechanisms of ROBO3 driven tumor progression remain largely unknown. In this study, we identified a hierarchical regulatory network of ROBO3-signaling in tumor subtype-specific functions with a particular focus on tumor cell invasion, metastasis and drug resistance. For this purpose, we took advantage of various human and murine PDA cell lines, genetically engineered mouse models (GEMM), patient-derived xenografts and orthotopic PDA mouse models. Our findings revealed that ROBO3 signaling maintains STAT3 activity in tumor cells via AXL, a receptor tyrosine kinase family member. Together, we established that high levels of ROBO3 linked to aggressive basal-like metastatic PDA, where disrupting of the pathway initiates a subtype-switch towards a favorable classic-like PDA subtype. Notably, inactivation of ROBO3-signaling axis improve the chemotherapy response of PDA cells, thus rendering cells sensitive towards gemcitabine treatment.

Large-scale transcriptome analysis in PDA tumors identified that basal-like subtype substantially associated with poorly differentiated, metastatic phenotype and poor response to conventional therapy compared to classical PDA tumors. Most recently it has been shown that axon-guidance pathway significantly linked to basal-like phenotype in a PDA murine model. Axon guidance family mainly comprises SLIT, ROBO1, ROBO2 and ROBO3 molecules, where SLIT, ROBO1 and ROBO2, harbors a tumor suppressor functions in PDA (Biankin et al. 2012; Benjamin J. Raphael et al. 2017). While elevated expression of ROBO3 in PDA profoundly linked to poor clinical outcome (Biankin et al. 2012; Han et al. 2015), however, whether ROBO3 expressions underlie PDA subtype-specificity and disease aggressiveness remains elusive. In our hands, publicly available RNA-sequencing including protein expressions data in established PDA cell lines revealed that ROBO3 markedly elevated particularly in the high-grade/basal-like PDA compared to low-grade/classical PDA cell lines (Diaferia et al. 2016). Further, we also observed ROBO3 high expressions in the orthotopic primary

and metastatic PDA derived from basal-like cell lines. Together, these observations indicate that ROBO3 may involve in shaping high-grade/poorly differentiated basal-like subtype.

To further validate the correlation between tumor differentiation and ROBO3 expression, we took advantage of KPC (*Kras^{G12D}; Trp53^{R172H}; PDX Cre*) transgenic mouse model, which substantially recapitulates the low-grade/well differentiated to high-grade/poorly differentiated human PDA. Consistently, we also found a strong correlation between ROBO3 expression and tumor grading. In fact, the highest levels of ROBO3 were detected in poorly differentiated tumors (G3 and G4) that reflect the basal-like phenotype. In contrast, the expression of ROBO3 in epithelial and well-differentiated tumors (G1 and G2) was significantly lower, thus supporting the idea that ROBO3 expression is closely linked to the highly aggressive basal-like subtype (Figure 13). Of note, poorly differentiated (G3 and G4) PDA tumor cells are significantly associated with EMT and invasiveness (Diaferia et al. 2016; Miyabayashi et al. 2020; Puleo et al. 2018). Indeed, we found that genetic inactivation of ROBO3 reduced the expressions of EMT markers (e.g., SOX2 and ZEB1) and invasive potential of basal-like PDA cell lines (Figure 15). Consistent with these studies, we were also able to demonstrate that the invasive potential of PDX cell lines was reduced following siRNA mediated ROBO3 silencing (Figure 24 and Figure 25). It has been widely shown that early tumor invasiveness is prerequisite for the distant metastasis in solids tumors, including PDA. In particularly, EMT-like or highly invasive tumor cells potentially acquired chemoresistance features, and thus linked to extremely poor clinical outcome. Most recently, the first prospective clinical trial (NCT02750657) revealed the subtype-specific response of first-line chemotherapy (gemcitabine and Nab-paclitaxel or modified-FOLFIRINOX) in PDA patients with classical and basal-like subtypes (Aung et al. 2018). Consequently, PDA patients with classical subtype responded very well to first-line chemotherapy, whereas basal-like showed extremely poor response. Importantly, patients with classical tumors had significantly better survival in comparison to basal-like subtype (Aung et al. 2018). Thus, we also examined the role of ROBO3 in gemcitabine resistance. As shown in Figure 16, the basal-like cells with dCas9-ROBO3 knockdown showed a significant reduction in cell viability after gemcitabine treatment compared to LacZ control. Noteworthy, this effect was strongly associated with the basal-like subtype, thus indicating that ROBO3 may shape basal-like subtype aggressiveness via promoting therapy resistance in PDA.

A recent transcriptional profiling in PDA revealed lineage gene signatures for subtype-specific identity (Collisson et al. 2011; Moffitt et al. 2015; Bailey et al. 2016). For instance, AGR2, CAPN8 and GATA6 expressions are substantially associated with classical subtype identity,

whereas TNC, TP63, KRT5 and TGFBP expressions linked to basal-like tumors. To determine whether ROBO3 could influence PDA subtype-specificity, we performed transcriptome profiling upon ROBO3 silencing in BL cells. We identified that BL hallmarks signatures such as EMT, Mitotic-spindle and Apical-Junction were significantly downregulated upon ROBO3 silencing (Figure 18). These gene sets determine invasive properties of tumor cells and thus also reflect the loss of invasive potential after ROBO3 knockdown in the 3D-transwell invasion assay. Further, we observed that loss of ROBO3 led to downregulation of BL lineage-gene signatures (e. g. KRT5) and simultaneously upregulation of CLA lineage-gens (e. g. AGR2), respectively (Figure 19). These transcriptomic effects emphasize the importance of ROBO3 as a potential mediator between the prognostic relevant subtypes in PDA and the possibility to suppress EMT-like transcriptional profile and invasiveness by inhibiting this signaling pathway.

To elucidate the molecular mechanism of the ROBO3 mediated EMT, invasion and subtype maintenance in PDA, we focused on the IL-6/STAT3 pathway, which in particularly altered in ROBO3 depleted RNA-seq profile. IL-6/STAT3 regulatory network widely linked to EMT, invasion and metastasis in solid tumors (Sullivan et al. 2009; Yadav et al. 2011; Xiong et al. 2014; Gong et al. 2017). In PDA, IL6/STAT3 role has recently been established in pre-metastatic niche formation and disease aggressiveness (Lee and Beatty 2020). In detail, STAT3 was characterized as an important oncogenic factor in a number of epithelial malignancies, including PDA, where the constitutive activation of STAT3 by phosphorylation of Tyr705 was observed in 30-100% of human tumor samples and in many PDA cell lines (Scholz et al. 2003; Toyonaga et al. 2003). In our study, we found that pSTAT3 is highly expressed in basal-like phenotype, especially in MiaPaCa2, while CAPAN1 as classical phenotype and L3.6 have very low levels, indicating a prognostic relevance of pSTAT3 ^{Tyr705} expression (Figure 21), which is also evidenced in literature (Li et al. 2015; HUANG et al. 2012). In line with the results of RNA-Seq, both dCas9 mediated and siRNA mediated ROBO3 knockdown revealed significant downregulation of pSTAT3^{Tyr705} along with EMT gene signatures such as SOX2, while total STAT3 was unaffected (Figure 15). This underlines the possible regulation of ROBO3 via the regulation of pSTAT3^{Tyr705} level. In order to exclude a possible STAT3 dependent regulation of ROBO3, a siRNA mediated knockdown of STAT3 was performed, resulting in no difference in ROBO3 expression, hence it can be assumed that the transmembrane receptor ROBO3 regulates the transcription factor STAT3 as downstream target and the expression of ROBO3 is independent of STAT3 (Figure 22)To further validate the ROBO3 mediated STAT3 activity, we examined the expression of WNT10A which is a potential downstream target gene of active STAT3 (Baumgart et al.

2014). Previously, we have shown that NFATc1 (Nuclear factor of activated T-cells, cytoplasmic 1) and STAT3 directly binds on the active enhancer site of WNT10A to regulate its oncogenic functions in PDA progression (Baumgart et al. 2014). Consistently, we found that WNT10A expression was reduced in the inactive STAT3 conditions, only upon ROBO3 silenced BL cells. Of note, we also observed a marked reduction of WNT10A expression in ROBO3 silenced RNA-seq profile. In addition, we could identify that dCas9-mediated overexpression of ROBO3 in the CLAS cell lines CAPAN1 and CAPAN2 leads to induction of pSTAT3 ^{Tyr705}, which underlines the ROBO3-dependent phosphorylation of STAT3 (Figure 22). As reported previously, ROBO3 is a transmembrane receptor protein without any autocatalytic or enzymatic activity, which raises the question of how ROBO3 controls the phosphorylation of STAT3 (Blockus and Chédotal 2016). It has been shown that NELL2 ligand (neural EGFL-like 2) potentially binds to ROBO3 receptor to regulate neuronal development (Jaworski et al. 2015; Pak et al. 2020). On the other hand, EGF-receptor conjugates with IL6/gp130 to activate STAT3 to promote inflammatory mechanisms (Wang et al. 2013). However, the ligand for ROBO3 receptor and its activation remains unclear in PDA. We anticipated that secreted IL6 from the PDA cell lines may bind as a ligand to ROBO3 receptor, which, in turn, phosphorylate STAT3. Interestingly, we observed that exogenous IL-6 treatment increases ROBO3 expressions both in classical and basal-like cell lines, indicated that IL-6 as a ligand may directly binds to ROBO3 receptor to activate STAT3. Therefore, we examined the endogenous IL6 levels by flow-cytometry analysis in the corresponding classical (CAPAN1, CAPAN2) and basal-like (PANC1, MiaPaCa2) cell lines. Surprisingly, none of the classical or basal-like cell lines expressed IL6 (data not shown). Thus, these results indicate that ROBO3-mediated STAT3 phosphorylation/activation could be driven by IL6 independent receptor tyrosine kinase (RTK) activity in PDA cells.

Notably, our RNA-seq profile identified a potential RTK 'AXL' which was downregulated upon ROBO3 silencing in BL cells. AXL belongs to the subfamily of TAM (Ty-ro3, AXL, MerTK), and its high expression profoundly linked to tumor aggressiveness, drug-resistant and metastatic phenotype in variety of malignant tumor types (Gjerdrum et al. 2010; Wu et al. 2014; Rankin and Giaccia 2016; Cruz et al. 2019). AXL high expressions strongly linked to mesenchymal-like phenotype in PDA (Leconet et al. 2014). Further, CRISPR mediated knockdown of AXL led to reduced tumor growth and metastasis in preclinical models of PDA (Leconet et al. 2014; Ludwig et al. 2018; Goyette et al. 2019; Du et al. 2019). Additionally, similar results were obtained by pharmaceutical inhibition of AXL by BGB324 inhibitor in the orthotopic PDA tumor models (Ludwig et al. 2018). Importantly, AXL inhibitor BGB324 is currently under phase-II clinical trials (NCT03649321) in advanced PDA.

Whether AXL regulates STAT3 phosphorylation/activation in PDA remains unknown. Most recent study on single-cell proteomic in lung cancer revealed the downstream kinase activity of AXL which includes JAK-STAT3 and TGFβ proteins (Taverna et al. 2020). Phosphorylation of STAT3 by AXL has not previously been described, however, the function as tyrosine kinase and the specific phosphorylation of STAT3 at tyrosine 705 led us to further investigate AXL as a possible downstream target. As presented in Figure 19 and Figure 26, a knockdown of ROBO3 leads to a reduced expression of AXL both at mRNA and the protein levels in established PDA as well as in PDX cell lines. Further, we found that both pharmacological inhibition and siRNA-mediated knockdown of AXL similarly causes reduced pSTAT3 ^{Tyr705} levels, indicating that AXL regulates STAT3 activity in PDA. To explore pSTAT3 Tyr705 levels following AXL inhibition in more detail, an orthotopic PDA *in vivo* mouse model with pharmacological AXL inhibition via BGB324 in comparison with standard chemotherapy would be appropriate. Thus, our findings indicate that ROBO3 positively regulate AXL to maintain basal-like plasticity. Next, we investigated the functional relevance of AXL on tumor cell invasion and therapy resistance *in vitro* in basal-like cells. As shown in Figure 28 and Figure 39 siRNA mediated silencing of AXL led to a significantly reduced invasion and increased gemcitabine response of basal-like PDA cells. These results are consistence with the previous findings by Ludwig et al., where pharmacological inhibition of AXL by BGB324 profoundly induced gemcitabine effectiveness in preventing distant metastasis, and simultaneously reduced the inflammatory TME in PDA. Consistently, we identified that genetic knockdown of ROBO3 led to reduced invasion and liver metastasis in basal-like PDA orthotopic model. Whether loss of ROBO3 impacts on inflammatory TME need further investigation. Together, these findings may suggest that ROBO3 maintain PDA aggressiveness by AXL-STAT3 regulatory axis in IL-6 independent mechanisms.

In PDA, inflammatory TME plays a critical role in tumor progression, metastatic niche formation and therapy resistance (Foucher et al. 2018; Neesse et al. 2019). Chronic inflammation is increasingly indicated to alter the TME through a variety of mechanisms, including cytokine/chemokine production, inflammatory immune cells recruitment and cellular reprograming of cancer-associated fibroblasts (CAFs). Recent large-scale transcriptome analysis in 308 PDA patient biopsies identified that IL-6 and TNFα (tumor necrosis factor α) are the two most predominant cytokines in the inflammatory stromal components (Puleo et al. 2018). Of note, reciprocal interaction between inflammatory or immune stromal components with basal-like and classical subtype significantly determine the clinical outcome of PDA patients. Furthermore, abundance of ECM-rich stromal components in basal-like tu-

mors associated with poor prognosis in PDA patients (Maurer et al. 2019). Whether inflammatory cytokines such as IL-6 involved in PDA subtype-shaping remains unknown so far. We observed that treatment of pro-inflammatory cytokine IL-6 profoundly induces ROBO3 expressions, and thus prolonged AXL mediated STAT3 activity in both classical and basal-like cell lines. Notably, however, exogenous IL-6 failed to induce AXL-STAT3 regulatory axis in the ROBO3 silenced basal-like cell lines. Whereas IL-6 treatment induces STAT3 activity in the AXL depleted basal-like cells. This suggests that AXL mediated STAT3 activation is independent of IL-6 mechanisms. In PDA, IL-6-STAT3 signaling in the TME plays an essential role for pre-metastatic niche formation. Further, it has been shown that inflammatory stromal components such as IL-6 and TNFα positively associated with basal-like PDA subtype, whereas immune stromal components such as CD4 T cells signaling linked to CLA subtype (Puleo et al. 2018). Thus far, our findings indicate that basal-like subtype-specific ROBO3 mediated tumor invasiveness and basal-like subtype specificity can be triggered by inflammatory cytokines (e. g. IL-6) in PDA.

Basal-like subtype-specificity profoundly linked to poorly differentiated, metastatic and therapy resistance phenotype. We noted that ROBO3 expression was relatively higher in high-grade/poorly differentiated tumors derived from basal-like orthotopic and KPC mice, respectively. We next investigated whether ROBO3 promotes tumor invasiveness and distant metastasis in preclinical mouse model. Here, we orthotopically implanted our dCas9-ROBO3 and LacZ BL PDA cells into the pancreata of nude mice. Strikingly, we noted that dCas9-ROBO3 mice showed reduced ascites compared to LacZ control mice. Also, as expected, we observed significantly reduced liver metastasis particularly in the dCas9-ROBO3 mice. Further, we found a marked reduction of both pSTAT3 and KRT81 (BL lineage marker) in the primary tumors derived from dCas9-ROBO3 mice. Notably, dCas9-ROBO3 cohort showed improved survival benefit compared to its LacZ control mice. On the other hand, relative tumor volume was unchanged in dCas9-ROBO3 mice compared to LacZ control mice. This suggests that ROBO3 is critical for maintaining BL subtype-specificity via modulating metastatic dissemination. Whether tumors derived from dCas9-ROBO3 mice modulate stromal components need further investigation. In general, immunocompromised animals have limited access to stromal immune cells such as fibroblasts and macrophages. Thus, to investigate the reciprocal interaction between neoplastic-epithelial ROBO3-AXL-STAT3 regulatory network and the inflammatory stromal microenvironment (e.g., IL-6) requires an immunocompetent preclinical mouse model.

The major aim of this study was to characterize ROBO3 in PDA subtype maintenance, disease aggressiveness and therapy response. Our findings indicate that ROBO3 signaling play a crucial role in basal-like metastatic program, and thus pharmacological targeting of this pathway may overcome disease aggressiveness and improve therapy response in PDA. Unfortunately, pharmacological inhibitor against ROBO3 has not been identified so far. Thus, we looked for a plausible alternatives to therapeutically intervene ROBO3 associated AXL-STAT3 regulatory axis. It has been shown that both AXL and STAT3 can be pharmacologically targeted in solid cancers including PDA. Hence, we first started testing basal-like cell lines with STAT3 inhibitor (napabucasin). The inhibition of STAT3 pathways, limiting stem cell activity in cancer cells, by napabucasin was investigated in Phase III clinical trials in PDA (NCT02993731). In our hand, napabucasin treatment substantially reduced pSTAT3 and WNT10A protein levels in a dose dependent manner, thus indicating the napabucasin specificity mainly towards STAT3 activity. Indeed, we found a marked reduction of cell viability upon combinatorial treatment of napabucasin and gemcitabine *in vitro*. Whether this combinatorial treatment impacts disease aggressiveness and improve preclinical outcome of basal-like tumors require further validations in mouse models. Although, most recent findings revealed that the randomized CanStem111P napabucasin phase-III clinical trials (NCT02993731) for metastatic PDA patients discontinued because of futility (Boston Biomedical 2019). Most likely, unconditional targeting of vital factors including safety and efficacy of napabucasin could be potential cause of futility. Notably, we found that AXL maintains STAT3 activity via ROBO3 signaling. As noted above, inhibition of AXL leads to improve pre-clinical outcome. In particularly, AXL inhibitor 'BGB324' treatment results in pre-clinical models of PDA were highly encouraging. Of note, targeting AXL either by BGB324 or genetic inactivation led to reduced metastasis and improved chemotherapy response in *Kras^{G12D};Ink4a$^{fl/fl}$;PDX Cre* (KIC) mouse model (Ludwig et al. 2018). In line with this, our results provide a strong evidence on AXL-mediated STAT3 activity, we identified that AXL knockdown substantially attenuates ROBO3-mediated pSTAT3 expressions in basal-like cell lines. Therefore, pharmaceutical inhibition of AXL may hold a promising therapeutic alternatives of STAT3, mainly in the ROBO3-high expressing PDA. One other important aspect of our findings was the regulation of ROBO3-AXL-STAT3 regulatory loop by the inflammatory cytokine IL-6. Of note, inflammatory stromal components (e.g., IL-6) positively associated with pre-metastatic niche formation in PDA. Importantly, it has been shown that AXL inhibition via BGB324 substantially reduces stromal components and inflammatory cytokines such as IL-6, CCL11 (C-C Motif Chemokine Ligand 11) and IL-1β (Interleukin 1 beta) in the pre-clinical models. These findings suggest that pharmaceutical

inhibition of AXL disrupts reciprocal interaction between inflammatory stroma and tumor epithelium in the TME (Ludwig et al. 2018). Therefore, AXL inhibition may not only lead to the inhibition ROBO3-STAT3 nexus in the neoplastic-epithelium, but also interferes with the inflammatory IL-6 production that enforces ROBO3-mediated AXL-STAT3 regulatory network in PDA aggressiveness (Figure 41). For the tailored therapy, STAT3 inhibition can also be regarded as a possibility to interfere ROBO3-mediated signaling, but whether STAT3 inhibition affects inflammatory TME needs further validation. Together, we provide a ROBO3-mediated hierarchical regulatory network, which determines invasive-metastatic plasticity and therapy response in basal-like PDA. Thus, pharmacological targeting of ROBO3-AXL-STAT3 signaling axis may overcome therapy response and offer favorable prognosis in PDA patients (Figure 42).

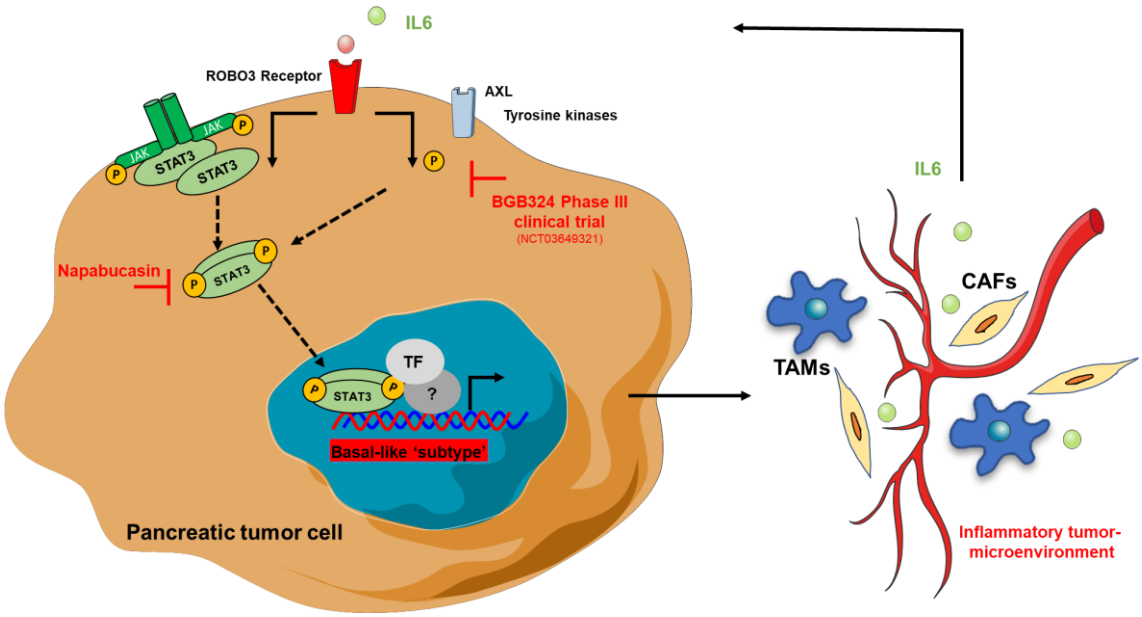

Figure 41. Working model of ROBO3 signaling in PDA. Illustration of ROBO3 mediated signaling in basal-like PDA subtype. ROBO3 controls the IL-6/STAT3-axis in PDA by regulating the expression of the tyrosine kinase AXL and subsequent phosphorylation of STAT3. The inflammatory cytokine IL-6 is capable to induce ROBO3 expression, thereby enhancing this feed-forward-loop. Napabucasin and BGB342 are potential inhibitors of ROBO3 driven signaling in PDA. Made by using Servier Medical Art.

4.1 Conclusion

Altogeher, our findings establish that axon guidance molecule ROBO3 maintain subtype-specificity, metastatic progression and therapy resistance in PDA. We have identified a novel hierarchical regulatory network, which determines invasive and high-grade/basal-like subtype identity via regulating lineage-specific gene signatures. In PDA, ROBO3 depletion attenuates EMT and basal-like-specifc lineage program, whereas classical associated gene signatures upregulated. Mechanistically, ROBO3 governs STAT3 activity through tyrosin phosphorylation in IL-6 independent mechanisms. We provide the first evidence that AXL serves as a tyrosine kinase to activate STAT3 in the neoplastic-epithelial cells via ROBO3 mediated signaling axis. On the other hand, exogenous IL-6 induced STAT3 activity deprived in the absence of ROBO3 both in classical and basal-like PDA cells. Notably, genetic silencing of either ROBO3 or AXL attenuates tumor cells invasiveness and improve chemotherapy response in basal-like PDA (Figure 41). In pre-clinical study, orthotopic implanted dCas9-ROBO3 animals showed reduce ascites and liver metastasis, subsequentally leding to better survival benefits. Notably, pharmacological inhibition of ROBO3 mediated AXL-STAT3 loop by clinically approved inhbititors (napabucasin and BGB324) improve therapy efficacy and reduces cell viability of basal-ike cells. Therefore, we conclude that targeting ROBO3-AXL-STAT3 reulatory network may re-establish more favorable clinical outcome in basal-like aggressive PDA (Figure 42).

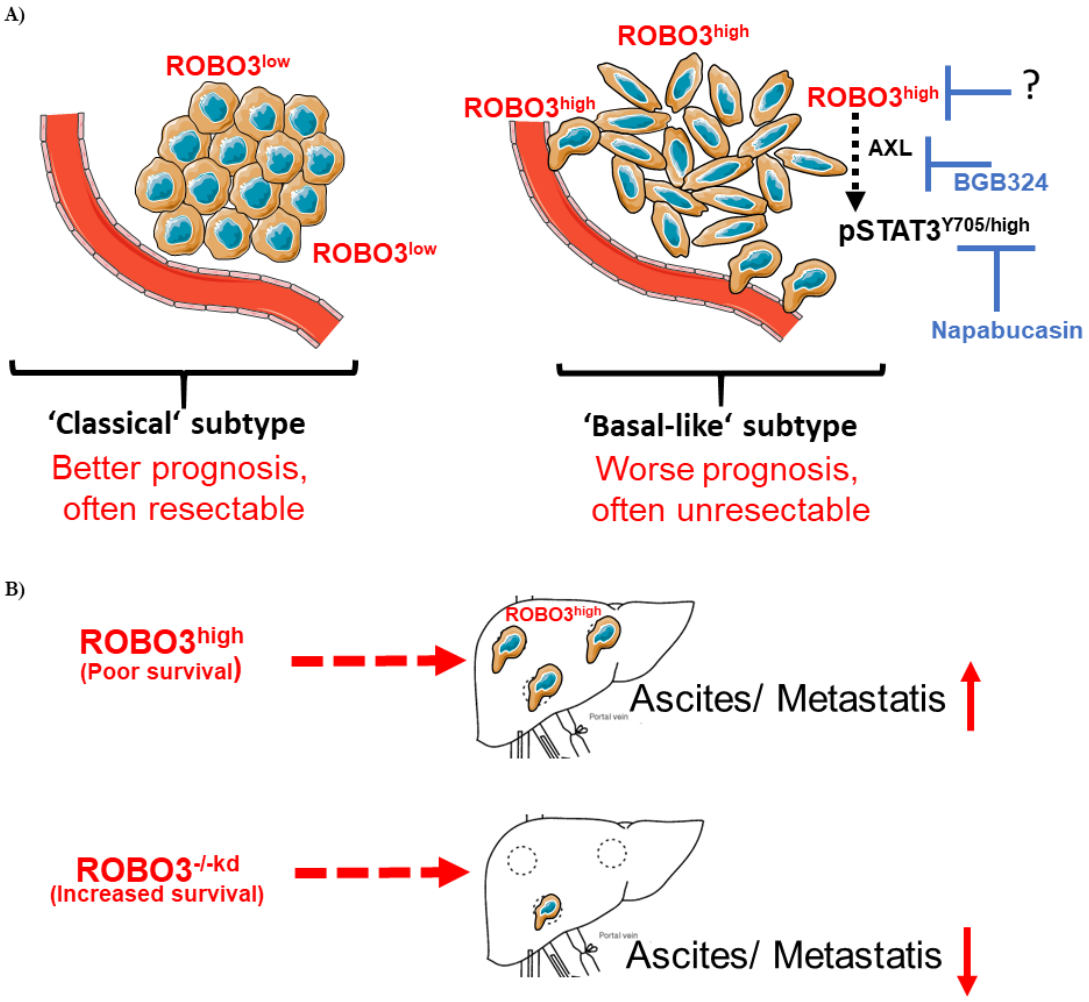

Figure 42. Summarized major findings of Axon guidance receptor ROBO3 mediated signaling in pancreatic cancer cell plasticity. A) ROBO3 expression in different PDA subtypes and downstream signaling cascade driven via tyrosine kinase AXL mediated phosphorylation of STAT3. B) Orthotopic PANC1 model revealed a better overall survival and less metastasis in ROBO3 dCas9 silenced tumors. Made by using Servier Medical Art.

5 Summary

Pancreatic ductal adenocarcinoma remains one of the most aggressive cancers with a 5-year survival rate below 10 %. Particularly, the clinical outcome of metastatic pancreatic cancer is extremely poor with a dismal 5-year survival rate below 3 %. Several factors influence the high therapy resistance. The tumor microenvironment is one of them, which exhibits a complex and heterogeneous structure within the neoplastic-epithelium and stromal cells compartments, making treatment strategies extremely challenging in pancreatic cancer patients. Whole-exome sequencing and transcriptional profiling in tumor biopsies identified distinct molecular subtypes of pancreatic cancer, which correspond with prognosis and therapeutic outcome of patients. In particularly, the 'basal-like' subtype is substantially linked to EMT, high rates of metastasis and a therapy resistance phenotype, thus leading to a poor prognosis. Whereas the 'classical' subtype is markedly associated with a better therapy responsiveness leading to a preferable prognostic outcome in pancreatic cancer patients. In this study, we demonstrate that axon-guidance receptor 'ROBO3' promotes poorly differentiated and metastatic basal-like phenotypes both *in vitro* and *in vivo* pancreatic cancer models. We identified that ROBO3 promotes tumor invasiveness and therapy resistance of basal-like pancreatic cancer cells. Notably, our CRISPR/dCas9-mediated ROBO3 inactivation confirmed its role in the orthotopic pancreatic mouse model. We show that ROBO3 activates STAT3 by phosphorylation at tyrosine-705 in an IL-6 independent mechanisms. Importantly, the IL-6/STAT3 regulatory mechanisms has already been identified as key event in the pre-metastatic niche formation in pancreatic cancer. We found that exogenous IL-6 induces ROBO3 and pSTAT3 expressions. However, ROBO3 silencing restricts IL-6 mediated STAT3 activation in basal-like cells. Mechanistically, ROBO3 directly controls receptor tyrosine kinase family member AXL, which in turn activates STAT3 in basal-like cells. Thus, ROBO3 or AXL depletion led to reduced invasiveness and improve chemo-responsiveness in basal-like cells. Furthermore, pharmacological inhibition of STAT3 or AXL substantially improves chemo-responsiveness towards gemcitabine in pancreatic cancer cells. Together, this study indicates that targeting ROBO3-mediated regulatory network may restore favorable outcome in a defined subgroup of pancreatic cancer patients.

6 Zusammenfassung

Das duktale Adenokarzinom der Bauchspeicheldrüse ist nach wie vor eine der aggressivsten Krebsentitäten mit einer 5-Jahres-Überlebensrate von unter 10%. Insbesondere das klinische Behandlungsergebnis von metastasiertem Bauchspeicheldrüsenkrebs ist ausgesprochen schlecht mit einer 5-Jahres-Überlebensrate von unter 3%. Ein wichtiger Faktor der sowohl die Prognose als auch die Behandlung von Patienten mit Pankreaskarzinom zu einer großen Herausforderung macht ist Tumormikroumgebung, welche eine komplexe Heterogenität innerhalb des neoplastischen Epithel- und Stromazellenkompartiments aufweist. Studien der letzten Jahre, welche die Sequenzierung des Exoms und transkriptionelle Analysen von humanen Tumorbiopsien beinhalten, konnten verschiedene molekulare Subtypen identifizierten. Diese Subtypen unterschieden sich auch weitgehend in dem therapeutischen Ansprechen und folglich in der Prognose der Patienten. Insbesondere der "basal-like"-Subtyp zeigt einen metastatischen und therapieresistenten Phänotyp und weist daher eine schlechte Prognose auf. Während der "classical"-Subtyp durch seine besseres Therapieansprechen mit einer günstigeren Prognose bei Patienten assoziiert ist. In dieser Studie konnten wir nachweisen, dass der Axonsteuerungs-Rezeptor „ROBO3“ den schlecht differenzierten und metastatischen basal-like-Phänotyp, sowohl *in vitro* als auch *in vivo* Pankreaskarzinom-Modellen fördert. Wir konnten feststellen, dass ROBO3 die Tumor Invasivität und Therapieresistenz von basal-like-Pankreaskarzinomzellen verstärkt. Insbesondere führte die CRISPR/dCas9-vermittelte ROBO3-Inaktivierung zu einer Reduzierung der Bildung von malignem Aszites und der Lebermetastasierung von basal-like Tumoren im orthotopen Pankreas-Mausmodell. Wir demonstrieren, dass ROBO3 in einem IL-6-unabhängigen Mechanismus STAT3 durch Phosphorylierung am Tyrosin-705 aktiviert. Die IL-6/STAT3-Regulationsmechanismen sind als Schlüsselereignis bei der prä-metastatischen Nischenbildung im Pankreaskarzinom identifiziert worden. Wir fanden heraus, dass exogenes IL-6 die Expression von ROBO3 und pSTAT3 induziert, jedoch schränkt die Inaktivierung von ROBO3 die IL-6-vermittelte STAT3-Aktivierung in basal-like Tumorzellen ein. Mechanistisch kontrolliert ROBO3 direkt das Rezeptortyrosinkinase-Familienmitglied AXL, das wiederum STAT3 in den basal-like Tumorzellen aktiviert. Insbesondere führte die Depletion von ROBO3 oder AXL zu einer reduzierten Invasivität und einer verbesserten Chemotherapie-Responsivität in Basal-like Tumorzellen. Darüber hinaus verbessert die pharmakologische Hemmung von STAT3 (durch Napabucasin) oder AXL (durch BGB324) die Chemotherapie-Responsivität von Gemcitabin in Pankreaskarzinomzellen erheblich. Die Unterbrechung der hierarchischen regulatorischen ROBO3-AXL-STAT3-Achse ermöglicht daher eine Wiederherstellung der

vorteilhaften Subtypidentität bei Pankreaskarzinom. Zusammenfassend zeigt diese Arbeit, dass die Beeinflussung des ROBO3-vermittelten regulatorischen Netzwerks bei einer definierten Untergruppe von Pankreaskarzinom-Patienten ein positives Therapieergebnis wiederherstellen könnte.

Bibliography

Aiello NM, Maddipati R, Norgard RJ, Balli D, Li J, Yuan S, Yamazoe T, Black T, Sahmoud A, Furth EE et al. (2018): EMT Subtype Influences Epithelial Plasticity and Mode of Cell Migration. Dev Cell 45, 681-695.e4

Aung KL, Fischer SE, Denroche RE, Jang G-H, Dodd A, Creighton S, Southwood B, Liang S-B, Chadwick D, Zhang A et al. (2018): Genomics-Driven Precision Medicine for Advanced Pancreatic Cancer: Early Results from the COMPASS Trial. Clin Cancer Res 24, 1344–1354

Bailey P, Chang DK, Nones K, Johns AL, Patch A-M, Gingras M-C, Miller DK, Christ AN, Bruxner TJC, Quinn MC et al. (2016): Genomic analyses identify molecular subtypes of pancreatic cancer. Nature 531, 47–52

Ballard MS, Hinck L (2012): A roundabout way to cancer. Adv Cancer Res 114, 187–235

Baumgart S, Chen N-M, Siveke JT, König A, Zhang J-S, Singh SK, Wolf E, Bartkuhn M, Esposito I, Heßmann E et al. (2014): Inflammation-induced NFATc1-STAT3 transcription complex promotes pancreatic cancer initiation by KrasG12D. Cancer Discov 4, 688–701

Becker AE, Hernandez YG, Frucht H, Lucas AL (2014): Pancreatic ductal adenocarcinoma: risk factors, screening, and early detection. World J Gastroenterol 20, 11182–11198

Benjamin J. Raphael, Ralph H. Hruban, Andrew J. Aguirre, Richard A. Moffitt, Jen Jen Yeh, Chip Stewart, A. Gordon Robertson, Andrew D. Cherniack, Manaswi Gupta, Gad Getz et al. (2017): Integrated Genomic Characterization of Pancreatic Ductal Adenocarcinoma. Cancer Cell 32, 185-203.e13

Biankin AV, Waddell N, Kassahn KS, Gingras M-C, Muthuswamy LB, Johns AL, Miller DK, Wilson PJ, Patch A-M, Wu J et al. (2012): Pancreatic cancer genomes reveal aberrations in axon guidance pathway genes. Nature 491, 399–405

Blockus H, Chédotal A (2016): Slit-Robo signaling. Development 143, 3037–3044

Burris HA, Moore MJ, Andersen J, Green MR, Rothenberg ML, Modiano MR, Cripps MC, Portenoy RK, Storniolo AM, Tarassoff P et al. (1997): Improvements in survival and clinical benefit with gemcitabine as first-line therapy for patients with advanced pancreas cancer: a randomized trial. J Clin Oncol 15, 2403–2413

Chen B, Gilbert LA, Cimini BA, Schnitzbauer J, Zhang W, Li G-W, Park J, Blackburn EH, Weissman JS, Qi LS et al. (2013): Dynamic imaging of genomic loci in living human cells by an optimized CRISPR/Cas system. Cell 155, 1479–1491

Collisson EA, Bailey P, Chang DK, Biankin AV (2019): Molecular subtypes of pancreatic cancer. Nat Rev Gastroenterol Hepatol 16, 207–220

Collisson EA, Sadanandam A, Olson P, Gibb WJ, Truitt M, Gu S, Cooc J, Weinkle J, Kim GE, Jakkula L et al. (2011): Subtypes of pancreatic ductal adenocarcinoma and their differing responses to therapy. Nat Med 17, 500–503

Conroy T, Desseigne F, Ychou M, Bouché O, Guimbaud R, Bécouarn Y, Adenis A, Raoul J-L, Gourgou-Bourgade S, La Fouchardière C de et al. (2011): FOLFIRINOX versus gemcitabine for metastatic pancreatic cancer. N Engl J Med 364, 1817–1825

Cox JL, Wilder PJ, Desler M, Rizzino A (2012): Elevating SOX2 levels deleteriously affects the growth of medulloblastoma and glioblastoma cells. PLoS ONE 7, e44087

Cruz VH, Arner EN, Du W, Bremauntz AE, Brekken RA (2019): Axl-mediated activation of TBK1 drives epithelial plasticity in pancreatic cancer. JCI Insight 5

da Silva-Diz V, Lorenzo-Sanz L, Bernat-Peguera A, Lopez-Cerda M, Muñoz P (2018): Cancer cell plasticity: Impact on tumor progression and therapy response. Semin Cancer Biol 53, 48–58

Demir IE, Jäger C, Schlitter AM, Konukiewitz B, Stecher L, Schorn S, Tieftrunk E, Scheufele F, Calavrezos L, Schirren R et al. (2018): R0 Versus R1 Resection Matters after Pancreaticoduodenectomy, and Less after Distal or Total Pancreatectomy for Pancreatic Cancer. Ann Surg 268, 1058–1068

Di Costanzo F, Carlini P, Doni L, Massidda B, Mattioli R, Iop A, Barletta E, Moscetti L, Recchia F, Tralongo P et al. (2005): Gemcitabine with or without continuous infusion 5-FU in advanced pancreatic cancer: a randomised phase II trial of the Italian oncology group for clinical research (GOIRC). Br J Cancer 93, 185–189

Diaferia GR, Balestrieri C, Prosperini E, Nicoli P, Spaggiari P, Zerbi A, Natoli G (2016): Dissection of transcriptional and cis-regulatory control of differentiation in human pancreatic cancer. EMBO J 35, 595–617

Dobin A, Davis CA, Schlesinger F, Drenkow J, Zaleski C, Jha S, Batut P, Chaisson M, Gingeras TR (2013): STAR: ultrafast universal RNA-seq aligner. Bioinformatics 29, 15–21

Domyan ET, Branchfield K, Gibson DA, Naiche LA, Lewandoski M, Tessier-Lavigne M, Le Ma, Sun X (2013): Roundabout receptors are critical for foregut separation from the body wall. Dev Cell 24, 52–63

Du W, Huang H, Toombs J, Wang Z, Hosein A, Burton N, Brekken RA (2019): Abstract 1037: Axl is critical for pancreatic cancer progression and metastasis. Cancer Res 79, 1037

Escot S, Willnow D, Naumann H, Di Francescantonio S, Spagnoli FM (2018): Robo signalling controls pancreatic progenitor identity by regulating Tead transcription factors. Nat Commun 9, 5082

Foucher ED, Ghigo C, Chouaib S, Galon J, Iovanna J, Olive D (2018): Pancreatic Ductal Adenocarcinoma: A Strong Imbalance of Good and Bad Immunological Cops in the Tumor Microenvironment. Front Immunol 9, 1044

Fujiwara M, Ghazizadeh M, Kawanami O (2006): Potential role of the Slit/Robo signal pathway in angiogenesis. Vasc Med 11, 115–121

Gabitova-Cornell L, Surumbayeva A, Peri S, Franco-Barraza J, Restifo D, Weitz N, Ogier C, Goldman AR, Hartman TR, Francescone R et al. (2020): Cholesterol Pathway Inhibition Induces TGF-β Signaling to Promote Basal Differentiation in Pancreatic Cancer. Cancer Cell 38, 567-583.e11

Gjerdrum C, Tiron C, Høiby T, Stefansson I, Haugen H, Sandal T, Collett K, Li S, McCormack E, Gjertsen BT et al. (2010): Axl is an essential epithelial-to-mesenchymal transition-induced regulator of breast cancer metastasis and patient survival. Proc Natl Acad Sci U S A 107, 1124–1129

Gnoni A, Licchetta A, Scarpa A, Azzariti A, Brunetti AE, Simone G, Nardulli P, Santini D, Aieta M, Delcuratolo S et al. (2013): Carcinogenesis of Pancreatic Adenocarcinoma: Precursor Lesions. Int J Mol Sci 14, 19731–19762

Goetze R-G, Buchholz SM, Patil S, Petzold G, Ellenrieder V, Hessmann E, Neesse A (2018): Utilizing High Resolution Ultrasound to Monitor Tumor Onset and Growth in Genetically Engineered Pancreatic Cancer Models. J Vis Exp

Golan T, Hammel P, Reni M, van Cutsem E, Macarulla T, Hall MJ, Park J-O, Hochhauser D, Arnold D, Oh D-Y et al. (2019): Maintenance Olaparib for Germline BRCA-Mutated Metastatic Pancreatic Cancer. N Engl J Med 381, 317–327

Gong J, Muñoz AR, Pingali S, Payton-Stewart F, Chan DE, Freeman JW, Ghosh R, Kumar AP (2017): Downregulation of STAT3/NF-κB potentiates gemcitabine activity in pancreatic cancer cells. Molecular Carcinogenesis 56, 402–411

Goyette M-A, Cusseddu R, Elkholi I, Abu-Thuraia A, El-Hachem N, Haibe-Kains B, Gratton J-P, Côté J-F (2019): AXL knockdown gene signature reveals a drug repurposing opportunity for a class of antipsychotics to reduce growth and metastasis of triple-negative breast cancer. Oncotarget 10, 2055–2067

Greenberg JM, Thompson FY, Brooks SK, Shannon JM, Akeson AL (2004): Slit and robo expression in the developing mouse lung. Dev Dyn 230, 350–360

Grivennikov SI, Greten FR, Karin M (2010): Immunity, inflammation, and cancer. Cell 140, 883–899

Han S, Cao C, Tang T, Lu C, Xu J, Wang S, Xue L, Zhang X, Li M (2015): ROBO3 promotes growth and metastasis of pancreatic carcinoma. Cancer Lett 366, 61–70

Hay ED (1995): An overview of epithelio-mesenchymal transformation. Acta Anat (Basel) 154, 8–20

Herreros-Villanueva M, Zhang J-S, Koenig A, Abel EV, Smyrk TC, Bamlet WR, Narvajas AA-M de, Gomez TS, Simeone DM, Bujanda L et al. (2013): SOX2 promotes dedifferentiation and imparts stem cell-like features to pancreatic cancer cells. Oncogenesis 2, e61

Hessmann E, Patzak MS, Klein L, Chen N, Kari V, Ramu I, Bapiro TE, Frese KK, Gopinathan A, Richards FM et al. (2018): Fibroblast drug scavenging increases intratumoural gemcitabine accumulation in murine pancreas cancer. Gut 67, 497–507

Hidalgo M, Álvarez R, Gallego J, Guillén-Ponce C, Laquente B, Macarulla T, Muñoz A, Salgado M, Vera R, Adeva J et al. (2017): Consensus guidelines for diagnosis, treatment and follow-up of patients with pancreatic cancer in Spain. Clin Transl Oncol 19, 667–681

Hinck L (2004): The versatile roles of "axon guidance" cues in tissue morphogenesis. Dev Cell 7, 783–793

Hingorani SR, Wang L, Multani AS, Combs C, Deramaudt TB, Hruban RH, Rustgi AK, Chang S, Tuveson DA (2005): Trp53R172H and KrasG12D cooperate to promote chromosomal instability and widely metastatic pancreatic ductal adenocarcinoma in mice. Cancer Cell 7, 469–483

Hoff DD von, Ervin T, Arena FP, Chiorean EG, Infante J, Moore M, Seay T, Tjulandin SA, Ma WW, Saleh MN et al. (2013): Increased survival in pancreatic cancer with nab-paclitaxel plus gemcitabine. N Engl J Med 369, 1691–1703

Hruban RH, Maitra A, Goggins M (2008): Update on Pancreatic Intraepithelial Neoplasia. Int J Clin Exp Pathol 1, 306–316

Hruban RH, van Mansfeld A d., Offerhaus GJ, van Weering DH, Allison DC, Goodman SN, Kensler TW, Bose KK, Cameron JL, Bos JL (1993): K-ras oncogene activation in adenocarcinoma of the human pancreas. A study of 82 carcinomas using a combination of mutant-enriched polymerase chain reaction analysis and allele-specific oligonucleotide hybridization. Am J Pathol 143, 545–554

Hsu PD, Lander ES, Zhang F (2014): Development and applications of CRISPR-Cas9 for genome engineering. Cell 157, 1262–1278

Huang T, Kang W, Cheng ASL, Yu J, To KF (2015): The emerging role of Slit-Robo pathway in gastric and other gastro intestinal cancers. BMC Cancer 15, 950

Huang C, Huang R, Chang W, Jiang T, Huang K, Cao J, Sun X, Qiu Z (2012): The expression and clinical significance of pSTAT3, VEGF and VEGF-C in pancreatic adenocarcinoma. Neoplasma 59, 52–61

Jaworski A, Tom I, Tong RK, Gildea HK, Koch AW, Gonzalez LC, Tessier-Lavigne M (2015): Operational redundancy in axon guidance through the multifunctional receptor Robo3 and its ligand NELL2. Science 350, 961–965

Jinek M, Chylinski K, Fonfara I, Hauer M, Doudna JA, Charpentier E (2012): A programmable dual-RNA-guided DNA endonuclease in adaptive bacterial immunity. Science 337, 816–821

Jürgens G, Wieschaus E, Nüsslein-Volhard C, Kluding H (1984): Mutations affecting the pattern of the larval cuticle inDrosophila melanogaster II. Zygotic loci on the third chromosome. Wilehm Roux Arch Dev Biol 193, 283–295

Koch-Institut R, GEKID (Gesellschaft Der Epidemiologischen Krebsregister In Deutschland E.V.) (2019): Krebs in Deutschland 2015/2016

Koohini Z, Koohini Z, Teimourian S (2019): Slit/Robo Signaling Pathway in Cancer; a New Stand Point for Cancer Treatment. Pathol Oncol Res

Koorstra J-BM, Hustinx SR, Offerhaus GJA, Maitra A (2008): Pancreatic Carcinogenesis. Pancreatology 8, 110–125

Lamouille S, Xu J, Derynck R (2014): Molecular mechanisms of epithelial-mesenchymal transition. Nat Rev Mol Cell Biol 15, 178–196

Le Large TYS, Bijlsma MF, Kazemier G, van Laarhoven HWM, Giovannetti E, Jimenez CR (2017): Key biological processes driving metastatic spread of pancreatic cancer as identified by multi-omics studies. Semin Cancer Biol 44, 153–169

Leconet W, Larbouret C, Chardès T, Thomas G, Neiveyans M, Busson M, Jarlier M, Radosevic-Robin N, Pugnière M, Bernex F et al. (2014): Preclinical validation of AXL receptor as a target for antibody-based pancreatic cancer immunotherapy. Oncogene 33, 5405–5414

Lee JW, Beatty GL (2020): Inflammatory networks cultivate cancer cell metastasis to the liver. Cell Cycle 19, 642–651

Leis O, Eguiara A, Lopez-Arribillaga E, Alberdi MJ, Hernandez-Garcia S, Elorriaga K, Pandiella A, Rezola R, Martin AG (2012): Sox2 expression in breast tumours and activation in breast cancer stem cells. Oncogene 31, 1354–1365

Li M, Bi X, Huang Z, Zhao J, Han Y, Li Z-Y, Zhang Y, Li Y, Chen X, Hu X et al. (2015): Prognostic Role of Phospho-STAT3 in Patients with Cancers of the Digestive System: A Systematic Review and Meta-Analysis. PLoS ONE 10, e0127356

Liao Y, Smyth GK, Shi W (2014): featureCounts: An efficient general-purpose program for assigning sequence reads to genomic features. Bioinformatics 30, 923–930

Love MI, Huber W, Anders S (2014): Moderated estimation of fold change and dispersion for RNA-seq data with DESeq2. Genome Biol 15, 550

Ludwig KF, Du W, Sorrelle NB, Wnuk-Lipinska K, Topalovski M, Toombs JE, Cruz VH, Yabuuchi S, Rajeshkumar NV, Maitra A et al. (2018): Small-Molecule Inhibition of Axl Targets Tumor Immune Suppression and Enhances Chemotherapy in Pancreatic Cancer. Cancer Res 78, 246–255

Macias H, Moran A, Samara Y, Moreno M, Compton JE, Harburg G, Strickland P, Hinck L (2011): SLIT/ROBO1 signaling suppresses mammary branching morphogenesis by limiting basal cell number. Dev Cell 20, 827–840

Massagué J, Blain SW, Lo RS (2000): TGFβ Signaling in Growth Control, Cancer, and Heritable Disorders. Cell 103, 295–309

Maurer C, Holmstrom SR, He J, Laise P, Su T, Ahmed A, Hibshoosh H, Chabot JA, Oberstein PE, Sepulveda AR et al. (2019): Experimental microdissection enables functional harmonisation of pancreatic cancer subtypes. Gut 68, 1034–1043

Mehlen P, Delloye-Bourgeois C, Chédotal A (2011): Novel roles for Slits and netrins: axon guidance cues as anticancer targets? Nat Rev Cancer 11, 188–197

Miyabayashi K, Baker LA, Deschênes A, Traub B, Caligiuri G, Plenker D, Alagesan B, Belleau P, Li S, Kendall J et al. (2020): Intraductal Transplantation Models of Human Pancreatic Ductal Adenocarcinoma Reveal Progressive Transition of Molecular Subtypes. Cancer Discov 10, 1566–1589

Moffitt RA, Marayati R, Flate EL, Volmar KE, Loeza SGH, Hoadley KA, Rashid NU, Williams LA, Eaton SC, Chung AH et al. (2015): Virtual microdissection identifies distinct tumor- and stroma-specific subtypes of pancreatic ductal adenocarcinoma. Nat Genet 47, 1168–1178

Moradpour M, Abdulah SNA (2020): CRISPR/dCas9 platforms in plants: strategies and applications beyond genome editing. Plant biotechnology journal 18, 32–44

Morlot C, Thielens NM, Ravelli RBG, Hemrika W, Romijn RA, Gros P, Cusack S, McCarthy AA (2007): Structural insights into the Slit-Robo complex. Proc Natl Acad Sci U S A 104, 14923–14928

Morris JP, Wang SC, Hebrok M (2010): KRAS, Hedgehog, Wnt and the twisted developmental biology of pancreatic ductal adenocarcinoma. Nat Rev Cancer 10, 683–695

Muller PAJ, Vousden KH (2013): p53 mutations in cancer. Nat Cell Biol 15, 2–8

Nagathihalli NS, Castellanos JA, VanSaun MN, Dai X, Ambrose M, Guo Q, Xiong Y, Merchant NB (2016): Pancreatic stellate cell secreted IL-6 stimulates STAT3 dependent invasiveness of pancreatic intraepithelial neoplasia and cancer cells. Oncotarget 7, 65982–65992

Neesse A, Algül H, Tuveson DA, Gress TM (2015): Stromal biology and therapy in pancreatic cancer: a changing paradigm. Gut 64, 1476–1484

Neesse A, Bauer CA, Öhlund D, Lauth M, Buchholz M, Michl P, Tuveson DA, Gress TM (2019): Stromal biology and therapy in pancreatic cancer: ready for clinical translation? Gut 68, 159–171

Nieto MA, Huang RY-J, Jackson RA, Thiery JP (2016): EMT: 2016. Cell 166, 21–45

Oettle H, Neuhaus P, Hochhaus A, Hartmann JT, Gellert K, Ridwelski K, Niedergethmann M, Zülke C, Fahlke J, Arning MB et al. (2013): Adjuvant chemotherapy with gemcitabine and long-term outcomes among patients with resected pancreatic cancer: the CONKO-001 randomized trial. JAMA 310, 1473–1481

Öhlund D, Handly-Santana A, Biffi G, Elyada E, Almeida AS, Ponz-Sarvise M, Corbo V, Oni TE, Hearn SA, Lee EJ et al. (2017): Distinct populations of inflammatory fibroblasts and myofibroblasts in pancreatic cancer. J Exp Med 214, 579–596

Pak JS, DeLoughery ZJ, Wang J, Acharya N, Park Y, Jaworski A, Özkan E (2020): NELL2-Robo3 complex structure reveals mechanisms of receptor activation for axon guidance. Nat Commun 11, 1489

Patil S, Steuber B, Kopp W, Kari V, Urbach L, Wang X, Küffer S, Bohnenberger H, Spyropoulou D, Zhang Z et al. (2020): EZH2 Regulates Pancreatic Cancer Subtype Identity and Tumor Progression via Transcriptional Repression of GATA6. Cancer Res 80, 4620–4632

Pinho AV, van Bulck M, Chantrill L, Arshi M, Sklyarova T, Herrmann D, Vennin C, Gallego-Ortega D, Mawson A, Giry-Laterriere M et al. (2018): ROBO2 is a stroma suppressor gene in the pancreas and acts via TGF-β signalling. Nat Commun 9, 5083

Procacci P, Moscheni C, Sartori P, Sommariva M, Gagliano N (2018): Tumor¯Stroma Cross-Talk in Human Pancreatic Ductal Adenocarcinoma: A Focus on the Effect of the Extracellular Matrix on Tumor Cell Phenotype and Invasive Potential. Cells 7

Puleo F, Nicolle R, Blum Y, Cros J, Marisa L, Demetter P, Quertinmont E, Svrcek M, Elarouci N, Iovanna J et al. (2018): Stratification of Pancreatic Ductal Adenocarcinomas Based on Tumor and Microenvironment Features. Gastroenterology 155, 1999-2013.e3

Qi LS, Larson MH, Gilbert LA, Doudna JA, Weissman JS, Arkin AP, Lim WA (2013): Repurposing CRISPR as an RNA-guided platform for sequence-specific control of gene expression. Cell 152, 1173–1183

Rahib L, Smith BD, Aizenberg R, Rosenzweig AB, Fleshman JM, Matrisian LM (2014): Projecting cancer incidence and deaths to 2030: the unexpected burden of thyroid, liver, and pancreas cancers in the United States. Cancer Res 74, 2913–2921

Rankin EB, Giaccia AJ (2016): The Receptor Tyrosine Kinase AXL in Cancer Progression. Cancers (Basel) 8

Redston MS, Caldas C, Seymour AB, Hruban RH, da Costa L, Yeo CJ, Kern SE (1994): p53 mutations in pancreatic carcinoma and evidence of common involvement of homocopolymer tracts in DNA microdeletions. Cancer Res 54, 3025–3033

Rhim AD, Mirek ET, Aiello NM, Maitra A, Bailey JM, McAllister F, Reichert M, Beatty GL, Rustgi AK, Vonderheide RH et al. (2012): EMT and dissemination precede pancreatic tumor formation. Cell 148, 349–361

Rothenberg ML, Moore MJ, Cripps MC, Andersen JS, Portenoy RK, Burris HA, Green MR, Tarassoff PG, Brown TD, Casper ES et al. (1996): A phase II trial of gemcitabine in patients with 5-FU-refractory pancreas cancer. Ann Oncol 7, 347–353

Ryan DP, Hong TS, Bardeesy N (2014): Pancreatic adenocarcinoma. N Engl J Med 371, 1039–1049

Sabatier C, Plump AS, Le Ma, Brose K, Tamada A, Murakami F, Lee EY-H, Tessier-Lavigne M (2004): The Divergent Robo Family Protein Rig-1/Robo3 Is a Negative Regulator of Slit Responsiveness Required for Midline Crossing by Commissural Axons. Cell 117, 157–169

Sarkar A, Hochedlinger K (2013): The sox family of transcription factors: versatile regulators of stem and progenitor cell fate. Cell Stem Cell 12, 15–30

Scholz A, Heinze S, Detjen KM, Peters M, Welzel M, Hauff P, Schirner M, Wiedenmann B, Rosewicz S (2003): Activated signal transducer and activator of transcription 3 (STAT3) supports the malignant phenotype of human pancreatic cancer. Gastroenterology 125, 891–905

Seino T, Kawasaki S, Shimokawa M, Tamagawa H, Toshimitsu K, Fujii M, Ohta Y, Matano M, Nanki K, Kawasaki K et al. (2018): Human Pancreatic Tumor Organoids Reveal Loss of Stem Cell Niche Factor Dependence during Disease Progression. Cell Stem Cell 22, 454-467.e6

Sellers WR, Rodgers JW, Kaelin WG (1995): A potent transrepression domain in the retinoblastoma protein induces a cell cycle arrest when bound to E2F sites. Proc Natl Acad Sci U S A 92, 11544–11548

Siegel RL, Miller KD, Jemal A (2019): Cancer statistics, 2019. CA Cancer J Clin 69, 7–34

Singh SK, Chen N-M, Hessmann E, Siveke J, Lahmann M, Singh G, Voelker N, Vogt S, Esposito I, Schmidt A et al. (2015): Antithetical NFATc1-Sox2 and p53-miR200 signaling networks govern pancreatic cancer cell plasticity. EMBO J 34, 517–530

Stella MC, Trusolino L, Comoglio PM (2009): The Slit/Robo system suppresses hepatocyte growth factor-dependent invasion and morphogenesis. Mol Biol Cell 20, 642–657

Sullivan NJ, Sasser AK, Axel AE, Vesuna F, Raman V, Ramirez N, Oberyszyn TM, Hall BM (2009): Interleukin-6 induces an epithelial-mesenchymal transition phenotype in human breast cancer cells. Oncogene 28, 2940–2947

Taverna JA, Hung C-N, DeArmond DT, Chen M, Lin C-L, Osmulski PA, Gaczynska ME, Wang C-M, Lucio ND, Chou C-W et al. (2020): Single-Cell Proteomic Profiling Identifies Combined AXL and JAK1 Inhibition as a Novel Therapeutic Strategy for Lung Cancer. Cancer Res 80, 1551–1563

The Cancer Genome Atlas Research Network, Benjamin J. Raphael, Ralph H. Hruban, Andrew J. Aguirre, Richard A. Moffitt, Jen Jen Yeh, Chip Stewart, A. Gordon Robertson, Andrew D. Cherniack, Manaswi Gupta et al. (2017): Integrated Genomic Characterization of Pancreatic Ductal Adenocarcinoma. Cancer Cell 32, 185-203.e13

Toyonaga T, Nakano K, Nagano M, Zhao G, Yamaguchi K, Kuroki S, Eguchi T, Chijiiwa K, Tsuneyoshi M, Tanaka M (2003): Blockade of constitutively activated Janus kinase/signal transducer and activator of transcription-3 pathway inhibits growth of human pancreatic cancer. Cancer Lett 201, 107–116

Vincent A, Herman J, Schulick R, Hruban RH, Goggins M (2011): Pancreatic cancer. The Lancet 378, 607–620

Waddell N, Pajic M, Patch A-M, Chang DK, Kassahn KS, Bailey P, Johns AL, Miller D, Nones K, Quek K et al. (2015): Whole genomes redefine the mutational landscape of pancreatic cancer. Nature 518, 495–501

Wang Y, van Boxel-Dezaire AHH, Cheon H, Yang J, Stark GR (2013): STAT3 activation in response to IL-6 is prolonged by the binding of IL-6 receptor to EGF receptor. Proc Natl Acad Sci U S A 110, 16975–16980

Wu F, Li J, Jang C, Wang J, Xiong J (2014): The role of Axl in drug resistance and epithelial-to-mesenchymal transition of non-small cell lung carcinoma. Int J Clin Exp Pathol 7, 6653–6661

Xiong A, Yang Z, Shen Y, Zhou J, Shen Q (2014): Transcription Factor STAT3 as a Novel Molecular Target for Cancer Prevention. Cancers (Basel) 6, 926–957

Yadav A, Kumar B, Datta J, Teknos TN, Kumar P (2011): IL-6 promotes head and neck tumor metastasis by inducing epithelial-mesenchymal transition via the JAK-STAT3-SNAIL signaling pathway. Mol Cancer Res 9, 1658–1667

Yadav SS, Narayan G (2014): Role of ROBO4 signalling in developmental and pathological angiogenesis. Biomed Res Int 2014, 683025

Yuan S, Norgard RJ, Stanger BZ (2019): Cellular Plasticity in Cancer. Cancer Discov

Zelina P, Blockus H, Zagar Y, Péres A, Friocourt F, Wu Z, Rama N, Fouquet C, Hohenester E, Tessier-Lavigne M et al. (2014): Signaling switch of the axon guidance receptor Robo3 during vertebrate evolution. Neuron 84, 1258–1272

Zheng X, Carstens JL, Kim J, Scheible M, Kaye J, Sugimoto H, Wu C-C, LeBleu VS, Kalluri R (2015): Epithelial-to-mesenchymal transition is dispensable for metastasis but induces chemoresistance in pancreatic cancer. Nature 527, 525–530

Boston Biomedical (2019): Boston Biomedical, Inc. Announces Update on Phase 3 CanStem111P Study of Napabucasin in Patients with Metastatic Pancreatic Cancer Following Interim Analysis. https://www.bostonbiomedical.com/news-and-media/20190701_boston-biomedical-inc-announces-update-canstem111p-study-following-interim-analysis/, abgerufen am: 16.03.2020

Acknowledgement

Primarily I would like to thank my doctoral supervisor Prof. Dr. Volker Ellenrieder and my supervisor and mentor Dr. Shiv K. Singh for the suggestion and the inspiration for this work as well as the energetic, scientific support and the motivating words during the last years. I am grateful for the opportunity to get to know experimental research, which is very important to me, and to constantly develop myself further.

Special thanks also go to the entire AG Singh working group, which is characterized by a good working atmosphere and always helpful and scientific support. I would particularly like to emphasize the great support of Lukas Klein, Mengyu Tu, Sinan Önder and Frederike Penz, who have always been there to help and advice. I would also like to thank the other working groups in our department AG Ellenrieder, AG Heßmann and AG Neese for excellent cooperation and support.

Furthermore, I would like to thank all our collaborators who have enriched this work and who have contributed to our success. I appreciate especially the help in the implementation of the RNA-Seq provided by Lukas Klein for the preparation of the RNA-Seq and the bioinformatic analysis by Florian Wegwitz. Furthermore, I would like to thank Mengyu Tu for her help with the animal experiments, the KFO 5002 (Department of Gastroenterology and Gastrointestinal Oncology, University Hospital Göttingen, Germany) for the use of the patient derived xenografts (PDX) and Geske Schmidt for her support in the scripting of the work.

Another great achievement that has contributed to this work was the help in creating a stable CRISPR dCas9 mediated ROBO3 knockdown cell line by Xingbo Xu.

Curriculum vitae

My name is Niklas Krebs and I was born on July 14th, 1994 in Bielefeld, as the first of two children of my parents Gabriele Protoschill-Krebs and Dietmar Krebs. My sister is Hannah Krebs.

I started my school career at the Plaßschule in Bielefeld from 2001 to 2005 and finished it in 2013 with the general university entrance qualification at the Gymnasium am Waldhof in Bielefeld.

Afterwards I enrolled in winter semester 2013/2014 for the study of human medicine at the Georg-August-University Göttingen. In 2015 I completed the first and in 2019 the second part of the medical licensing examinations. I was able to expand my medical experience through internships in various departments including Gastroenterology and gastrointestinal Oncology, University Medicine Göttingen. In April 2017 I began working on my dissertation and spent altogether two free semesters in the lab. During this time, several successes have already been achieved, such as the DGVS (Deutsche Gesellschaft für Gastroenterologie, Verdauungs- und Stoffwechselkrankheiten) doctoral scholarship and 3 poster awards at the DPC conferences 2018 and 2020 (Deutscher Pankreas Club) and the EACR (European Association for Cancer Research) "Seed and Soil" Congress 2019. In December 2020, I successfully completed my medical studies. In January 2021, I started working as an assistant physician in the Department of Gastroenterology and Gastrointestinal Oncology at the University Medical Center Göttingen.